TOOLS FOR THE ADVANCEMENT OF CELL-BASED SCREENING FOR NEUROLOGICAL DISORDERS

Kent Ross Gordon

A dissertation submitted to the faculty at the University of North Carolina at Chapel Hill in partial fulfillment of the requirements for the degree of Doctor of Philosophy in the Department of Biomedical Engineering in the School of Medicine.

Chapel Hill
2017

Approved by:

Anne Marion Taylor

Robert Dennis

J. Michael Ramsey

Donald Lo

Donald Rose

ABSTRACT

Kent Ross Gordon: Tools for the Advancement of Cell-based Screening for Neurological Disorders
(Under the direction of Anne Marion Taylor)

The pharmaceutical industry has changed in multiple ways. Major consolidation has continued with increasing mergers and acquisitions. Concurrently, there has been a decreasing trend in the number of new drugs being commercialized. Of this reduced output, new drug discovery has increasingly focused on treatment of neurological disorders, and R&D outsourcing has increased in the form of partnerships with academic drug discovery centers. As public institutions, it is critical for these partnerships to have low cost solutions for their drug discovery needs. In this spirit new focus has been directed at developing technology to improve drug screening for neurological diseases. This new technology includes microfluidic devices for increasing throughput as well as the use of human induced pluripotent stem cell (iPSC) derived neurons which present an advantage over animals for modeling human diseases. Although they show great promise, human iPSC-derived neurons are still hindered by many challenges, including long differentiation times and low yields of homogenous neuronal subtypes. These challenges along with the post-mitotic nature of other mature primary neurons limit the pool of available cells for screening. Historically this has been addressed by

using immortalized non-neuronal cell lines in neurological screening; however screening on neurons represents the possibility of better outcomes due to their phenotypic and morphological accuracy. Thus there is an increased demand for technology to expand neuron throughput for screening. This work explores the use of microraft arrays to increase throughput for neuron-based neurological disorder drug screening. Microraft arrays are culture devices consisting of an array of 1,600 releasable, paramagnetic, polystyrene microrafts (500 µm x 500 µm x 100 µm) each serving as an individual culture surface. The device is used to culture both primary rat neurons as well as human neurons derived from embryonic stem cells, and new tools are created to support this device for screening applications. Individual microraft cultures were maintained in multi-well plates and tools were developed to isolate and transport of individual microrafts to facilitate screening studies. Centering and quantification of these microrafts was achieved and together these results show a strong potential for the use of this device in neurological screening. Finally, in order to demonstrate the high-throughput potential of this technology, scalable assays including a bead-based ELISA and an immunofluorescence assay are devised to detect fragile X mental retardation protein which is reduced in patients with fragile X syndrome – a well-known neurodevelopmental disorder.

To my beloved daughter Amani. You are, and always will be my masterpiece.

ACKNOWLEDGEMENTS

I first extend my gratitude to my advisor Anne M. Taylor for her support. Her kindness and generosity has meant so much to me over the years. I thank my wife Neina Gordon for her love, support, patience, and being the amazing woman she is. I'd like to thank all the members of my committee for their support and guidance. They are all remarkable people and I look up to their excellence. I thank Bob Dennis for serving as chair of my committee and always having my back. I thank my family for their love and support, most of all my parents for always being there for me and staying positive. I thank the members of the Taylor lab past and present for their support, well wishes, and friendship: Tharkika Nagendran, Rebecca Bigler, Joyce Kamande, Mark Niedringhaus, and Nicholas Hallfors. I thank Nancy Allbritton and her lab, specifically Matt Disalvo, Yuli Wang, and Pete Attayek for supplying the Cellraft arrays and answering all of my questions. I give special thanks to Vilma Berg for believing in me and always being there. I give special thanks to Kathy Wood for her support, encouragement, and working tirelessly to create impactful programs for minorities at UNC. I give special thanks to Glenn Walters for his help, guidance, and inspiration. Finally, to my friends Andrew Nigro, Powell Draper, and my friend and mentor Rick Johansen – you're all the best!

TABLE OF CONTENTS

LIST OF TABLES

LIST OF FIGURES

LIST OF ABBREVIATIONS

ALS	Amyotrophic Lateral Sclerosis
ASD	Autism spectrum disorder
CNS	Central nervous system
DMD	Duchenne Muscular Dystrophy
ELISA	Enzyme-linked immunosorbent assay
ESC	Embryonic Stem Cell
FMR1	Fragile X mental retardation 1
FMRP	Fragile X mental retardation protein
FRDA	Friedreich's ataxia
FXN	Frataxin
FXS	Fragile X Syndrome
HD	Huntington's disease
hiPSC	Human induced pluripotent stem cell
HTS	High-throughput screening
HTT	Huntingtin protein
IF	Immunofluorescence

M&A	Mergers and acquisitions
mRNA	Messenger RNA
PDMS	Polydimethylsiloxane
RNA	Ribonucleic acid
SMA	Spinal Muscular Atrophy
SMN	Spinal motor neuron
TR-FRET	Time resolved fluorescence resonance energy transfer

Chapter 1 Background

1.1 Introduction

Neurological disorders including neurodevelopmental and neurodegenerative diseases represent a disease segment with one of the largest unmet need. While undergoing many structural changes, the pharmaceutical industry is now focusing more intensely on this disease segment. For these reasons, new technology is needed to reduce costs. The technology to-date however has yet to make a strong impact on drug discovery and here we learn why this is the case. In this review, an assessment is made of the current state of treatment for neurological diseases followed by the current state of pharmaceutical R&D. Finally, new technological solutions including physical devices and cellular innovations are described along with their implementation.

1.2 Current State of Treatment for Neurological Diseases

There are many neurological disorders without cures or effective treatments. This is the case for a variety of reasons. In some cases the specific cause of the disease or disorder is unknown, so there are no reliable biomarkers from which a treatment can be based. Examples of this include Amyotrophic Lateral Sclerosis (ALS) and late onset Alzheimer's disease. In other cases potential treatments have failed in clinical trials either because they were found ineffective or toxic such as the failure of CEP-1347, the apoptosis kinase inhibitor, which failed to show efficacy in

phase II clinical trials for the treatment of Parkinson's disease.[1] Data has shown an increase in attrition rates for new pharmaceutical projects across all phases, but especially Phase II and III clinical trials.[2] One of the reasons for these increased attrition rates is the discrepancies between the animal models used in preclinical trials and human subjects used in later clinical trials. Another reason is that screening and preclinical work has not been carried out because it is not financially practical for most organizations.

Of the many neurological diseases and disorders, the ones that can benefit the most from new cost saving technology are those in which well-defined biomarkers exist, and are simple in nature such as single gene mutations or those in which a known protein is absent or over expressed. For these reasons, some of the most attractive disorders for drug discovery include Huntington's disease (HD), Fragile X Syndrome (FXS), Duchenne Muscular Dystrophy (DMD), Spinal Muscular Atrophy (SMA), and Friedreich's ataxia (FRDA).

None of these diseases and disorders has a cure and a possible reason for this is the lack of preclinical testing on human cells. Currently the largest impediment to testing with human cells is access. Unless testing can be done on skin fibroblasts or muscle myocytes which are relatively easy to access, currently the only source for diseased neurons comes from post mortem patients. However, these cells are not easily accessible, only represent a particular stage of maturity, and are subject to certain ethical issues. Embryonic stem cell (ESC) derived neurons are also hindered by ethical issues. Human induced pluripotent stem cell

(hiPSC) derived neurons present a promising alternative and will be described in a later section.

1.2.1 Huntington's Disease

Huntington's disease is an autosomal dominant neurodegenerative disorder caused by a CAG repeat expansion in the huntingtin gene. This mutation results in an expanded polyglutamine (polyQ) repeat in the huntingtin protein (HTT). Repeats >36-39 trigger the disorder and longer expansions lead to an early onset.[3; 4] The polyQ repeat expansion leads to a buildup of misfolded HTT which is toxic to neurons in the central nervous system (CNS).

HD is an inherited disorder that typically begins between the ages of 30 to 50 and gets progressively worse after onset. This disease is characterized by uncontrollable motor functions, known as chorea, and cognitive deficits in patients. The impairment in cognition includes attention deficit and loss of short- and long-term memory as well as reduced depth perception.[5] Other symptoms include slurred speech, emotional instability, and difficulty feeding and swallowing.

There is no cure for HD and current treatments only treat symptoms. So far the most successful drug used to treat HD is Tetrabenazine (Zenazine) by Lundbeck. Tetrabenazine, a high-affinity inhibitor of mono-amine uptake into vesicles of presynaptic neurons, was approved in 2008 for chorea in HD patients.[6] Looking at the current pipeline (**Table 1.1**), therapeutic approaches for HD include addressing mutant HTT modification and degradation, addressing signaling pathways, and reducing mutant HTT through inhibition of gene transcription or mRNA translation. Some of these therapeutic strategies are encouraging, but still

very early in development. The major drugs that have failed in the pipeline include Dimebon (Latrepirdine), Coenzyme Q10, PDE10A Inhibitor, Pridopidine, VX15, and PBF-999. All of these drugs failed in phase II or III trials suggesting that they were non-toxic but ineffective. It's possible that this lack of efficacy could be due to the failure to test these compounds on human cells prior to entering the clinic. In preclinical studies, Dimebon and Coenzyme Q10 were tested on the YAC128 HD transgenic mouse while the PDE10A inhibitor was tested on the R6/2 HD mouse model. Pridopidine was tested on CHO cells expressing human D2short dopamine receptors.

1.2.2 Fragile X syndrome

Fragile X syndrome (FXS) is well known neurodevelopmental disorder and one of the leading causes of autism. FXS is caused by a CGG repeat expansion in the 5' untranslated region of the fragile X mental retardation 1 (FMR1) gene located on the X chromosome. This mutation leads to loss of the fragile X mental retardation protein (FMRP). FMRP is a ribonucleic acid (RNA) binding protein which serves to transport intracellular RNA and regulate the translation of target messenger RNAs (mRNA).

FXS is the most common form of inherited mental retardation. FXS also makes up the largest percentage of cases of syndromic autism spectrum disorder (ASD) and affects 1 in 5,000 males and 1 in 6,000 females.[7] Individuals having over 200 repeats, typically ~800 repeats, are considered to have the full mutation and lead to complete silencing of the FMR1 gene, while those with 55-200 repeats are said have the premutation. For the fully mutated FXS patients , symptoms include

moderate to severe mental retardation, delays in social development, attention deficit, hyperactivity, anxiety, reduced motor coordination, and an increased incidence of epilepsy.[8]

Currently there is no cure for FXS. Most current therapies target anxiety and other symptoms rather than addressing the root cause of the disease. Treatments in the pipeline (**Table 1.2**) for FXS target neuro-transmitter dependent receptors, cell signaling molecules, translation regulators, and specific targets of FMRP. In terms of these potential treatments, major clinical failures include Arbaclofen, Basimglurant (RO4917523), and Mavoglurant (AFQ056). Arbaclofen is a GABA-B agonist while Basimglurant (RO4917523) and Mavoglurant (AFQ056) are both mGlur5 antagonists. These are all neuro receptor ligands and instead of addressing the root cause of the disease, they only function to ameliorate the FXS phenotype downstream at neural synapses. Most importantly however, all three of these therapies were tested on the fmr1 knockout mouse model in preclinical studies and not on human cells.

1.2.3 Duchenne Muscular Dystrophy

Duchenne muscular dystrophy (DMD) is the most common form of muscular dystrophy and the most common neuromuscular disease. DMD is caused by disruptions in the DMD gene which consists of 79 exons on the X chromosome. These disruptions include deletions (~65%), duplications (~10%), point mutations (~10%), and other rearrangements (15%), and lead to the loss of the protein, dystrophin, for which it encodes. Dystrophin is present in all types of muscle as well as neurons and is among a family of membrane cytoskeletal proteins.[9-11]

DMD affects 1 in 3,500 boys and is first observed at the age of 3 to 5 years. From onset, the disease is characterized by rapid progression of muscle weakness and degeneration. By the age of 12 most boys lose the ability to walk and death occurs by the age of 20 or 30 usually due to respiratory failure. Girls have a 50 percent chance of inheriting and passing the defective gene to their children.[11-13]

There is no cure for DMD. Glucocorticoid drug therapy represents the best therapeutic option. Examples of this family of drugs include the corticosteroids, prednisone, and deflazacort. These drugs unfortunately have many side effects, but are effective in slowing the rate of muscle deterioration, reducing inflammation, and delaying the disease progression overall. Furthermore, it is not yet clear mechanistically how these drugs function to ameliorate the symptoms of DMD.[11]

Current therapeutic research for DMD can be divided into two approaches – therapies that attempt to upregulate dystrophin production and those that attempt to treat specific phenotypes of the disease. Methods used to restore dystrophin include cell therapy, gene therapy, exon skipping, and suppression of stop codons, while those used to treat the disease phenotypic side effects include anti-inflammatory, anti-fibrotic, and antioxidant agents, myostatin pathway inhibition, neuronal nitric oxide synthase (NNOS) pathway enhancement, and Utrophin upregulation.

There are many therapies currently in clinical trials for DMD (**Table 1.3**); however there have also been many failures. These failures include GSK2402968 (Pro-051), Tadalafil, Drisapersen, ACE-031, PTC124 (Ataluren), BMN053 (Pro-053), BMN044 (Pro-044), and halofuginone (HT-100). GSK2402968 (Pro-051) is a 2OMe

oligomer, Tadalafil is a GMP-hydrolyzing phosphodiesterase 5A (PDE5A) inhibitor, Drisapersen is a 2'O-methyl-phosphorothioate oligonucleotide (2'OMePS) which is a type of antisense oligonucleotide targeting exon 51, ACE-031 is a muscle growth factor, PTC124 (Ataluren) is a stop codon suppressor, BMN053 (Pro-053) is a 2'OMePS targeting exon 53, BMN044 (Pro-044) is a 2'OMePS targeting exon 44, and halofuginone (HT-100) is an anti-fibrotic TGF-β inhibitor. The majority of these therapies were tested on human myoblasts except for Tadalafil and halofuginon (HT-100) which were tested on the mdx mouse model.[14-16]

1.2.4 Spinal Muscular Atrophy

Spinal muscular atrophy (SMA) is a neuromuscular disorder caused by mutation or deletion of the survival motor neuron (SMN) 1 gene which leads to a reduction or loss of the SMN protein. The function of the SMN protein includes RNA transcription, pre-mRNA splicing, small nuclear ribonucleoprotein (snRNP) biogenesis, axonal transport, and cytoskeletal dynamics.[17] Humans also possess an SMN2 gene which is paralogous to SMN1 with the exception of a translational silence occurring at nucleotide 840 which leads to alternative splicing. The majority of the SMN protein is therefore produced by SMN1 however SMN2 does produce low levels of the protein. Loss of the SMN protein leads to degradation of motor neurons in the spinal cord.

Spinal muscular atrophy affects approximately 1 in 10,000 newborns and is considered the second most common fatal autosomal recessive disorder.[18] There are three types of SMA and all result in weakness and degradation of muscles

located in the trunk and distal limbs, thus causing difficulties in breathing and movement.

There is no cure for SMA. Current therapeutic research on SMA has focused on four major therapeutic approaches. These approaches include replacement or correction of the mutated SMN1 gene, modulation of the SMN2 gene, neuroprotection of distressed motor neurons, and prevention and restoration of muscle function loss.

Currently 4-AP (Dalfampridine-ER, Ampyra) is showing the most promise in clinical trials. This drug has been approved to treat muscle fatigue in patients with multiple sclerosis and is sold and produced by Acorda Therapeutics.[19] Although the studies on SMA have been completed successfully, Chiriboga et al. from Columbia University found no positive improvement in motor function or ambulation in adults ages 18-50 at the doses approved for muscular sclerosis.[20]

SMA has seen two therapeutic failures in Phase I clinical trials suggesting issues with toxicity (**Table 1.4**). These failures include the small molecules LM1070 by Novartis, and RG7800 (RO7034067, RO6885247) by Roche and PTC Pharmaceuticals. LMI070 (NVS-SM1) is an SMN2-splicing modulator and was tested on the C/+ SMA mouse model in preclinical studies.[21] RG7800 (RO7034067, RO6885247) is also an SMN2-splicing modulator, however preclinical studies of this compound were tested on the Δ7 SMA mouse model as well as Islet-1+ hiPSC-derived motor neurons.[22]

1.2.5 Friedreich's Ataxia

Friedreich ataxia (FRDA) is an autosomal recessive neurodegenerative disease caused by a mutated expansion of the guanine-adenine-adenine (GAA) triplet on both alleles of the frataxin (FXN) gene. This is a heterogeneous disease with a range of 600 to 1200 repeats. This mutation leads to loss and reduced expression of the protein frataxin which is produced in the mitochondria and is involved in iron metabolism within the cell and also has antioxydative properties. A loss of FXN protein leads to dysfunction in ATP synthesis, iron accumulation, possible oxidative stress, and cellular dysfunction as a whole.[23; 24]

FRDA is the most common form of hereditary ataxia. In the United States approximately 1 in 100 people are carriers of the mutated FXN gene and one in 20,000 to 50,000 are affected. Symptoms of the disease include loss of coordination (ataxia), fatigue, loss of vision, loss of hearing, impaired speech, aggressive scoliosis, diabetes mellitus, and serious heart conditions including hypertrophic cardiomyopathy. These symptoms usually begin between the ages of 5 and 25 but occasionally begin in middle aged adults. Most people diagnosed with the disease require walking aids such as a wheelchair by their early 20s.[25; 26]

Therapeutic research for FRDA has focused on mitochondrial function, oxidative stress, upregulation of FXN, gene therapy, and neurotrophic factors.

FRDA has seen many drug failures in recent years. These include the antioxidents Idebenone and alpha-tocopherolquinone, the FXN modulators Interferon-ɣ and Lu-AA24493, the iron chelator deferiprone, pioglitazone, EGB761,

and verenicline. While many of these drugs were tested on human fibroblasts in preclinical studies, none were tested on human motor neurons.

All of the above mentioned diseases and disorders lack a cure. Drugs have continued to fail in the regulatory pipeline, and in most of these cases preclinical studies were performed on non-human cells. Drug screening using human cells may improve the identification of drugs that are effective in humans. Thus there is an obvious need for new technologies to make preclinical studies on human cells more feasible and help pave the way for cures for such diseases.

1.3 Current State of Commercial Drug Discovery R&D

1.3.1 Current State of Pharmaceutical R&D and Future Directions

The pharmaceutical industry has undergone many changes over the last half century. After adjusting for inflation, the cost to bring a new drug to market in the 1980's was approximately $400 MM, and took 7 years, while today it's close to $2.6 B and requires 15 years.[27] These increased costs can be attributed to the rising costs of Phase II and Phase III clinical trials. Furthermore, where clinical costs were less than pre-human studies in the 1980s to early 1990s, clinical studies have risen in cost dramatically over the past twenty years.[27]

The industry is also undergoing increased levels of consolidation. From 1988 to 2011 the membership of the Pharmaceutical Research and Manufacturers of America (PhRMA) organization saw a 75% reduction largely because of mergers and acquisitions (M&A) in the industry. Some examples of major M&A deals during this time include that of Brystol-Myers and Squibb in 1989, Glaxo and Smith-Kline in

2000, and Pfizer (Warner-Lambert, Pharmacia) and Wyeth in 2009. Taking advantaged of synergies, this increased consolidation has led to cuts in R&D and some argue the decline in output efficiency.[28]

Reduced efficiency has been a major topic in the Pharmaceutical industry in the past twenty years. The number of new drugs approved per billion US dollars spent on R&D has been in a broad decline since 1950 (**Figure 1.1**), and taken as just the new drugs approved, this number has been mainly flat (**Figure 1.2**).

As mentioned above, one possible reason for stagnation is due to industry consolidation. Between 1990 and 1999 there was an average of 31 drugs approved per year compared to 24 drugs from the years 2000 to 2009. This number peaked in 1996 with 54 drugs, but many of the companies that existed back then do not exist today.[28]

Another possible reason for the decline in efficiency is associated with the idea of “low hanging fruit”. This theory follows the notion that the technically tractable drugs such as the cardiovascular statins of the ‘90s have already been developed and the diseases that remain to be treated are much more difficult to develop drugs for. This concept somewhat discounts the efforts that went into developing early drugs and fails to account for the fact that successfully commercialized drugs raise the standards and lower the value of undiscovered drugs. It does however point to the treatment of neurological diseases as the future of drug discovery next to cancer therapies.[2; 29-31] From 2000-2007, nervous system focused R&D increased 1.09% compared to -4.57% for the cardiovascular system.[2]

However, due to a lack of pathological understanding as well as disease heterogeneity, treatment of neurological diseases faces a much steeper path.

1.3.2 Public Private Partnerships in Drug Development

With continued consolidation and the growing costs of R&D, companies are increasingly outsourcing R&D efforts to help preserve profits and minimize their risk in the market. These public-private partnerships (PPP) can exist between pharmaceutical companies and academic institutions, or foundations with public health initiatives. These models are set up to defer the costs of early stage drug development to the public through i.e. NIH, while improving the academic drug discovery capabilities and the value gained from NIH funded research.

The pharmaceutical industry and academia have shared a rich history. In the past, companies have been formed by commercializing new drugs developed by academic researchers. One of the most well-known examples of this was Genentech, founded by Herbert Boyer of UCSF and venture capitalist Robert Swanson in 1976.[32] More recently there is Vertex, Infinity, and H3 Biosciences all produced by Professor Stuart Schreiber and colleagues at Harvard University. Finally, there is a list of well-known drugs that have come out of academic institutions including pregabalin (Lyrica™; Silverman lab, Northwestern), emtricitabine (Emtriva™; Liotta lab, Emory) and premetrexed (Alimta™; Taylor lab, Princeton).[33-35]

These early cases have paved the way for official partnerships between Pharma and Academia and these collaborations continue to grow to this day. As of 2017 the Academic Drug Discovery Consortium reported 148 active university-led

drug discovery centers across the country. This consortium also tracks partnerships between these centers and the pharmaceutical industry and some notable ones include Yale University (GSK, Gilead Sciences, Evotec AG), UCSF (Sanofi, Genentech, Bayer, Pfizer), Vanderbilt (Bristol-Myers Squibb, Astra Zeneca, GSK), University of Pennsylvania (Novartis, Astra Zeneca), Broad Institute of Harvard and MIT (Astra Zeneca), UC San Diego (Roche), Oxford University (Novo Nordisk, UCB), California Institute for Biomedical Research (Merck), Harvard University (UCB), and Johns Hopkins Brain Science Institute (Janssen Pharmaceuticals). Relying on public funding, it is critical for these academic institutions to have access to technology to reduce the costs of drug discovery as much as possible.

1.4 Current State of Technology for Screening for Neurological Conditions

New technology is being developed continuously to advance small molecule screening, improving efficiency, efficacy, and reducing costs. High-density microtiter plates such as 96- and 384-well plates remain the gold standard for cell-based phenotypic screening; however these plates are still relatively low in throughput resulting in the need for large populations of cells and significant volumes of compounds and reagents. Higher throughput plates such as 1536- and 3456-well plates have been designed, with the former starting to become more prominent, however these plates are marked by high evaporation and require expensive equipment for handling. Increased focus has been placed on the use of microfluidics in screening in order to address these issues. Microfluidic approaches for drug discovery can be divided into two major categories, array based systems and droplet based systems.

1.4.1 Array Based Microfluidic Systems

Wlodkowic et al. published in 2009 the design of a polydimethylsiloxane (PDMS) array of micromechanical traps to hydrodynamically capture single nonadherent hematopoietic cells (**Figure 1.3**). After being exposed to anti-cancer drugs, this study showed that ~300 trapped cells could be analyzed with real time fluorescent imaging just as effectively as traditional single cell analysis techniques such as a flow cytometry which requires a much larger cell population. This major drawback to this device is that it is a continuous system and cannot test multiple compounds in parallel.[36]

Dimov et al. published in 2011 the development of an integrated microfluidic array plate (iMAP) which is a gravity driven (pump and tube free), PDMS based, microfluidic culture device for the capture and analysis of discrete populations of cells (**Figure 1.4**). This device can interrogate 64 separate populations with the capability of performing real-time Nucleic Acid Sequence Based Amplification (NASBA) and immunofluorescent (IF) analysis. Each populations consists of 5-50 cells however culture of these cells was done under constant perfusion. The performance of this device was demonstrated with NASBA, IF, and a drug dose analysis using HeLa and MCF7 cells.[37]

Wang et al. developed a microfluidic cell array with individually addressable chambers. Fabricated out of PDMS, this chip featured 36 chambers arranged in a 6 x 6 array and access to these chambers were controlled with pneumatic valves through an automated system (**Figure 1.5**). Cells were loaded into the array via syringe pump into the six inlets identified in orange in **Figure 1.5**, and access to the

cell chambers was controlled by surrounding, water-filled channels (identified in blue in **Figure 1.5**) which would expand and contract to gas pressure controlled by solenoid valves. To seed specific cell types into specific chambers, the cell suspension in the syringe pump would have to be changed while the valves for the target chamber were open and the surrounding chambers were closed. The utility of the device was demonstrated by seeding two cell types, regular Chinese hamster ovary (CHO) cells and EGFP-expressing CHO cells, into specific chambers, and then treating specific chambers with specific fluorescent dyes. The number of cells in each chamber ranged in the 100s and were cultured for 2 days.[38]

In an effort to seed and culture multiple cell types in specific localized positions in an easier and more efficient way, Gao et al. created a microfluidic device which does so utilizing vacuum actuation (**Figure 1.6**). Fabricated from PDMS, this device featured 256 culture channels divided into eight individually addressable regions and all branched from a central main channel. In their proof of design study, four cell types were seeded including HuT 78, Ramos, PC-3, and C166-GFP cells and viability and cell proliferation were measured. With cultures varying from 2-7 days, viability ranged from 92-97% and each cell population was individually monitored for its response to apoptosis inducing compounds.[39]

Screening multiple compounds in combination is also a concern in drug development in order to assess possible side effects. In order to reduce equipment and reagent costs for *in vitro* drug combination screening, Kim et al. designed a programmable microfluidic cell culture array for the generation of drug concentrations and then combined them pairwise with cell populations for

observation (**Figure 1.7**). Fabricated from two layers of PDMS, one for fluid exchange and one for pneumatic control, this device featured 64 individually addressable cell culture chambers connected to a set of upstream concentration channels where compounds are diluted and combined. Using human prostate cancer PC3 cells, the device was demonstrated by inducing viability loss by introducing combinations of the chemotherapeutic drugs doxorubicin and mitoxantrone with TNF-alpha Related Apoptosis Inducing Ligand (TRAIL). One of the unique attributes of this device is its ability to operate without continuous perfusion, however media changes were performed every three hours possibly leading to a lower effectiveness in the combination treatments when compared to the use of traditional 96-well plates.[40]

In an interesting effort to encompass all the tools and resources necessary for a drug screen, Zhou et al. developed an automated nanoliter dispensing microfluidic liquid handler and accompanying micro-multiwell chip which reduces reagent consumption and expands cellular throughput (**Figure 1.8**). Using standard soft lithography methods, the nanoliter liquid handling pipette chip was fabricated with four channels in parallel which dispense 50 to 500 nL with a coefficient of variation (CV) < 8% at 150 nL. This device dispenses cells and fluids into a 96-well microchip consisting of 12 X 8 individual microwells, with each microwell holding a maximum volume of 500 nL. In demonstrating the device ~350 nL were dispensed in each well resulting in 400-500 cells per well. These cells were grown for over 48 hours with media replacement every 8 hours. Altogether, the study showed that cells could be

seeded, transferred, passaged, transfected, stimulated by drugs, and observed in a screening assay.[41]

To address the growing need to miniaturize screening assays while also making them affordable, easy to handle, and accurate, Du et al. described in 2013 a 2-dimensional PDMS based microfluidic culture device to increase throughput for combination drug testing (**Figure 1.9**). The system was designed around the sequential operation droplet array (SODA) technique, and featured a chip with an array of 342 circular micro-wells each 1.3 mm in diameter and 10 µm in depth. Using this chip and an automated stage and capillary system, 11-day old cell cultures were achieved in oil-covered 500 nL droplets with media changes every 24 hours. Each droplet supported 80-100 cells/well of A549 cells. Using this technology, not only was cell viability comparable to 96 and 384-well plates, but drug consumption for each well was reduced by 2-3 orders of magnitude.[42]

To create a large number of unique microenvironments for the growth and analysis of stem cells, Zhang et al. developed a superhydrophobic microwell array chip (SMARchip) (**Figure 1.10**). Seeding and fluid exchange in the chip was facilitated by a robotic spotter. The SMARchip was fabricated by micrografting a PDMS array to the superhydrophobic layer via contact printing. The final SMARchip consisted of a 960-well array each with a 500 µm diameter and a 100 µm-thick superhydrophobic layer. In order to prevent evaporation, the device was handled in a custom built glovebox and contained double Petri dishes with sterile water during culture. In demonstrating the performance of the device BHK-21, HUVEC, and K562 cells were cultured for 2-5 days while growth rate and viability were measured.

Additionally, the device's screening capabilities were demonstrated by culturing Oct4-EGFP mouse induced pluripotent stem cells (iPSCs) for four days and individually delivery soluble factors while measuring their effects on pluripotency and proliferation.[43]

Similarly, Popova created a droplet microfluidic array (DMA) with super hydrophilic and hydrophobic areas to eliminate the risk of cross-contamination between cell clusters when screening on cell microarrays (**Figure 1.11**). The DMA was fabricated using a standard microscope slide upon which a layer of nanoporous poly(2-hydroxyethyl methacrylate-co-ethylene dimethacrylate) (HEMA-EDMA) film was placed. This surface was then functionalized with one reaction to create superhydrophilic squared spots and another reaction to create superhydrophobic borders. In all, three different arrays were created with 588, 2187, and 4563 spots of sizes 1000 µm, 500 µm, and 350 µm respectively. In evaluating the device, HeLa, HEK293, and A549 cells were seeded and then morphologically observed. Additionally, the utility of the DMA in screening was first tested by reverse transfecting HEK293 cells and then individually treating HeLa cells with doxorubicin and quantifying its effect on the cells by calcein staining.[44]

1.4.2 Droplet Based Microfluidic Systems

In order to study microbial ecology, physiology, evolution, and adaptation to changing environments, Jakiela et al developed a droplet based microfluidic device to isolate populations of bacteria (**Figure 1.12**). Composed of ten input and output channels, the device performs three functions: 1) formation of microdroplets containing cells, reagents, and grow factors; 2) cycles microdroplets for cell

incubation and monitoring; and 3) splits and fuses microdroplets to control the modulate the concentration of injected chemical factors. Using the device 164 microdroplet chemostats were produced and monitored. Chemostats are culture modules for bacteria, yeast, and algae which continuously replenish fluids to maintain volume and concentration of growth reagents for the optimal culture environment. Microfluidics greatly reduces the cost of producing these chemostats, so in demonstrating the application of this device, the growth and response of E. Coli cells (~14,000 cells per droplet) was observed after being introduced to varying concentrations of tetracycline and chloramphenicol and the bacterial showed similar growth to that grown in a bulk environment.[45]

In a demonstration of digital microfluidics (DMF), Bogojevic et al. developed the first DMF device to implement a parallel-scale cell-based assay (**Figure 1.13**). Using photolithography and etching this device was fabricated as two plates separated by a 140 µm space with patterned chromium electrodes on the bottom plate and a 50 nm Teflon-AF coating on either side of the inside surface. The device has six 1.5 mm diameter assay zones in the central region with twelve adjacent reagent reservoirs. After plating HeLa cells at approximately 800 cells per assay zone and incubating overnight, a fluorogenic apoptosis assay for caspase-3 activity was performed since it is popular in anti-cancer drug discovery. The results showed a 33-fold reduction in reagent consumption and lower detection limit and greater dynamic range than the same assay performed in a 96-well plate.[46]

As seen from these examples, there are a wide variety of approaches in developing microfluidic platforms for drug screening. While these devices are able

to interagate small cell populations with extremely low reagent volumes, they do suffer certain consequences, namely the ability to produce long term cultures. Except for the Du and Zhang devices, these platforms have not been proven to support cells for more than 48 hours, and all require frequent media changes. There has yet to be a commercially popular device that combines the volume advantages of 384-well plates with the throughput advantages of microfluidics.

1.5 Use of Human iPSC Derived Neurons in HTS

1.5.1 History and Advantages of Human iPSCs

With the increased focus of the pharmaceutical industry on treating neurological disorders, there is a greater need for accurate disease models. With the discovery and development of human induced pluripotent stem cells (hiPSCs) a massive movement has been underway to realize the potential of this new technology in better understanding the pathology and mechanisms of neurological disorders as well as discovery of new drugs to treat them. Although extensive efforts have been made, therapies have failed to come to fruition. The reasons for this failure include the polymorphic nature and our lack of understanding of the disease pathogenesis, the failure of animal models to fully recapitulate all aspects of the disease including genetic - environmental interactions, and limited access to human cellular samples at different stages of maturation and disease progression.

Animals have been used widely in the study of diseases and their mechanisms; however use of animal models in drug discovery has not led to successful therapies in the clinic.[47] These failures may be in part due to genetic,

anatomical, and/or physiological differences between animal models and humans. In the case of rodents, which we diverged from 60 million years ago, there are significant genomic differences such as noncoding and regulatory RNA that play a major role in disease epigenetics. Anatomically there are major differences as well, such as the difference in development of the prefrontal and temporal cortex of the rodent versus the human brain. Also, rodent brains are lissencephalic and don't contain certain types of neurons that exist in the human brain such as Von Economo neurons.[48] Such differences affects neurogenesis and neuronal function, therefore neurons dissected from mice may not always have the same morphology as human neurons. Finally, in terms of physiology, these genetic and anatomic differences effect neuronal function, and thus rodent neurons behave differently as well. Specifically, it has been shown that rodent neurons have different electrophysiological properties than human neurons.[49] Taken together, these differences may explain part of the discrepancies between preclinical and clinical data.

Given the threat of misinformation posed by animal models, new attention is being given to the use of human cells for drug screens. However access to human brain tissue may be difficult to impossible to obtain. Currently, human brain tissue can be extracted from live surgeries, or postmortem subjects. For a variety of reasons however, these samples are not ideal for high-throughput screening. First, similar to rodent neurons, they are post mitotic and there is a limited supply of tissue/cells that can be derived – not nearly enough needed for screens or repeated experiments. Second, these neurons represent cells at a late stage of development

and therefore are not ideal for modeling neurodevelopment in early onset diseases. Furthermore, neurons derived from postmortem subjects or neurosurgeries eliminate the possibility of performing patient specific screens or establishing biobanks that represent the mosaic nature of many neurological and neuropsychiatric diseases.

Given the limitations of these current models, human iPSCs make it possible to perform screens on human neurons from patients with specific genetic mutations caused by a known neurological disorder. The discovery of these cells thus was a major breakthrough and even overcame the moral challenges of using embryonic stem cells (ESCs) which were already seeing limited use. In 2006, Takahashi and Yamanaka discovered hiPSCs, for which they received the Nobel Prize. In their landmark paper, they demonstrated that mouse fibroblasts could be reprogrammed into a pluripotent state similar to ESCs by introducing transcription factors in a retroviral-mediated process. The four transcription factors used in this study were OCT3/4, SOX2, c-MYC, and KLF4.[50] After induction, pluripotent stem cells can differentiate into any human cell, and within a year of these original studies, human iPSCs had been generated from a number of different tissue sources, fibroblasts and peripheral blood being the most common.[51]

High-throughput screening using stem cell derived neurons was first demonstrated with ESCs. McNeish et al. performed a screen of over 2 million compounds to identify a glutamate receptor potentiator to enhance cognitive ability. The primary screen was carried out using mouse ESC-derived neurons while the secondary screen to validate the leads was performed on human ESC-derived

neurons. This campaign paved the way for eventual screens using hiPSC-derived neurons.[52]

1.5.2 Current Use of hiPSC-derived Neurons

Executing effective screens for neurological and neurodegenerative disorders partially depend on the types of neurons available. Over the years various types of neurons have been derived from hiPSCs with motor, cortical, and dopaminergic neurons being the most developed and characterized. Each of these types of neurons is produced from a different differentiation protocol, and these protocols have evolved over the years.

In 2008 Eggan et al. first demonstrated motor neuron differentiation from human somatic cells. Established from a previous study which produced MNs from mouse stem cells using a retinoic acid (RA) and sonic the hedgehog (SHH) for the neural patterning, Eggan's group was able to mimic this same protocol in hESCs.[53] Shortly thereafter this method was adopted by Ebert to produce motor neurons from hiPSCs. This was the first study to show a disease specific phenotype in differentiated motor neurons, and paved the way for future studies, however it resulted in an efficiency of less than 10% and required a 56-day differentiation time frame.[54] Since then efficiencies and differentiation times have improved, but are still not ideal for large scale screening purposes. (**Table 1.6**)

Similar to motor neurons, cortical neurons were first developed using ESCs. In 2009 Li et al. produced cortical glutamatergic cells from hESCs using RA in the absence of morphogens.[55] Also during that time Eiraku et al. differentiated cortical neurons from hESCs using a three-dimensional quick aggregation culture (SFEBq)

method in 24 days.[56] It was not until 2012 however that cortical neurons were differentiated from hiPSCs by Shi et al. in their landmark study. In this elegant work, dual SMAD inhibition using Noggin and SB431542 was combined with retinoids to produce 95%efficiency; however differentiation time for mature neurons was between 60 to 90 days. Although this is consistent with the time frame of neurogenesis in human development, it is not ideal for screening campaigns. Fortunately other protocols with shorter differentiation times have been produced since then, but efficiency has suffered at the cost of reducing time (**Table 1.6**).

Dopaminergic (DA) neurons play a key role in regulating reflexive actions and is implicated in Parkinson's disease (PD). One of the first groups to differentiate hiPSCs into DA neurons was Chambers et al. in 2008. Introducing the dual SMAD inhibition patterning technique using NOGGIN and SB435142 for the first time, this groundbreaking study produced DA neurons in 19 days with 82 percent efficiency.[57]

Having a selection of different types of neurons available from hiPSC differentiation is critical in carrying out screens for different neurological and neurodegenerative diseases, however screening with these cells is still in its infancy. Early screens have been carried out using dividing neuro progenitor cells (NPCs) as these cells are still scalable and homogenous[52; 58]. However, NPCs do not have the full disease phenotype and thus reaction of mature neurons to compound treatment cannot be fully ascertained. Of the instances listed in (**Table 1.7**) where iPSC-derived neurons were used to model diseases in the past four years, in only a few cases were they actually used in screening campaigns.

In targeting Parkinson's disease Scwab and Ebert created sensory neurons at 20% efficiency after a 21 day differentiation period from patients carrying the LRRK2 G2019S mutation. In studying the morphology and function of theses neurons using imaging techniques they found the presence of large microtubule-containing neurite aggregations as well as altered calcium dynamics. When treated with three LRRK2 kinase inhibitors LRRK2-IN-1, GSK2578215A, AND CZC25146 they observed a significant, but partial rescue in morphology and a full rescue in calcium dynamics. These findings supported the idea that kinase activity is implicated in PD neuronal dysfunction. It also showed minor line-to-line differences due to patient variability in the iPSCs used which is a partial hindrance to screening with iPSC-derived neurons. Furthermore, although a full screen was not executed, this study showed that small molecules could be tested on hiPSC-derived neurons and valuable information retrieved.

Probably the best demonstration of hiPSC-derived screening has been associated with FXS. Two separate screens were published in 2015; however neither used fully mature neurons. Using a high content assay Kaufmann et al. screened 50,000 compounds to see which ones upregulated FMRP production in neural precursor cells. The study concluded with several compounds that produced a small but detectable increase in FMRP. Moreover it showed the feasibility of plating iPSC-derived cells in high-density well plates.[59] Kumari et al. used at 1536-well plate format and screened 5,000 compounds on neural stem cells using a time-resolved fluorescence resonance energy transfer (TR-FRET)-based assay to measure increases in FMRP. TR-FRET is an assay format in which a donor

fluorophore, when excited by a light source, releases energy towards a nearby acceptor fluorophore which in turn emits a specific fluorescent wavelength which is detected. Using this technique, this study concluded with six compounds that modestly increased FMRP production, however this work provided proof of principal for using TR-FRET in this format with patient iPSC-derived cells.[60]

In HD, there have been recent studies performed on hiPSC-derived neurons; however these studies have only used these neurons to validate compounds discovered in larger primary screens. Kumar et al. created mesencephalic dopaminergic neurons in 26 days for a study to better elucidate the intracellular processes that regulate neuronal manganese (Mn) homeostasis. Following a 40,167 compound primary screen based on a fluorescence Mn measurement assay, 9 compounds were selected for validation on the hiPSC-derived neurons and interestingly all nine showed varying activity at different stages of maturation of the neurons. Such a study would not be possible in animal or postmortem models, thus this work demonstrated more accurately the possible use of these compounds to regulate Mn levels in humans.[61]

Recently another screen was performed targeting HD treatment. Combining in vitro single molecule fluorescence spectroscopy, in silico molecular docking simulations, and in vivo fly and mouse HD models, 19,468 physical compounds were screened for inhibitors of abnormal interactions between mutant HTT and Ku70, a mutation repair protein. Fifty-six hits were produced from this primary screen and three were tested on HD patient derived cortical neurons. Using confocal microscopy and immunocytochemistry, it was concluded that these compounds

improved dendrite length and spine density, but did not reduce the number of inclusion body positive neurons present. Taken together however, treating these neurons illustrated the therapeutic effectiveness of these compounds.[62]

1.5.3 Challenges of hiPSC-derived Neurons

From the previous examples, it is clear that screening on hiPSC-derived neurons is still in its infancy, and has a long way to go before it is commonplace. There are significant reasons why screening with hiPSC-derived neurons has not accelerated, and these challenges must be overcome to unlock the true potential of this technology. These challenges include biologic, logistic, and economic factors.

One of the major threats to screening with hiPSC-derived neurons is the possibility of the existence of genetic mutations separate from the disease as well as epigenetic memory from the somatic tissue of origin. Historically, iPSCs have been generated via a lentiviral or retroviral reprogramming process, however these techniques can lead to mutations at the integration site, copy number variations, or abnormal karyotypes.[63] These genetic aberrations could possibly lead to problems during differentiation and may affect the final disease phenotype.

New strategies using transgene-free techniques have been employed to minimize or eliminate the negative effects caused by the early reprograming methods. Excisable factors have been developed including floxed lentiviral and transposon vectors, while non-integrating factors such as adenoviral, plasmids, Sendai viruses, mRNA transfections, recombinant proteins, RNA viruses, and miRNA viruses have also been developed. Furthermore, small molecules such as

valproic acid, vitamin C, SB431542, PD0325901, thiazovinin, sodium butyrate, and forskolin have demonstrated improved reprogramming results when utilized.

Another genetic challenge for hiPSCs and their resulting neurons is the threat of retaining genetic information from the original somatic cells from which they were derived from. In their paper in Nature, Kim et al. was one of the first to report that low-passage iPSCs harbor residual DNA methylation signatures characteristic of their somatic tissue of origin. Furthermore, these residual signatures favored differentiation along lineages of the donor cell as opposed to alternate cell types. They also showed that this 'epigenetic memory' could be reset via serial reprogramming or by treatment of iPSCs with chromatin-modifying drugs.[64] In a similar vein Liester et al. showed that somatic memory was independent of reprogramming techniques.[65]. Increasing passage number and culture time however could possibly reduce these effects and make iPSCs behave more like ESCs.[66; 67]

Apart from the genetic concerns, another major challenge is having access to consistent iPSC lines. Disease phenotypes should be the same among iPSC lines with the same gene mutations. This is true for lines derived from the same patient, or different patients even though they have a different genetic background. However, this is not always the case, and environmental factors sometimes interfere.[68; 69] In order to increase reliability and reproducibility large panels of well characterized iPSC lines from a wide cohort of patients representing the mosaic nature of most neuropsychiatric and neurodevelopmental diseases should be organized and properly maintained. In this spirit, repositories such as the Coriell Institute for

Medical Research, the HD consortium, and the UK Biobank have been established. Furthermore, it is important for screening campaigns to use multiple iPSC lines to ensure that disease-specific cellular phenotypes are detected beyond this normal variability.

Having proper controls is also vital. Historically, controls have consisted of iPSCs generated from age, gender, and race matched healthy donors, but these controls are not ideal because of the previously mentioned genetic variability across patients. For these reasons, it is critical to be able to isogenically correct the disease mutations from the same patient lines as are used in the screen.[70; 71] It is also critical to characterize those cells for precise disease related phenotypic readouts to ensure they are safe controls. Fortunately there are a number of tools available today to create these isogenic lines including zinc finger nucleases (ZFNs), transcription activator-like effector nucleases (TALENS)[72], and clustered regularly interspaced short palindromic repeates-CRISPR-associated protein-9 nuclease (CRISPR-Cas9) and these tools are being increasingly used.[73-75]

The final major challenge of screening with hiPSC-derived neurons is the ability to generate large numbers of homogenous cells. Currently it is possible expand neural progenitor cells, but these cells do not provide the rich phenotypic information of mature neurons, and are not ideal for modeling neurodegenerative diseases which are typically late-onset. Protocols must be developed that improve differentiation efficiencies, however many of the measures taken already, such as non-integrating factors and small molecules, have increased developmental costs. Furthermore, in creating large populations of homogenous neurons, it is also

necessary to characterize these cells for their type, maturity, and functionality which require additional time.

1.6 Summary

The pharmaceutical industry is consolidating, and in the process R&D is being outsourced to academic drug discovery centers which are supported by public research funding. With this outsourced R&D, greater focus has been put on treating neurological disorders. There are a number of well characterized neurological disorders that have no cure and only limited symptomatic treatments. Failures of promising therapies in clinical trials have followed successful preclinical studies on non-human models. For these reasons there is greater attention on the use of hiPSC-derived neurons for preclinical drug development. This technology has yet to be used in a wide spread manner however because of the high costs associated with differentiation, characterization, and control preparation. Furthermore, due to low efficiencies and long differentiation times, there is a demand for new technology to increase cellular throughput. Development in microfluidics has increased to address this demand, however the main hindrance of this technology is its limited capacity for extended cell culture.

	DRUG	COMPANY	Dis/Sym	PRECLINIC IN-VITRO	PRECLINIC IN-VIVO	PHASE I	PHASE II	PHASE III
1	Tetrabenazine (Xenazine)	Lundbeck	Sym					
2	Dimebon (latrepirdine)	Medivation (Pfizer)	Sym					FAILED
3	Coenzyme Q10	Huntington Study Group	Sym					FAILED
4	SD-809ER (AUSTEDO)	Auspex Pharma	Sym					
5	Cysteamine (RP103)	Raptor Pharma	Sym					
6	PBT2 (Reach2HD)	Prana Biotechnology	Sym					
7	PDE10A Inhibitor (PF-02545920)	Pfizer	Sym				FAILED	
8	Pridopidine (Pride HD)	Teva Pharmaceuticals	Sym				FAILED	
9	Laquinimod (LEGATO-HD)	Teva Pharmaceuticals	Sym					
10	PDE10A Inhibitor	Omeros Corp	Sym				FAILED	
11	VX15	Vaccinex	Sym					
12	PBF-999	Palobiofarma	Sym			FAILED		
13	Anti-sense Oligonucleotides (ASOs)	Roche and Ionis Pharma	Dis					
14	Kynurenine mono-oxygenase (KMO) inhibitor	CHDI Foundation	Sym					
15	HDAC Inhibitor	CHDI Foundation and Biomarin	Sym					
16	AAV-SHRNA	Genzyme, Sanofi, Voyager Therapeutics	Dis					
17	Zinc Finger DNA-Binding Protein (ZFP)	Shire, Sangamo	Dis					
18	Pro289	Prosensa	Dis					
19	Caspase 6 Inhibitor	Teva Pharmaceuticals	Dis					

Table 1.1. Current therapies in the pipeline to treat Huntington's Disease

	DRUG	COMPANY	Dis/Sym	PRECLINIC IN-VITRO	PRECLINIC IN-VIVO	PHASE I	PHASE II	PHASE III
1	STX209 (Arbaclofen)	Seaside Therapeutics	Sym					FAILED
2	Sertraline	UC Davis	Sym					
3	Oxytocin	Stanford	Sym					
4	Donepezil	Stanford	Sym					
5	Basimglurant (RO4917523)	Roche	Sym					FAILED
6	NNZ-2566 (Trofinetide)	Neuren	Sym					
7	Metadoxine (MG01CI)	Alcobra	Sym					
8	CX516	RespireRx	Sym					
9	Mavoglurant (AFQ056)	Novartis	Sym				FAILED	
10	Ganaxolone	Marinus Pharmaceuticals	Sym					
11	Minocycline	UC Davis	Sym					
12	Lithium	FRAXA	Sym					

Table 1.2. Current therapies in the pipeline to treat fragile X syndrome

	DRUG	COMPANY	Dis/Sym	PRECLINIC IN-VITRO	PRECLINIC IN-VIVO	PHASE I	PHASE II	PHASE III
1	GSK2402968 (Pro-051)	GlaxoSmithKline	Dis					FAILED
2	Tadalafil	Eli Lilly	Sym					FAILED
3	Drisapersen	BioMarin Pharmaceutical	Sym					FAILED
4	Idebenone	Santhera Pharmaceuticals	Sym					
5	Oxatomide	CINRG	Sym					
6	AVI-4658	Imperial College London	Dis					
7	ACE-031	Acceleron Pharma	Sym				FAILED	
8	PTC124 (Ataluren)	PTC Therapeutics	Sym				FAILED	
9	BMN053 (Pro-053)	BioMarin Pharmaceutical	Dis				FAILED	
10	BMN044 (Pro-044)	BioMarin Pharmaceutical	Dis				FAILED	
11	Halofuginone (HT-100)	Akashi Pharmaceuticals	Sym				FAILED	
13	SRP-4045	BioMarin Pharmaceutical	Dis					
14	Flavocoxid	University of Messina	Sym					
15	SMT C100 (Ezutromid)	Summit Therapeutics	Sym					
16	TAS-205	Taiho Pharmaceutical	Sym					
17	Eplerenone	Ohio State	Sym					

Table 1.3. Current therapies in the pipeline to treat Duchenne Muscular Dystrophy

	DRUG	COMPANY	Dis/Sym	PRECLINIC IN-VITRO	PRECLINIC IN-VIVO	PHASE I	PHASE II	PHASE III
1	4-AP (Dalfampridine-ER, Ampyra)	Columbia University	Sym					
2	Riluzole	Hopitaux de Paris	Sym					
3	Olesoxime	Roche/Genentech	Sym					
4	ISIS-SMNRx	Ionis Pharmaceiuticals	Sym					
5	Nusinersen	Biogen/Ionis	Sym					
6	CK-2127107	Cytokinetics/Astellas	Sym					
7	RG7916	Roche/PTC/SMA Foundation	Dis					
8	LMI070 (NVS-SM1)	Novartis	Sym			FAILED		
9	RG7800 (RO7034067) (RO6885247)	Roche/PTC/SMA Foundation	Dis			FAILED		
10	AVXS-101	AveXis	Dis					

Table 1.4. Current therapies in the pipeline to treat spinal muscular atrophy

	DRUG	COMPANY	Dis/Sym	PRECLINIC IN-VITRO	PRECLINIC IN-VIVO	PHASE I	PHASE II	PHASE III	
1	Idebenone (Catena)	Santhera Pharmaceuticals	Sym						FAILED
2	Pioglitazone	Assistance Publique - Hopitax de Paris	Sym						FAILED
3	Interferon gamma (Actimmune)	Horizon	Dis						FAILED
4	EPI-743	Edison	Sym						
5	SHP622 (VP 20629 or OX1)	Shire	Sym						
6	Lu AA24493 (cEPO)	H. Lundbeck A/S	Sym					FAILED	
7	alpha-tocopherolquinone (EPI-A0001)	Edison Pharmaceuticals	Sym					FAILED	
8	RT001 (dPufas)	Retrotope	Sym						
9	Resveratrol	Jupiter Therapeutics	Dis						
10	Deferiprone (Ferriprox)	ApoPharma	Sym					FAILED	
11	Epoetin Alfa (Erythropoietin or EPO)	Federico II University	Sym						
12	Egb 761	Ipsen	Sym					FAILED	
13	Verenicline (Chantix)	University of South Florida & Pfizer	Sym				FAILED		
14	Nicotinamide	Imperial College	Dis						

Table 1.5. Current therapies in the pipeline to treat Friedreich's ataxia.

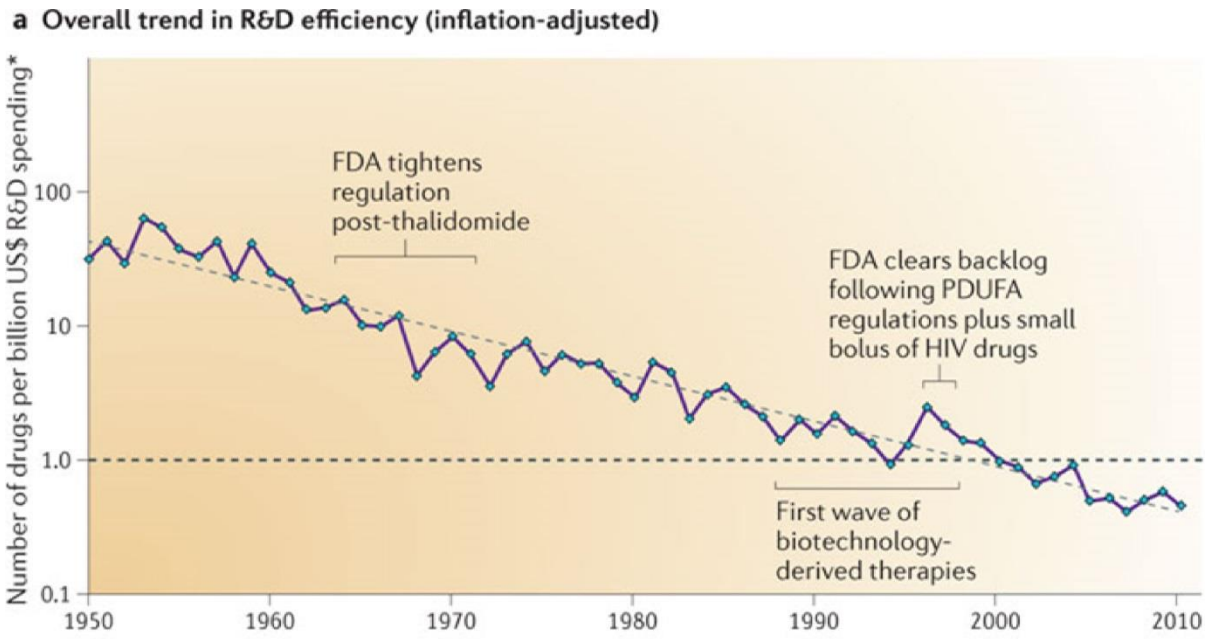

Figure 1.1. The number of new drugs approved by the US Food and Drug Administration (FDA) per billion US dollars (inflation-adjusted) spent on research and development (R&D) has halved roughly every 9 years.[30]

A | Approvals of new chemical entities by the US FDA: 1940–2010.

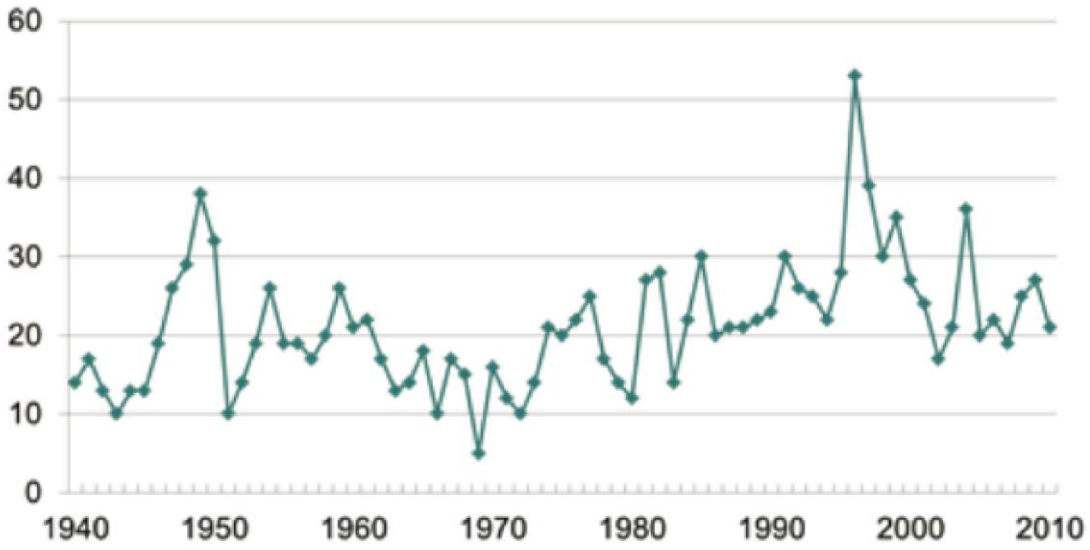

Figure 1.2. Approvals of new chemical entities by the US FDA: 1940-2010.[28]

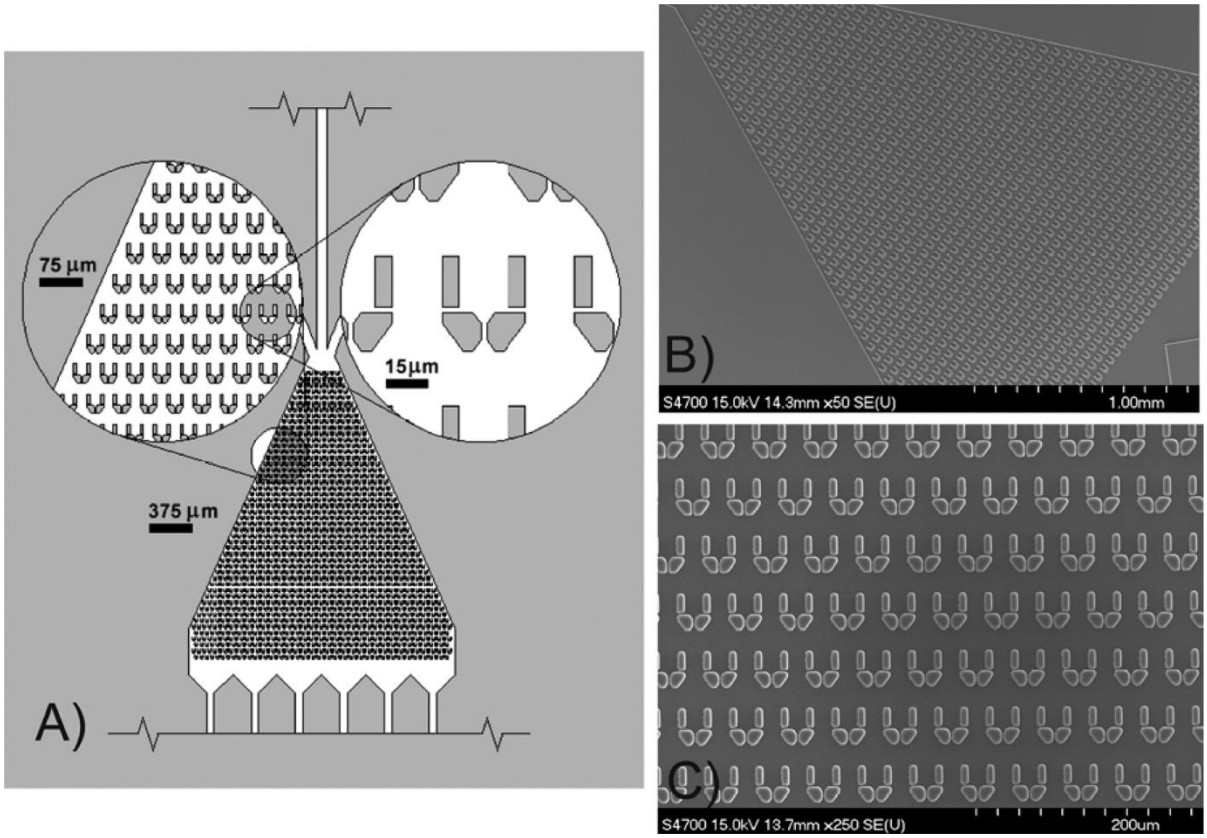

Figure 1.3. Microfluidic live-cell array (array cytometer). (A) CAD schematic of the chip layout showing a triangular microculture chamber, containing the cell trapping array. (B and C) SEM images of the array of PDMS cell traps.[36]

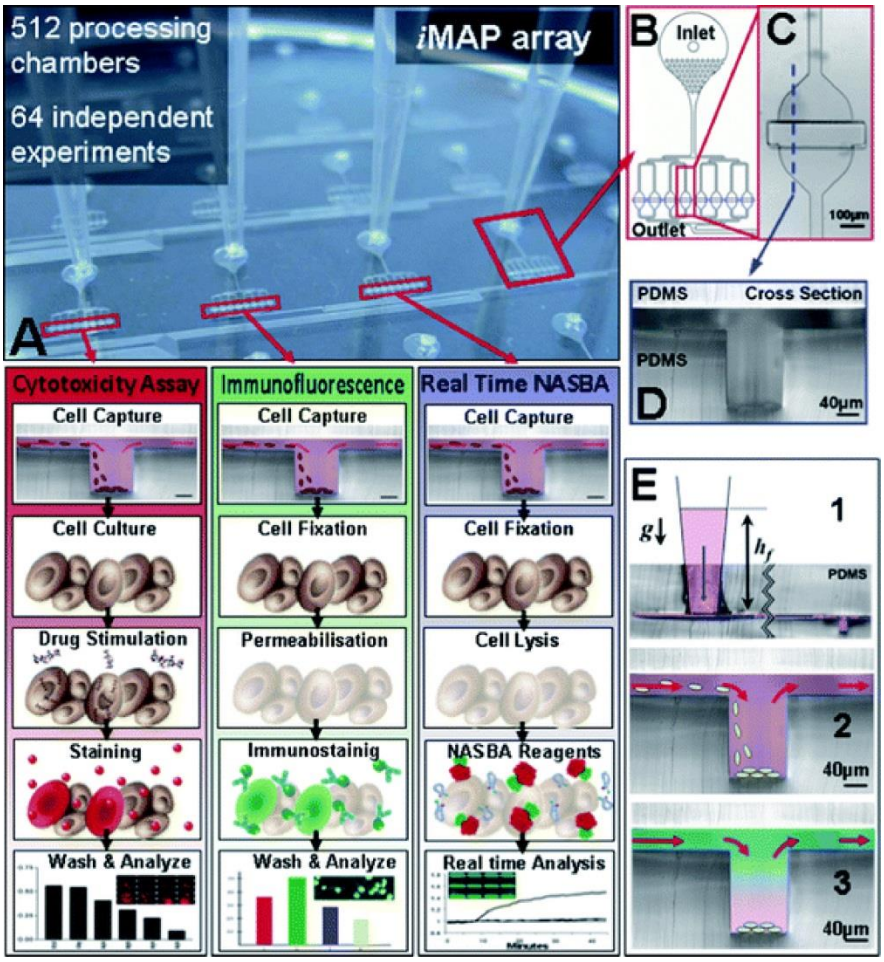

Figure 1.4. iMAP array (A) consists of 64 processing modules (B) that can perform 64 independent simultaneous integrated assays. The integrated function of each processing module can be flexibly selected by the user and depends entirely on the sequence and timing of the fluid inputs. The basic steps required for three different cell based assays are illustrated (A). This versatility allows the user to combine cell stimulation and gene and protein expression analysis on a single microfluidic platform. For statistical replication purposes each module consists of 8 parallel and equally distributed (C) processing chambers that contain a central trench structure (D). Each processing chamber can execute any sequence laboratory unit operations (E), gravity driven flow (E1), cell capture (E2) and reagent loading and mixing (E3).[37]

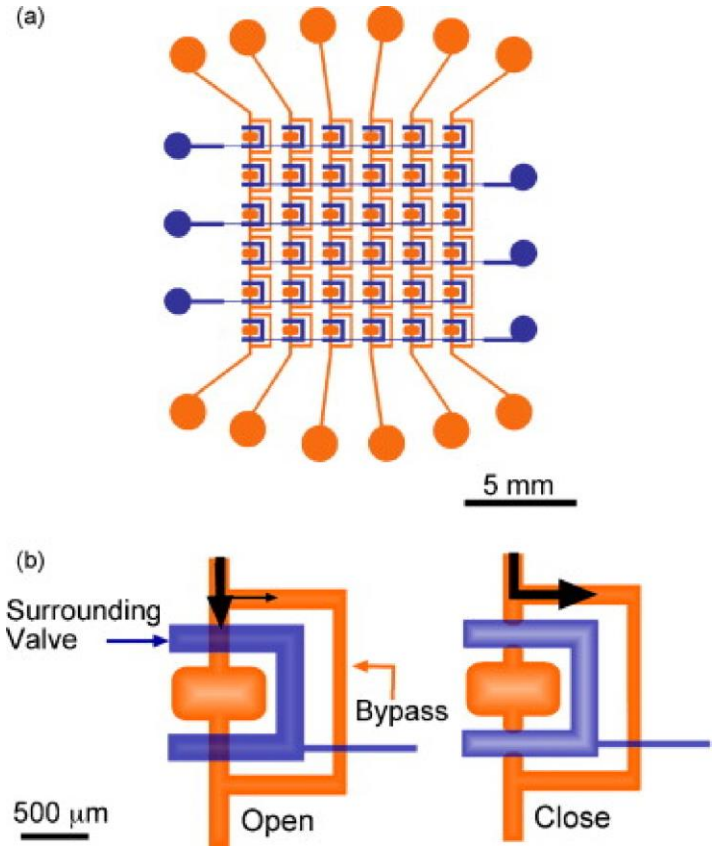

Figure 1.5. (a) The schematic of the multilayer microfluidic cell array. The fluidic channels and chambers (in the fluidic layer) are shown in orange while the surrounding valves (in the control layer) are shown in blue. (b) The operation of a surrounding valve and the microfluidic culture chamber under its control. The channel depth is 18 μm in the fluidic layer and 25 μm in the control layer. The sample flows mainly through the chamber when the valve is open due to the higher flow resistance in the bypass channel. The sample flows through the bypass channel when the valve is closed. (For interpretation of the references to color in this figure legend, the reader is referred to the web version of the article.)[38]

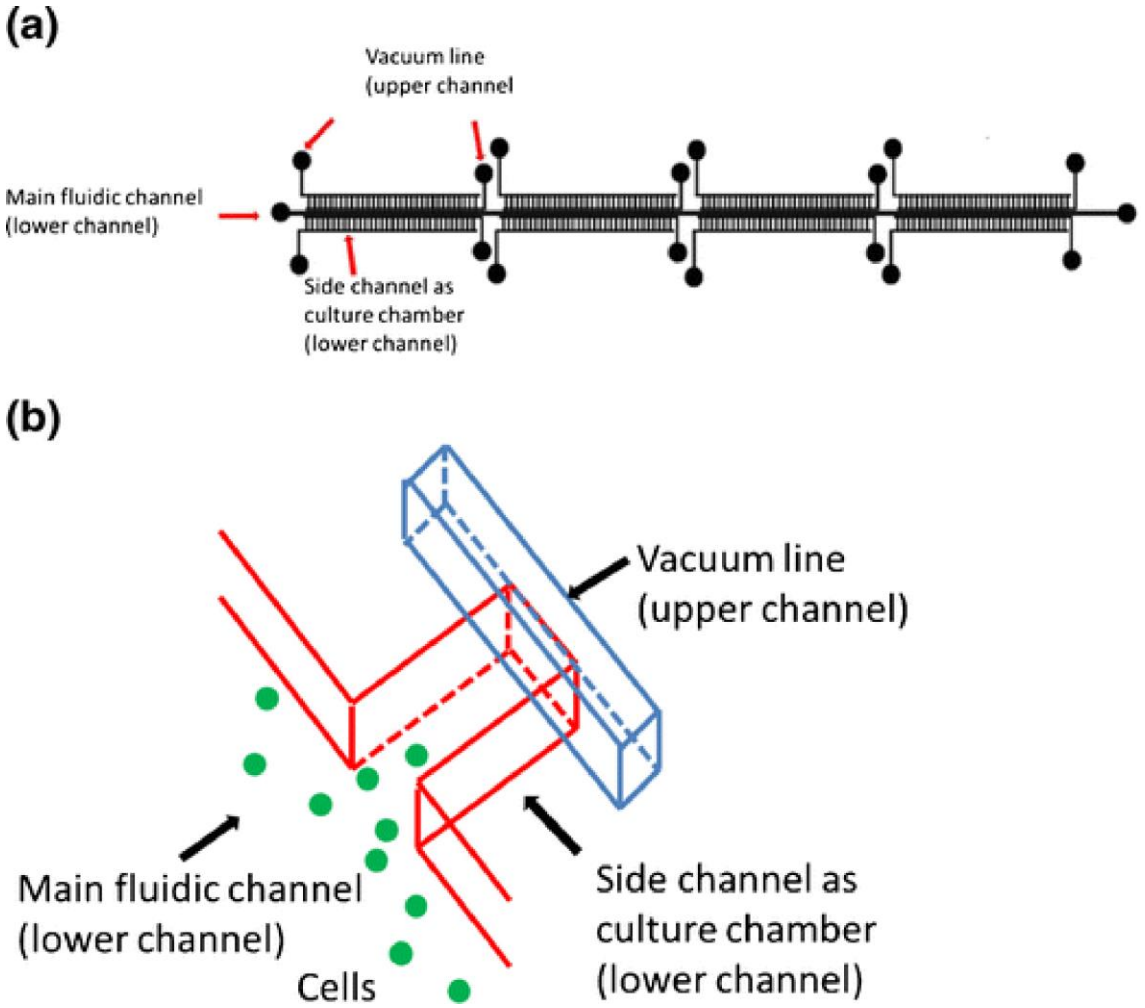

Figure 1.6. a) Overview of device design. b) A closeup of the culture wells. The main fluidic channel was 5.5 cm long and 300 µm wide, while side channels were 1 mm long and 150 µm wide. There were 128 repeat side channel units on each side of the main channel. The 256 culture channels were divided into 8 regions of 32 culture channels. 2 control channels were located above the side channels on each region (8 control channels total), on the neck and end of side channels, respectively. The control line on the end was used for vacuum actuation. The line on the neck was used as a debubbler to remove air in channels.[39]

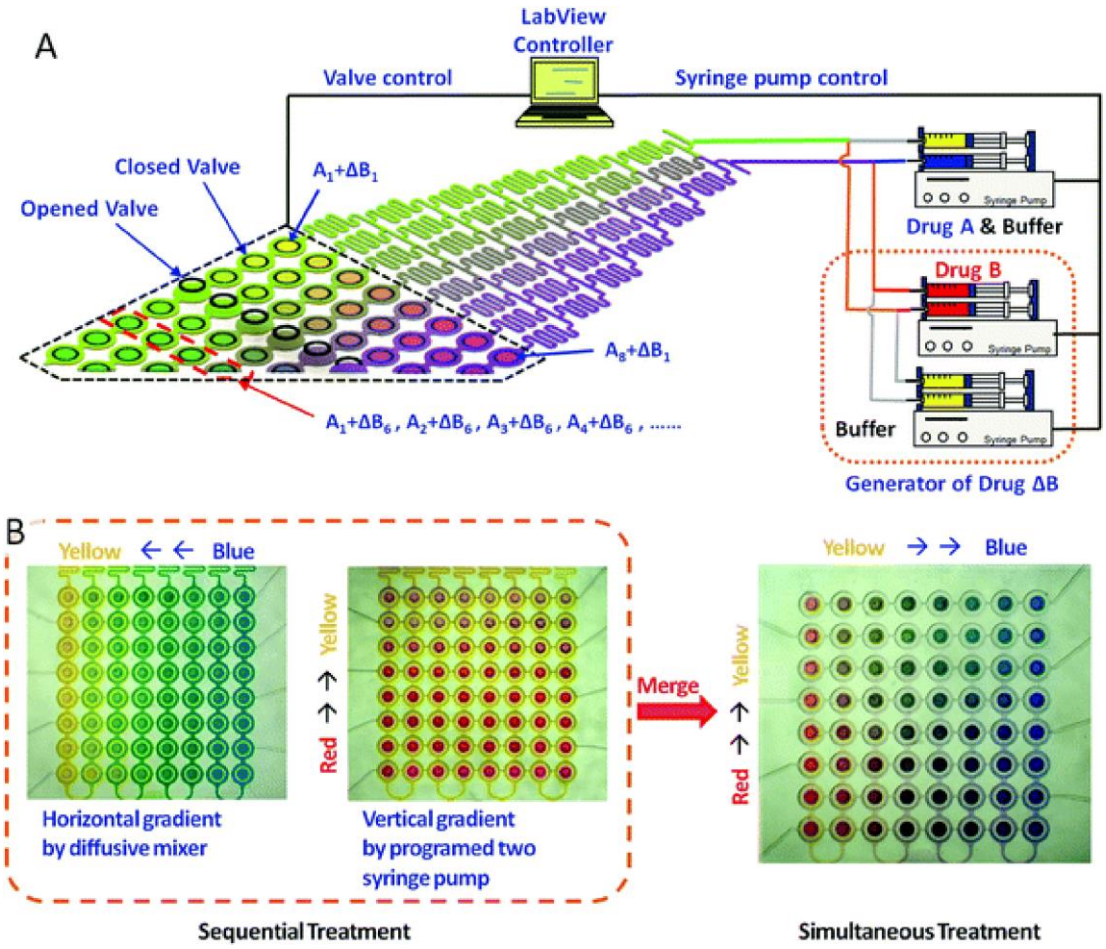

Figure 1.7. Schematic of the microfluidic array. (A) Different concentrations of drugs A and B are generated in the diffusive gradient mixer, and used, either sequentially or in combination, to perfuse cells cultured in downstream microchambers. The mixing operation for generating different drug combinations and the opening and closing of valves for perfusing cells in the microchambers are controlled through a LabVIEW interface. (B) Depiction of the range of concentrations that can be generated for sequential and simultaneous treatment using color dyes. In the left panel, yellow and blue color dye solutions (representing the minimum and maximum concentrations of one drug) are mixed to generate eight outlet concentrations (''horizontal gradient'' of colors between yellow and blue), and represent the gradient used in sequential exposure experiments. In the middle panel, yellow and red streams (representing the minimum and maximum concentrations of the second drug) are mixed together to generate a ''vertical gradient'' of colors between yellow and red. Merging the two color gradients (vertical direction concentration gradient: yellow to blue; horizontal direction concentration gradient: yellow to red) yields an array of pair-wise combinations, and represents the gradient used in simultaneous exposure experiments (right panel).[40]

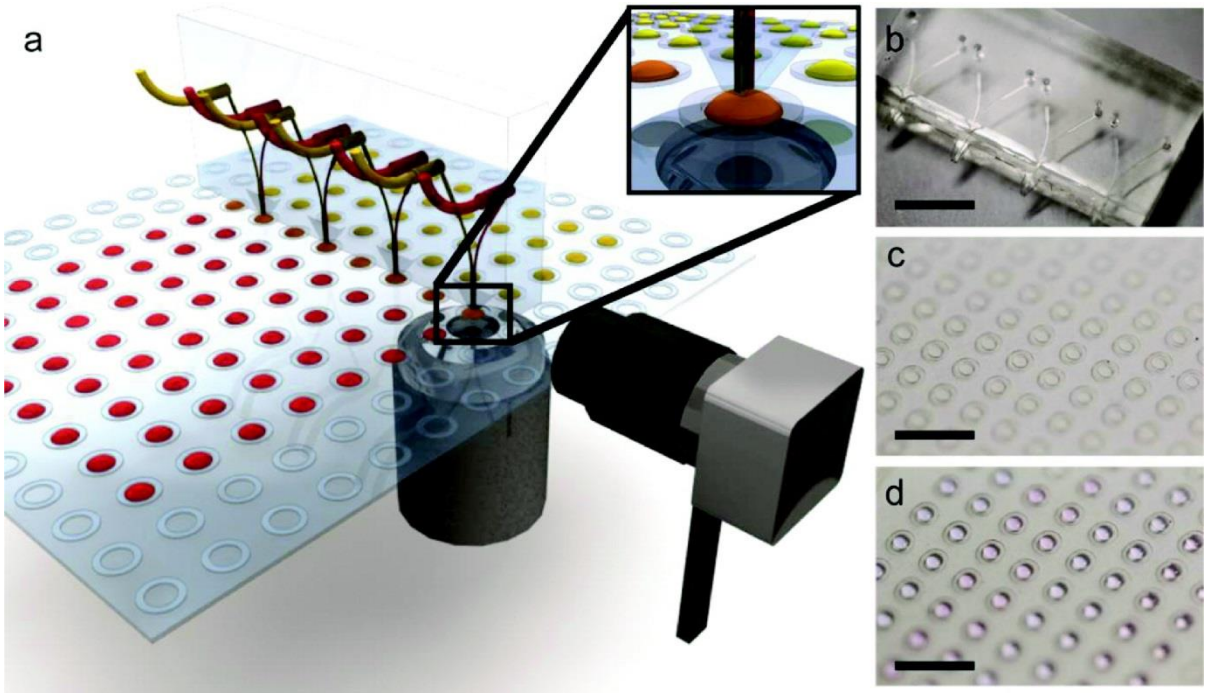

Figure 1.8. The microfluidic liquid handling system. (a) A microfluidic chip was aligned to the microwell chip horizontally and vertically using a microscope and a camera. Inset: a close view of the outlet of the microfluidic pipet chip. (b) A four-channel microfluidic liquid pipet chip. (c) Before and (d) after the microwell chip was filled with ~350 nL of liquid sample in each well. Scale bars are 5 mm.[41]

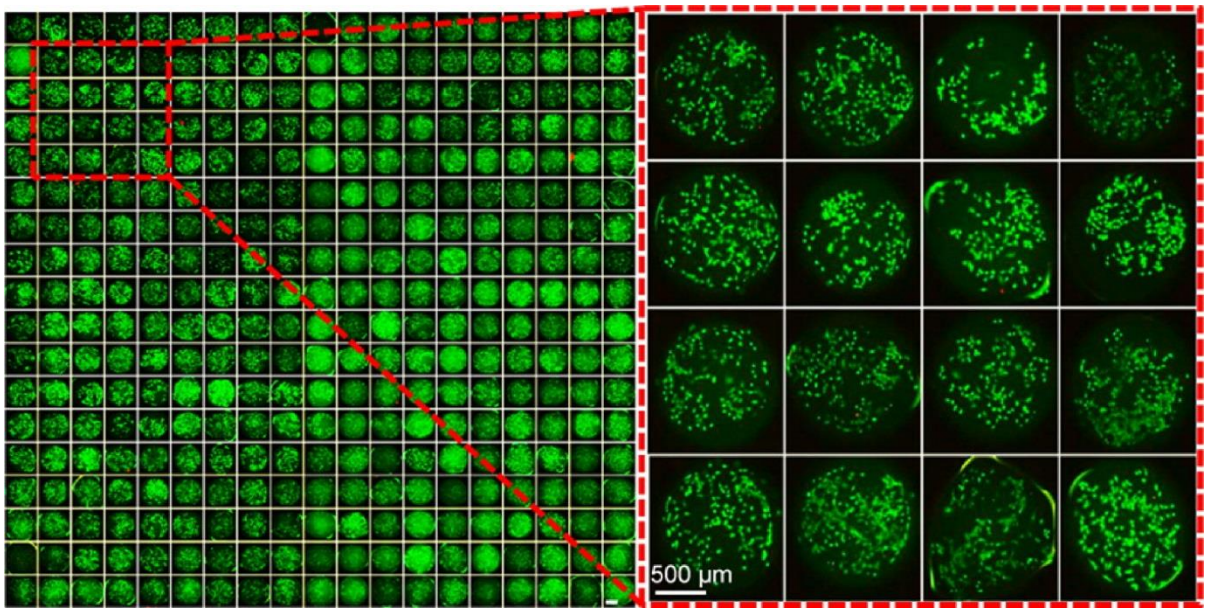

Figure 1.9. Fluorescence images of an on-chip array of 342 droplets with A549 cells.[42]

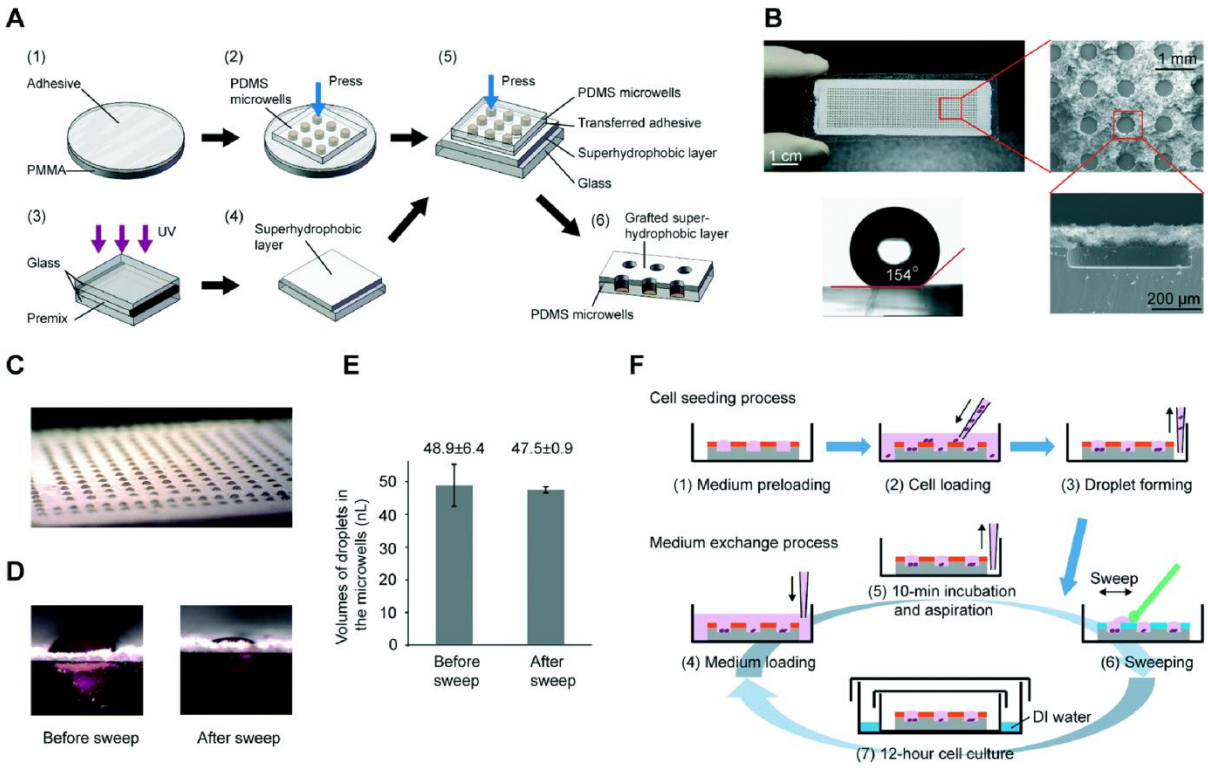

Figure 1.10. Superhydrophobic microwell array chip (SMARchip) and operation procedure. (A) Micrografting procedure for fabricating the SMARchip. (B) Photos and scanning electron micrographs of the SMARchip. The SMARchip consists of a microfabricated polydimethylsiloxane (PDMS) microwell array and a superhydrophobic polymer layer. (C) A droplet array of culture medium spontaneously forming in the microwells due to the repelling effect of the superhydrophobic layer on the aqueous solution. (D) Typical side-views of the droplets in microwells before and after a sweep with a cell spreader. (E) Average volumes and standard deviations of droplets in microwells with a depth of 200 µm before and after a sweep. The volumes were calculated from the side-views of the microwells (n = 10). (F) Experimental procedures for cell seeding and medium exchange on the SMARchip.[43]

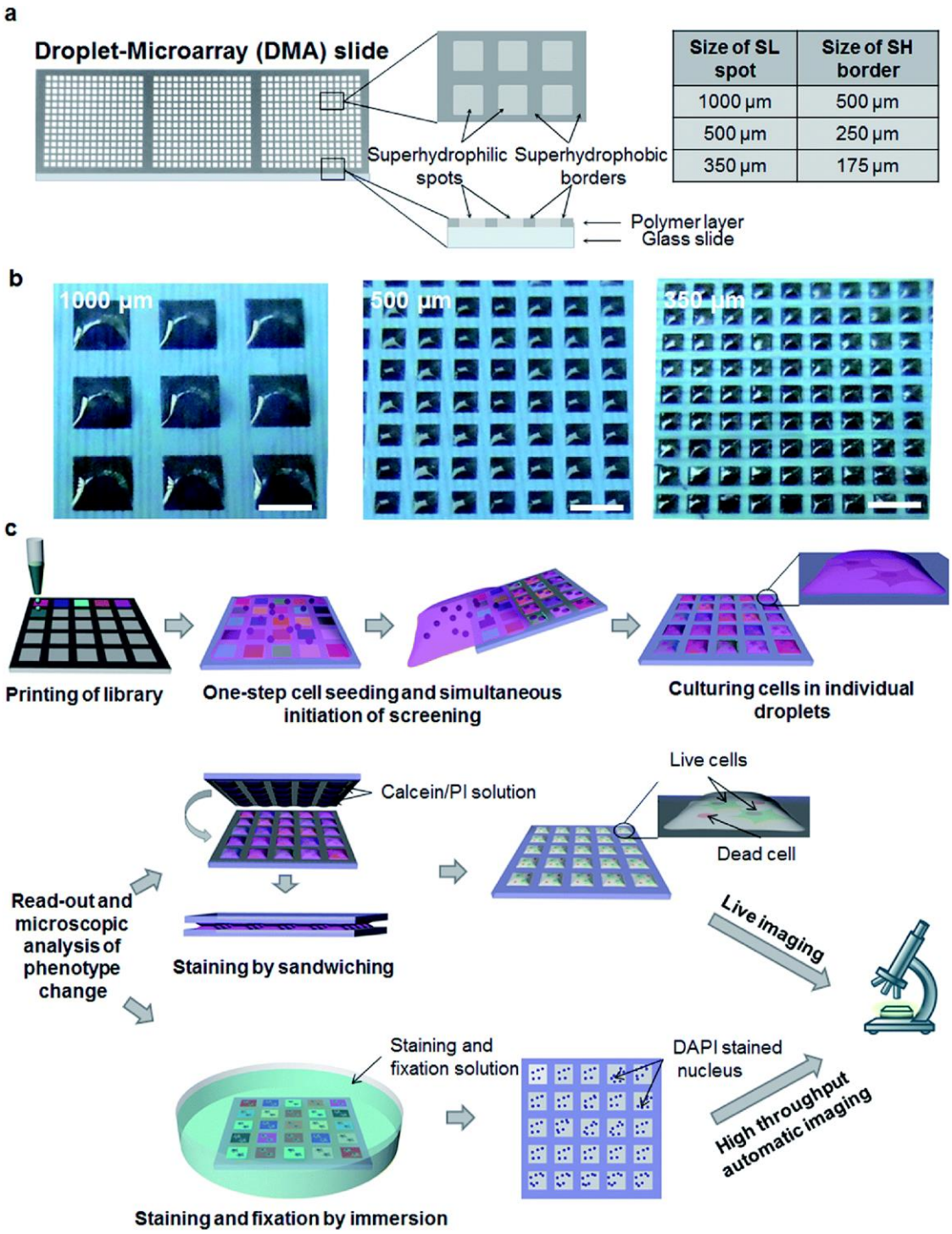

Figure 1.11. Droplet-microarray (DMA) reverse cell screening platform. (a) Schematic representation of a DMA slide and a table showing the sizes of the superhydrophilic spots and corresponding superhydrophobic borders. (b) Photographs of droplet microarrays. Scale bar 1mm. (c) Schematic diagram of the workflow of reverse cell screening using a DMA platform.[44]

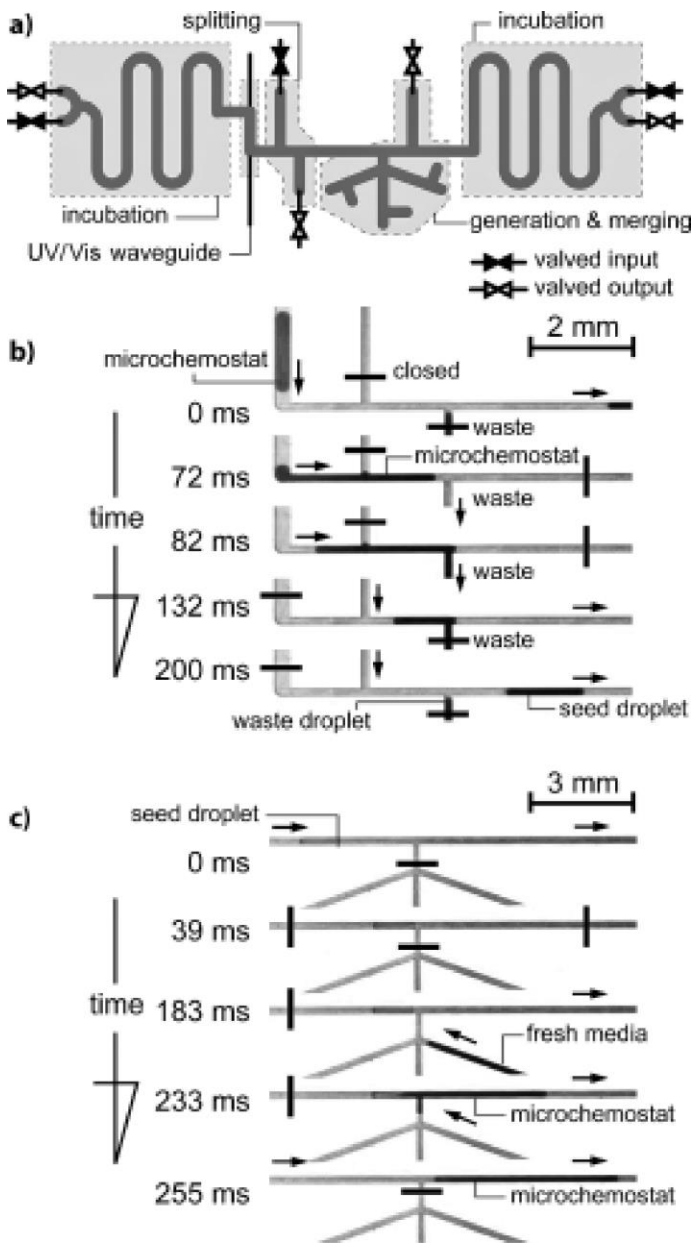

Figure 1.12. a) Diagram of the layout of the microfluidic device. b) A sequence of micrographs illustrating the splitting of one microdroplet into a seed droplet and waste droplets with pre-programmed volumes. c) A sequence of micrographs illustrating the fusion of the seed droplet with fresh media to control the chemical composition and number of cells in a microdroplet.[45]

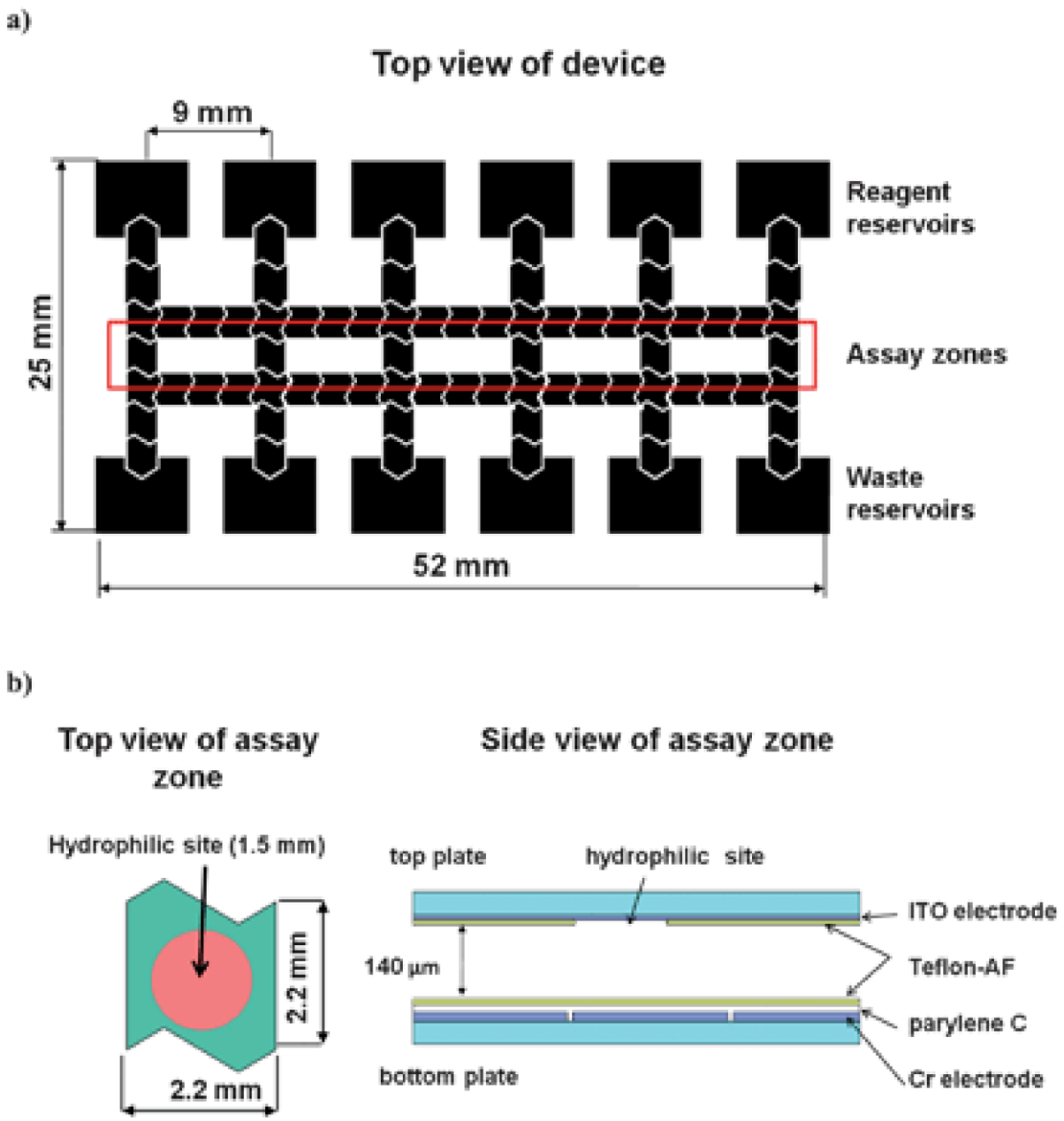

Figure 1.13. DMF device used for multiplexed cell-based assays. a) Top-view schematic of full device bearing six assay zones. b) Top- and side-view schematics of one assay zone.[46]

	Neuronal Type	Year	Reprogramming Protocol	Differentiation Protocol	Yield	Differentiation Time	Characterization	Reference
1	Motor Neurons	2008	lentiviral (OCT4, SOX2, NANOG, LIN28)	Retinoic acid (RA), sonic hedgehog (SHH)	9.50%	42-56	HOXB4, OLIG2, ISL1, HB9, SMI32, CHAT	Ebert A., Nature, 2009
2	Motor neurons	2009	lentiviral, phosphoglycerate kinase (PGK) promoter	SMAD signaling inhibitors (Noggin and SB431542)	Not listed	19	ISL1 and HB9	Chambers S., Nature Biotechnology, 2009
3	Motor neurons	2012	episomal plasmid	All-trans retinoic acid, purmoorphamin	17.10%	28-70	Olig2, HB9, ISL1, Lhx1, SMI-32	Sareen D., Plos One, 2012
4	Motor neurons	2014	Sendai virus		90% (MNX1)	21-30	MNX1,ISL1, CHAT, electrophysiology	Chen H., Cell Stem Cell, 2014
5	Motor neurons	2014	lentiviral, compound C	Activin and BMP inhibition via RA and SHH	8-13%	20	SMI32, HB9, CHAT	Qu Q., Nature Communications, 2014
6	Cortical neurons	2010	self-inactivating lentivirus (SIN)	embryoid aggregate, no growth factors	86%	35	OTX2, LHX2	Zeng, Hui, Plos One, 2010
7	Cortical neurons	2012	lentiviral, phosphoglycerate kinase (PGK)	SMAD signaling inhibitors (Noggin and	95%	60-90	Pax6, OTX 1/2	Shi, Yichen, Nature Neuroscience, 2012
8	Cortical neurons	2013	Sendai virus	SMAD signaling inhibitors (Noggin and	70%	21	SOX5, CTIP2, CUX1, CUX2, BRN1, BRN2	Boissart C., Translational Psychiatry, 2013
9	Dopaminergic neurons	2009	lentiviral, phosphoglycerate kinase (PGK)	SMAD signaling inhibitors (Noggin and	82%	19	ISL1 and HB9	Chambers S., Nature Biotechnology, 2009
10	Dopaminergic neurons	2013	retrovirus	SMAD signal inhibition (dorsomorphin,	35%	55-60	TH, FOXA2, TUBBIII	Reinhardt, Peter, PlosOne, 2013
11	Dopaminergic neurons	2014	Sendai virus	SMAD signal inhibition (LDN193189,	5-15%	11-35	SOX1, FOXA2, LMX1, TH, GIRK2	Woodward, Chris, Cell Reports, 2014

Table 1.6 hiPSC-derived neuron types

	Disease	Starting Cells	Derived Cells	Diff Protocol	Diff Time	Yield	Phenotype demonstrated	Characterization	Screen (Y/N)	Reference
1	ALS	fibroblasts (C9ORF72)	motor neurons	All-trans retinoic acid (ATRA), purmorphamine (PMN)	39-84	33-45%	Southern Blot	SMI32, CHAT, electrophysiology	N	Sareen et al., Science Translation Medicine, 2013
2	ALS	fibroblasts	motor neurons	embyoid aggregates, SMAD inhibitor (SB431542)and dorsomorphin	42-56	15%	Q-PCR	HB9, CHAT, P75ntr	N	Diana Toli, Neurobiology of Disease, 2015
3	ALS	fibroblasts	motor neurons	retinoic acid (RA), smo agonist (SAG), purmorphamine (PUR)	31	35%	increased yH2AX, p53, ATR, GADD45	CHAT	N	Rodrigo Lopez-Gonzalez, Neuron, 2016
4	ALS	fibroblasts (D90A SOD1 mutation)	motor neurons	SB431542, retinoic acid (RA), purmorphamine	21-30	77%	RT-PCR, Western Blot	CHAT, MNX1, TUJ1	N	Hong Chen, Cell Stem Cell, 2014
5	ALS	fibroblasts (FUS, TDP-43)	spinal cord neurons	SMAD inhibitors (SB431542, dorsomorphin), RA, PUR	28-34	15%	RT-PCR	OLIG2,HB9, ISL1, CHAT	N	Jessica Lenzi, Disease Models & Mechanisms, 2015
6	ALS	fibroblasts (hnRNP A2/B1 D290V)	motor neurons	SMAD inhibitors (SB431542, dorsomorphin), RA, SAG	46-53	not listed	E-clip, 866 clusters in 527 genes	HB9, ISLET1, SMI31	N	Fernando Martinez, Neuron, 2016
7	PD	fibroblasts (heterozygous GBA1 mutations)	mid-brain dopanminergic neurons	floor-plate-based, modified SMAD inhibition (CHIR)	40-65	15-20%	Q-PCR	TH+, FOXA2, NURR1, GIRK2, VMAT2	N	David Schoendorf, Nature Communications, 2014
8	PD	fibroblast (hetero deletion of exon 3 and 5, homo deletion of exon 3)	dopaminergic neurons	embryoid aggregates with SB431542, FGF, SHH	45-50	not listed	RT-PCR	TH+, FOXA2, AADC, DAT, VMAT2	N	Yong Ren, Stem Cells, 2015
9	PD	fibroblast (LRRK2 G2019S)	sensory neurons	EZ spheres, FGF-8, purmorphammine,	21-28	20%	Western Blot	BIII tubulin, peripherin, TrkA, TRPV1	LIMITED	Andrew Schwab, Stem Cell Reports, 2015
10	AD	epithelial & fibroblast (non-patient)	cortical neurons	SMAD inhibitors	30-39	20%	Western Blot-TAU	TBR1, CTIP2	N (screening assay)	X. Medda, J. Biomolecular Screening, 2016
11	AD	epithelial (non-patient)	cortical neurons	SMAD inhibitors	35-70		Western Blot - TAU	TBR1, CTIP2,	N (screening assay)	An Verheyen, Plos One, 2015
12	AD	fibroblast (FAD1, A246E PS1, M146L PS1 Mutation)	NPCs	dual-SMAD inhibitors, TGFB	35-55	79%	Q-PCR	Tuji1, nestin, CD56	N	Andrew Sproul, Plos One, 2014
13	AD	fibroblasts (APP-V7171 mutation)	cortical neurons	embryoid body	24-100	not listed	Western Blot, Q-PCR	Cux1, Tbr1	N	Christina Muratore, Human Molecular Genetics, 2014
14	AD	fibroblasts (FAD)	cortical neurons	embryoid aggregates with SHH	40-100	90%	Q-PCR	VGLUT1, KCC2, VGAT, NMDAR, MAP2, TAU	N	Mei-Chen Liao, Neurobiology of Disease, 2016
15	FXS	fibroblasts	NPCs	dual-SMAD Inhibitors - FGF	19	87%	Southern Blot, PCR	CD24, CD184, CD44	Y (50K cmpds)	Markus Kaufmann, J. Biomolecular Screening, 2015
16	FXS	fibroblasts, lymphoblastoid (full mutation)	NSCs	not listed	>14	not listed	Southern Blot, PCR	Nestin, Pax6, Sox2	Y (5K cmpds)	Daman Kumari, Stem Cells Translational Medicine, 2015
17	ASD	fibroblasts (SHANK-3 mutation)	cortical neurons (based on Boissart)	BMP inhibitor (Noggin), Nodal inhibitor (SB431542), EGF, FGF	21-28	not listed	RT-PCR	not listed	Y (202 cmpds)	Helene Darville, EbioMedicine, 2016
18	FXS	fibroblasts (FM)	cortical neurons	dual-SMAD inhibitors	28 - 44	not listed	RT-PCR	FOXG1	N	Matthew Doers, Stem Cells and Development, 2014
19	HD	not listed	mesencephalic dopaminergic neurons	floor-plate-based, dual SMAD inhibition - SHH, Purmoprhamine, FGF8, CHIR	26	not listed	PCR	TH+, B3-Tubulin, LMX1A	Y (secondary - 9 cmpds)	Kevin Kumar, Scientific Reports, 2014
20	HD	CS92iHD57n9 iPSC line (CAG repeat 57)	cortical neurons	dual SMAD inhibition	28-35	72%	G-Banding Analysis	Cux1, Tbr1	Drug validation (3 cmpds)	Tomomi Imamura, Scientific Reports, 2016
21	HD	fibroblast (109 CAG repeat)	NPCs	EZ spheres, FGF, EGF	42	40%	RT-PCR	Nestin, DARPP32	N	Virginia Mattis, Human Molecular Genetics, 2015

Table 1.7. hiPSC-derived disease models

1.8: BIBLIOGRAPHY

1. Shoulson I, Schwid S, Hyson C, Oakes D, Gorbold E, Rudolph A, Shinaman A, Kamp C, Kieburtz K, Lang A et al. 2007. Mixed lineage kinase inhibitor cep-1347 fails to delay disability in early parkinson disease. Neurology. 69(15):1480-1490.

2. Pammolli F, Magazzini L, Riccaboni M. 2011. The productivity crisis in pharmaceutical r&d. Nature Reviews Drug Discovery. 10(6):428-438.

3. Gray M, Shirasaki DI, Cepeda C, Andre VM, Wilburn B, Lu XH, Tao JF, Yamazaki I, Li SH, Sun YE et al. 2008. Full-length human mutant huntingtin with a stable polyglutamine repeat can elicit progressive and selective neuropathogenesis in bachd mice. Journal of Neuroscience. 28(24):6182-6195.

4. Miller J, Arrasate M, Shaby BA, Mitra S, Masliah E, Finkbeiner S. 2010. Quantitative relationships between huntingtin levels, polyglutamine length, inclusion body formation, and neuronal death provide novel insight into huntington's disease molecular pathogenesis. Journal of Neuroscience. 30(31):10541-10550.

5. Lynch G, Kramar EA, Rex CS, Jia YS, Chappas D, Gall CM, Simmons DA. 2007. Brain-derived neurotrophic factor restores synaptic plasticity in a knock-in mouse model of huntington's disease. Journal of Neuroscience. 27(16):4424-4434.

6. Yero T, Rey JA. 2008. Tetrabenazine (xenazine), an fda-approved treatment option for huntington’s disease–related chorea. Pharmacy and Therapeutics. 33(12):690-694.

7. Ghosh A, Michalon A, Lindemann L, Fontoura P, Santarelli L. 2013. Drug discovery for autism spectrum disorder: Challenges and opportunities. Nature Reviews Drug Discovery. 12(10):777-790.

8. Bear MF, Huber KM, Warren ST. 2004. The mglur theory of fragile x mental retardation. Trends Neurosci. 27(7):370-377.

9. Hoffman EP, Bronson A, Levin AA, Takeda S, Yokota T, Baudy AR, Connor EM. 2011. Restoring dystrophin expression in duchenne muscular dystrophy muscle progress in exon skipping and stop codon read through. American Journal of Pathology. 179(1):12-22.

10. Koenig M, Kunkel LM. 1990. Detailed analysis of the repeat domain of dystrophin reveals 4 potential hinge segments that may confer flexibility. Journal of Biological Chemistry. 265(8):4560-4566.

11. Huard J, Mu X, Lu A. 2016. Evolving paradigms in clinical pharmacology and therapeutics for the treatment of duchenne muscular dystrophy. Clinical Pharmacology & Therapeutics. 100(2):142-146.

12. Hoffman EP, Brown RH, Kunkel LM. 1987. Dystrophin - the protein product of the duchenne muscular-dystrophy locus. Cell. 51(6):919-928.

13. Cirak S, Feng L, Anthony K, Arechavala-Gomeza V, Torelli S, Sewry C, Morgan JE, Muntoni F. 2012. Restoration of the dystrophin-associated glycoprotein complex after exon skipping therapy in duchenne muscular dystrophy. Molecular Therapy. 20(2):462-467.

14. Aartsma-Rus A, Janson AAM, Kaman WE, Bremmer-Bout M, den Dunnen JT, Baas F, van Ommen GJB, van Deutekom JCT. 2003. Therapeutic antisense-induced exon skipping in cultured muscle cells from six different dmd patients. Human Molecular Genetics. 12(8):907-914.

15. Asai A, Sahani N, Kaneki M, Ouchi Y, Martyn JAJ, Yasuhara SE. 2007. Primary role of functional ischemia, quantitative evidence for the two-hit mechanism, and phosphodiesterase-5 inhibitor therapy in mouse muscular dystrophy. Plos One. 2(8):16.

16. Carlson TJ, Pellerin A, Djuretic IM, Trivigno C, Koralov SB, Rao A, Sundrud MS. 2014. Halofuginone-induced amino acid starvation regulates stat3-dependent th17 effector function and reduces established autoimmune inflammation. Journal of Immunology. 192(5):2167-2176.

17. McGivern JV, Patitucci TN, Nord JA, Barabas MEA, Stucky CL, Ebert AD. 2013. Spinal muscular atrophy astrocytes exhibit abnormal calcium regulation and reduced growth factor production. Glia. 61(9):1418-1428.

18. Mehta NM, Newman H, Tarrant S, Graham RJ. 2016. Nutritional status and nutrient intake challenges in children with spinal muscular atrophy. Pediatric Neurology. 57:80-83.

19. Tisdale S, Pellizzoni L. 2015. Disease mechanisms and therapeutic approaches in spinal muscular atrophy. Journal of Neuroscience. 35(23):8691-8700.

20. 2015 sma researcher meeting summary: drug discovery. 2015. Cure SMA; [accessed]. http://www.curesma.org/news/2015-researcher-meeting-drug-discovery.html?referrer=https://www.google.com/).

21. Palacino J, Swalley SE, Song C, Cheung AK, Shu L, Zhang XL, Van Hoosear M, Shin Y, Chin DN, Keller CG et al. 2015. Smn2 splice modulators enhance u1-pre-mrna association and rescue sma mice. Nature Chemical Biology. 11(7):511-+.

22. Naryshkin NA, Weetall M, Dakka A, Narasimhan J, Zhao X, Feng ZH, Ling KKY, Karp GM, Qi HY, Woll MG et al. 2014. Smn2 splicing modifiers improve motor function and longevity in mice with spinal muscular atrophy. Science. 345(6197):688-693.

23. Strawser CJ, Schadt KA, Lynch DR. 2014. Therapeutic approaches for the treatment of friedreich's ataxia. Expert Review of Neurotherapeutics. 14(8):949-957.

24. Martineau L, Noreau A, Dupre N. 2014. Therapies for ataxias. Current Treatment Options in Neurology. 16(7):13.

25. What is fa? Friedreich's Ataxia Research Alliance - CureFA.org; [accessed 2017]. http://www.curefa.org/whatis.

26. Diagnosis of ataxia. National Ataxia Foundation; [accessed 2017]. http://ataxia.org/learn/ataxia-diagnosis.aspx.

27. DiMasi JA, Grabowski HG, Hansen RW. 2016. Innovation in the pharmaceutical industry: New estimates of r&d costs. Journal of Health Economics. 47:20-33.

28. LaMattina JL. 2011. The impact of mergers on pharmaceutical r&d. Nature Reviews Drug Discovery. 10(8):559-560.

29. Schnee JE. 1979. R and d strategy in the united-states pharmaceutical-industry. Research Policy. 8(4):364-382.

30. Scannell JW, Blanckley A, Boldon H, Warrington B. 2012. Diagnosing the decline in pharmaceutical r&d efficiency. Nature Reviews Drug Discovery. 11(3):191-200.

31. Scannell JW, Bosley J. 2016. When quality beats quantity: Decision theory, drug discovery, and the reproducibility crisis. Plos One. 11(2):21.

32. Russo E. 2003. Special report: The birth of biotechnology. Nature. 421(6921):456-457.

33. Dworkin RH, Kirkpatrick P. 2005. Pregabalin. Nature Reviews Drug Discovery. 4(6):455-456.

34. Richman DD. 2001. Antiretroviral activity of emtricitabine, a potent nucleoside reverse transcriptase inhibitor. Antiviral Therapy. 6(2):83-88.

35. Muhsin M, Gricks C, Kirkpatrick P. 2004. Pemetrexed disodium. Nature Reviews Drug Discovery. 3(10):825-826.

36. Wlodkowic D, Faley S, Zagnoni M, Wikswo JP, Cooper JM. 2009. Microfluidic single-cell array cytometry for the analysis of tumor apoptosis. Analytical Chemistry. 81(13):5517-5523.

37. Dimov IK, Kijanka G, Park Y, Ducree J, Kang T, Lee LP. 2011. Integrated microfluidic array plate (imap) for cellular and molecular analysis. Lab on a Chip. 11(16):2701-2710.

38. Wang HY, Bao N, Lu C. 2008. A microfluidic cell array with individually addressable culture chambers. Biosensors & Bioelectronics. 24(4):613-617.

39. Gao Y, Li P, Pappas D. 2013. A microfluidic localized, multiple cell culture array using vacuum actuated cell seeding: Integrated anticancer drug testing. Biomedical Microdevices. 15(6):907-915.

40. Kim J, Taylor D, Agrawal N, Wang H, Kim H, Han A, Rege K, Jayaraman A. 2012. A programmable microfluidic cell array for combinatorial drug screening. Lab on a Chip. 12(10):1813-1822.

41. Zhou Y, Pang YH, Huang YY. 2012. Openly accessible microfluidic liquid handlers for automated high-throughput nanoliter cell culture. Analytical Chemistry. 84(5):2576-2584.

42. Du GS, Pan JZ, Zhao SP, Zhu Y, den Toonder JMJ, Fang Q. 2013. Cell-based drug combination screening with a microfluidic droplet array system. Analytical Chemistry. 85(14):6740-6747.

43. Zhang PF, Zhang JX, Bian ST, Chen ZY, Hu YW, Hu RW, Li JQ, Cheng YC, Zhang XC, Zhou YM et al. 2016. High-throughput superhydrophobic microwell arrays for investigating multifactorial stem cell niches. Lab on a Chip. 16(16):2996-3006.

44. Popova AA, Demir K, Hartanto TG, Schmitt E, Levkin PA. 2016. Droplet-microarray on superhydrophobic-superhydrophilic patterns for high-throughput live cell screenings. Rsc Advances. 6(44):38263-38276.

45. Jakiela S, Kaminski TS, Cybulski O, Weibel DB, Garstecki P. 2013. Bacterial growth and adaptation in microdroplet chemostats. Angewandte Chemie-International Edition. 52(34):8908-8911.

46. Bogojevic D, Chamberlain MD, Barbulovic-Nad I, Wheeler AR. 2012. A digital microfluidic method for multiplexed cell-based apoptosis assays. Lab on a Chip. 12(3):627-634.

47. Dragunow M. 2008. Opinion - the adult human brain in preclinical drug development. Nature Reviews Drug Discovery. 7(8):659-U610.

48. Allman JM, Tetreault NA, Hakeem AY, Park S. 2011. The von economo neurons in apes and humans. American Journal of Human Biology. 23(1):5-21.

49. Steffenhagen C, Kraus S, Dechant FX, Kandasamy M, Lehner B, Poehler AM, Furtner T, Siebzehnrubl FA, Couillard-Despres S, Strauss O et al. 2011. Identity, fate and potential of cells grown as neurospheres: Species matters. Stem Cell Reviews and Reports. 7(4):815-835.

50. Grskovic M, Javaherian A, Strulovici B, Daley GQ. 2011. Induced pluripotent stem cells - opportunities for disease modelling and drug discovery. Nature Reviews Drug Discovery. 10(12):915-929.

51. Takahashi K, Tanabe K, Ohnuki M, Narita M, Ichisaka T, Tomoda K, Yamanaka S. 2007. Induction of pluripotent stem cells from adult human fibroblasts by defined factors. Cell. 131(5):861-872.

52. McNeish J, Roach M, Hambor J, Mather RJ, Weibley L, Lazzaro J, Gazard J, Schwarz J, Volkmann R, Machacek D et al. 2010. High-throughput screening in embryonic stem cell-derived neurons identifies potentiators of alpha-amino-3-hydroxyl-5-methyl-4-isoxazolepropionate-type glutamate receptors. Journal of Biological Chemistry. 285(22):17209-17217.

53. Di Giorgio FP, Boulting GL, Bobrowicz S, Eggan KC. 2008. Human embryonic stem cell-derived motor neurons are sensitive to the toxic effect of glial cells carrying an als-causing mutation. Cell Stem Cell. 3(6):637-648.

54. Ebert AD, Yu JY, Rose FF, Mattis VB, Lorson CL, Thomson JA, Svendsen CN. 2009. Induced pluripotent stem cells from a spinal muscular atrophy patient. Nature. 457(7227):277-U271.

55. Li XJ, Zhang XQ, Johnson MA, Wang ZB, LaVaute T, Zhang SC. 2009. Coordination of sonic hedgehog and wnt signaling determines ventral and dorsal telencephalic neuron types from human embryonic stem cells. Development. 136(23):4055-4063.

56. Eiraku M, Watanabe K, Matsuo-Takasaki M, Kawada M, Yonemura S, Matsumura M, Wataya T, Nishiyama A, Muguruma K, Sasail Y. 2008. Self-organized formation of polarized cortical tissues from escs and its active manipulation by extrinsic signals. Cell Stem Cell. 3(5):519-532.

57. Chambers SM, Fasano CA, Papapetrou EP, Tomishima M, Sadelain M, Studer L. 2009. Highly efficient neural conversion of human es and ips cells by dual inhibition of smad signaling. Nature Biotechnology. 27(3):275-280.

58. Zhao WN, Cheng CL, Theriault KM, Sheridan SD, Tsai LH, Haggarty SJ. 2012. A high-throughput screen for wnt/beta-catenin signaling pathway modulators in human ipsc-derived neural progenitors. Journal of Biomolecular Screening. 17(9):1252-1263.

59. Kaufmann M, Schuffenhauer A, Fruh I, Klein J, Thiemeyer A, Rigo P, Gomez-Mancilla B, Heidinger-Millot V, Bouwmeester T, Schopfer U et al. 2015. High-throughput screening using ipsc-derived neuronal progenitors to identify compounds counteracting epigenetic gene silencing in fragile x syndrome. Journal of Biomolecular Screening. 20(9):1101-1111.

60. Kumari D, Swaroop M, Southall N, Huang W, Zheng W, Usdin K. 2015. High-throughput screening to identify compounds that increase fragile x mental retardation protein expression in neural stem cells differentiated from fragile x syndrome patient-derived induced pluripotent stem cells. Stem cells transl med. AlphaMed Press.

61. Kumar R, Kumari B, Srivastava A, Kumar M. 2014. Nrfampred: A proteome-scale two level method for prediction of nuclear receptor proteins and their sub-families. Scientific Reports. 4:7.

62. Imamura T, Fujita K, Tagawa K, Ikura T, Chen XG, Homma H, Tamura T, Mao Y, Taniguchi JB, Motoki K et al. 2016. Identification of hepta-histidine as a candidate drug for huntington's disease by in silico-in vitro- in vivo-integrated screens of chemical libraries. Scientific Reports. 6:15.

63. Laurent LC, Ulitsky I, Slavin I, Tran H, Schork A, Morey R, Lynch C, Harness JV, Lee S, Barrero MJ et al. 2011. Dynamic changes in the copy number of pluripotency and cell proliferation genes in human escs and ipscs during reprogramming and time in culture. Cell Stem Cell. 8(1):106-118.

64. Kim K, Doi A, Wen B, Ng K, Zhao R, Cahan P, Kim J, Aryee MJ, Ji H, Ehrlich LIR et al. 2010. Epigenetic memory in induced pluripotent stem cells. Nature. 467(7313):285-U260.

65. Lister R, Pelizzola M, Kida YS, Hawkins RD, Nery JR, Hon G, Antosiewicz-Bourget J, O'Malley R, Castanon R, Klugman S et al. 2011. Hotspots of aberrant epigenomic reprogramming in human induced pluripotent stem cells. Nature. 471(7336):68-U84.

66. Nishino K, Toyoda M, Yamazaki-Inoue M, Fukawatase Y, Chikazawa E, Sakaguchi H, Akutsu H, Umezawa A. 2011. Dna methylation dynamics in human induced pluripotent stem cells over time. Plos Genetics. 7(5):14.

67. Hussein SM, Batada NN, Vuoristo S, Ching RW, Autio R, Narva E, Ng S, Sourour M, Hamalainen R, Olsson C et al. 2011. Copy number variation and selection during reprogramming to pluripotency. Nature. 471(7336):58-U67.

68. Abyzov A, Mariani J, Palejev D, Zhang Y, Haney MS, Tomasini L, Ferrandino AF, Belmaker LAR, Szekely A, Wilson M et al. 2012. Somatic copy number mosaicism in human skin revealed by induced pluripotent stem cells. Nature. 492(7429):438-+.

69. Regal L, Vanopdenbosch T, Tilkin P, Van Den Bosch L, Thijs V, Sciot R, Robberecht W. 2006. The g93c mutation in superoxide dismutase 1 - clinicopathologic phenotype and prognosis. Archives of Neurology. 63(2):262-267.

70. Soldner F, Laganiere J, Cheng AW, Hockemeyer D, Gao Q, Alagappan R, Khurana V, Golbe LI, Myers RH, Lindquist S et al. 2011. Generation of isogenic pluripotent stem cells differing exclusively at two early onset parkinson point mutations. Cell. 146(2):318-331.

71. Liu GH, Qu J, Suzuki K, Nivet E, Li M, Montserrat N, Yi F, Xu XL, Ruiz S, Zhang WQ et al. 2012. Progressive degeneration of human neural stem cells caused by pathogenic lrrk2. Nature. 491(7425):603-607.

72. Hockemeyer D, Wang HY, Kiani S, Lai CS, Gao Q, Cassady JP, Cost GJ, Zhang L, Santiago Y, Miller JC et al. 2011. Genetic engineering of human pluripotent cells using tale nucleases. Nature Biotechnology. 29(8):731-734.

73. Hsu PD, Lander ES, Zhang F. 2014. Development and applications of crispr-cas9 for genome engineering. Cell. 157(6):1262-1278.

74. Schwank G, Koo BK, Sasselli V, Dekkers JF, Heo I, Demircan T, Sasaki N, Boymans S, Cuppen E, van der Ent CK et al. 2013. Functional repair of cftr by crispr/cas9 in intestinal stem cell organoids of cystic fibrosis patients. Cell Stem Cell. 13(6):653-658.

75. Wu YX, Liang D, Wang YH, Bai MZ, Tang W, Bao SM, Yan ZQ, Li DS, Li JS. 2013. Correction of a genetic disease in mouse via use of crispr-cas9. Cell Stem Cell. 13(6):659-662.

Chapter 2: Neuronal Cell Culture Performance of Microraft Arrays

2.1 Introduction

Currently 1536-well plates represent the most practical option for drug discovery researchers seeking the highest throughput for their cellular screening campaigns. The throughput advantage of these plates however comes with a cost. Using such high-density plates requires expensive equipment. Additionally, these plates suffer high rates of evaporation which threatens cell viability and physiology. In dealing with such issues, plates either must be sealed or cell growth must be limited to only a few days.

In 2016 Thorne et al used hESC-derived astrocytes to identify compounds that protect against oxidative stress. Using 1,536-well plates 4,000 astrocytes were plated in each well, however these cells were only maintained for up to 72 hours with media changes every 24 hours.[1] Similarly, in Dai et al., in testing a coating-free plating method for iPSC-derived neurons plated 3,000 cells per well in 1,536-well plates, but these cells were only maintained for 24 hours.[2]

To achieve longer cultures technical measures such as plate sealers must be implemented. In a high-content screen on mouse retinal neurons to identify compounds that are neuroprotective and promote photoreceptor differentiation, Fuller et al. plated 1,000 cells per well in 1,536-well plates and incubated them for up to 21 days. This extensive growth was achieved however using Breath-Easy gas-

permeable membranes (Diversified Biotech) and MicroClime vapor barrier lids (LabCyte).[3]

Microraft array technology represents a promising solution to the issues mentioned that have plagued other devices. Microraft arrays are culture devices consisting of approximately 1600 releasable paramagnetic particles (**Figure 2.1 A**). In the array, these particles are arranged in an orthogonal grid separated by PDMS borders. Cells are plated onto the device en masse, and each particle supports an individual subpopulation of cells for extended growth.

The Microraft arrays were originally developed by the Allbritton group at the University of North Carolina at Chapel Hill. Where this technology was originally developed for the isolation and sorting of specific cells from a heterogeneous population, this work explores the use of this technology for increasing throughput in neuron based drug screening. The fabrication of these microraft arrays follows a standard soft lithography process. Briefly, a photoresist master is created on a glass substrate upon which polydimethylsiloxane (PDMS) is poured and cast. After curing, the PDMS is then dipcoated into a poly (styrene-co-acrylic acid) solution containing 1 % wt./wt. γFe_2O_3 nanoparticles to form the individual Microraft particles. After curing, this assembly is then attached to a polystyrene culture cassette using additional PDMS as adhesive. The microraft array is currently being commercialized by Cell Microsystems, Inc. under the trademark CellRaft™ technology (U.S. patent #9,068,155 B2). The current devise being commercialized contains square particles with a side length of 250 µm. Throughout this dissertation, a modified array was used containing square particles with side lengths of 500 µm (**Figure 2.1A**). Larger

particles were chosen for these studies for easier manual use of the microraft array as well as a flatter profile, which is more beneficial for imaging given the concavity of each particle.

The microraft arrays were first described by Wang et al. in 2010 in “Lab on a Chip” as a device for single cell analysis. It has been tested in sorting heterogeneous populations of H1299 cells as well as the successful sorting of AsPC-1-Luc cells and subsequent transplantation into nude mice for tumor growth analysis.[4] More recently, this technology has been used to sort T-cells and Epstein Barr virus-infected lymphoblastoid cells.[5; 6] This new microraft technology was designed to replace a previous array device which used photoresist for its micro elements and a focus laser to release them.[7] The improved microraft array fabricated from poly (styrene-co-acrylic acid) polymer was shown to have extremely low auto fluorescence compared to the previously used photoresist materials. Furthermore in demonstrating the cell-culture functionality of the array, multiple cell types were cultured on the device. HeLa cells were cultured for up to 8 days on the intact array and >99% of cells were located within the wells on individual microrafts 20 minutes after plating and a single media wash. In addition to HeLa cells, Es129 embryonic stem cells were cultured for 50 h and pancreatic tumor cells from live donor were cultured for 23 days. Furthermore, cell viability following release of the microrafts from the PDMS substrate was assessed by releasing microrafts with a single HeLa cell and then observing the cell division. The results of these studies showed that 100% of the HeLa cells remained on the microraft surface, and after 144 h, 95 ± 8.7% of the single cells had formed small colonies.[8]

Initial tests of the microraft array with neuron cultures were performed in the Taylor lab by Mark Niedringhaus. The findings of these studies were published in Scientific Reports in 2015. In this research H9 embryonic stem cell derived neurons were first cultured on the microrafts to demonstrate their potential in expanding throughput for screening with stem cells. In the first set of experiments ESC-derived neurons were cultured for five days on the microrafts and neuronal markers MAP2 and VGLUT1 were positively expressed and the FM dye release rate was measured showing normal synaptic activity. In these experiments however, microrafts were released from the array and transferred to large volume well plates such as the 6 and 12-well variety. In another experiment, the cell viability of ESC-derived neurons was compared to those grown directly in 384-well plates. After five days of growth, the microrafts showed a significantly lower percentage of dead cells, however again, the microrafts were not transferred to large volume plates as opposed to high density 384-well plates.[9]

Typically 384-well plates support 5,000-20,000 neurons/well and 1,536-well plates support 1,000-5,000 neurons/well. Given a 1MM neuron/array plating density and ~1,600 microrafts/array each microraft supports between 300-500 neurons. Thus when looking at the high-end of these ranges the microraft array technology proposes a 40-fold increase in cellular throughput compared to plating directly in 384-well plates. Furthermore, if $1x10^6$ neurons were plated on 384-well plates at a density of 20,000 neurons/well, this would only facility the screening of 50 compounds compared to the 1,600 compounds promised from the microrafts when

the entire array is released and each microraft is distributed into individual wells (**Figure 2.1 B**).

Microraft arrays therefore have the unique advantage of being able to support fewer neurons than 1,536-well plates but still take advantage of the volume benefits of 384-well plates when transferred into their wells. Here the cell culture utility of microraft array technology in conjunction with the 384-well plate is demonstrated with hippocampal rat neurons as well as human ESC-derived neurons. The primary objective for these studies was to assess viability of these neurons following transfer from the microrafts and growth in multiwell plates.

2.2 Materials and Methods

2.2.1 Microraft arrays and well plates

Microraft arrays were fabricated according to previously published methods[8; 10]. Briefly, soft lithography was used to make the poly(dimethylsiloxane) (PDMS) template containing an array of microwells (each well has width x length x height = 500 µm x 500 µm x 200 µm, array size = 25.4 mm x 25.4 mm). The PDMS template was then dip coated with a 20% polystyrene solution in gamma-butyrolactone (GBL) containing 4% iron oxide particles. The arrays are then placed in a convection oven at 95°C for 16 hours to evaporate GBL to create the microrafts. The array was glued to a polystyrene cassette to facilitate handling, and then surface treated with air plasma (Harrick Plasma) for 2 min.

The 384-well microtiter plates used for this experiment were Small Volume, LoBase, Polystyrene, µClear, black, tissue-culture-treated, sterile (788092; Greiner

BioOne, Frickenhausen, Germany). The 1536-well microtiter plates used for this experiment were LoBase, F-bottom, Polystyrene, µClear, black, tissue-culture-treated, sterile (783092; Greiner BioOne, Frickenhausen, Germany).

2.2.2 Rat neuron culture

All animal procedures were carried out in accordance with the University of North Carolina at Chapel Hill Institutional Animal Care and Use Committee (IACUC). Dissociated hippocampal cultures were prepared at embryonic day 18 from Sprague Dawley rat embryos as previously described[11] with some modifications. Briefly, hippocampal tissue was dissected in dissociation media (DM) containing 82 mM Na2SO4, 30mM K2SO4, 5.8mM MgCl2, 0.25mM CaCl2, 1mM HEPES, 20mM Glucose and 0.001% Phenol red. Equal volumes of TrypLE Express (Invitrogen) and DM were added to the tissue and incubated at 37°C for 8 min. Tissue was then rinsed and gently triturated in Neurobasal media (NBM, Invitrogen) supplemented with 1x B27 (Invitrogen), 1x Antibiotic-antimycotic (Invitrogen), 1x Glutamax (Invitrogen). Dissociated cells were then centrifuged (67xg) for 7 minutes at 4°C, and resuspended (12x106 neurons/mL) in NBM. Prior to cell dissociation, the microraft array, 384-well plate, and the 1536-well plate were coated with poly-D-lysine (80 µg/mL; high molecular weight – 500-550 kDa) at 37˚C overnight and then rinsed three times with PBS. Neurons were then plated on each plate type at equivalent densities as shown below.

Initial Plating

	Area (mm^2)	Cells/well	Density ($cells/mm^2$)
Microraft	0.25	500	2000
384	2.66	5320	2000
1536	2.34	4680	2000

Neurons were maintained in NBM until 7 DIV at which time they were fixed and stained. Microrafts were released from their array after 2 DIV. We released and transferred the microrafts after 2 DIV because at this stage their processes are not long enough to extend over the PDMS borders between the microrafts while they are still embedded in the array. Waiting longer to release and transfer microrafts may cause injury to the neurons through shearing of processes that have grown over the borders.

2.2.3 Stem Cell Culture

The NIH-approved, human embryonic stem cell (ESC) line H9 (WA09) was obtained from WiCell Research Institute (Madison, WI). H9 ESCs were maintained as undifferentiated colonies on growth factor reduced Matrigel (BD Biosciences) in mTeSR1 media (StemCell Technologies). Media was changed daily. Cells were passaged every three days with 0.5 mM EDTA (340 mOs).

Differentiation was initiated with mTESR media supplemented with the SMAD inhibitors SB431542, LDN193189, and XAV939. These factors were incubated from Day 0-7 while retinoic acid was added on day 6. On day 7 embryo bodies were plated on laminin coated plates and switched to N2B27 differentiation media. At day

24, neuroprogeniter cells were plated on poly-D-lysine coated microraft arrays containing N2B27 media supplemented with BDNF.

2.2.4 Immunocytochemistry

The cell viability assay was performed as described previously with minor changes[12]. Briefly, cells were grown for 7 DIV and then stained with a solution containing Sytox Green Nucleic Acid Stain (1:1000; Life Technologies, Inc.) and DRAQ5 Fluorescent Probe (1:500; Thermo Scientific) in NBM for 5 minutes at room temperature to label dead/dying cell nuclei and all cell nuclei respectively. Following staining, the cells were rinsed three times for two minutes each with PBS and then fixed for 30 minutes with 4% formaldehyde. After fixation, cells were rinsed three times for two minutes each with PBS and finally placed in PBS before imaging.

2.2.5 Microscopy

Imaging was performed on an Andor XDi imaging system featuring a Yokogawa spinning disk confocal unit and an Olympus IX81-ZDC2 inverted microscope with a motorized stage by Ludl as described previously [13]. Montages were taken of each plate type with a 20X objective and stacks ranging from 10 – 20 slices each spaced 0.85 µm (z-distance) apart. Dead cells stained by Sytox were captured using a 488 nm laser excitation and a 525-30nm single band fluorescence filter (Semrock Brightline), while the cell nuclei representing all cells were captured using a 640 nm laser excitation and a 637-60nm single band fluorescence filter (Semrock Brightline).

2.2.6 Image processing and analysis

After acquisition, all images were analyzed with ImageJ as described previously [12]. Briefly, images were imported using the Bio-formats plugin, slices were summed using maximum intensity projection, and then converted to 8-bit. The projected images were thresholded and the number of stained nuclei were counted within a 300 µm diameter region of interest in the center of the rafts using the 'Analyze Particles' command.

2.2.7 Statistics

Statistical analysis was performed using GraphPad Prism 6 software. Percent dead was plotted as mean ± SEM. Statistical significance for the Viability vs. Well Plate experiment was tested with a one-way ANOVA using a Kruskal-Wallis test. Significance for the Viability vs. Cell Density and the viability of hESC-derived neuron experiments were tested with an ordinary one-way ANOVA using a Tukey's test. Significance with p-values < 0.001 are indicated with asterisks.

2.3 Results and Discussion

2.3.1 Rat Neuron Cell Culture

The objective of this study was to establish the process of culturing neurons on microraft arrays. The primary metric here was cell viability, but cell density and neurite outgrowth were also observed. Since 384 and 1536-well plates are commonly used in screening campaigns, culturing on microraft arrays was compared to these traditional plate types. After plating neurons on each substrate at equivalent densities of 2000 cells/mm^2 they were maintained for 7 DIV, and then

fixed and stained. To measure viability the cells were stained with Sytox (dead cells) and DRAQ 5 (all cells) and the viability was calculated as the ratio of Sytox positive cells to DRAQ 5 positive cells. DRAQ 5 was used in this study because the natural fluorescence of the microrafts interferes with Hoechst, DAPI, and other nuclear dyes in the blue wavelength range.

Although not statistically significant, the results showed the microrafts had a slightly better viability of 51% compared to 41% for the 384-well plate and 32% for the 1536-well plate (**Figure 2.2A**). In addition the final plating density was quantified to show the level of cell adhesion. This data showed that the microrafts had the largest final cell density with a mean of 1149 cells/mm^2 compared to 700 and 833 cells/mm^2 for the 384-well and 1536-well plates respectively (**Figure 2.2B**)

Once it was determined that the microrafts supported healthy neuron cultures, it was then necessary to determine the minimum total amount of cells to plate on the microrafts for a healthy culture. Since the goal in using the microraft arrays is to maximize throughput, it's important to minimize the amount of neurons on each microraft in order to do so. For these reasons cell densities of $1x10^6$, $1x10^5$, and $1x10^4$ cells/array were plated on three separate arrays, maintained for 8 DIV and then fixed and stained for the same viability measurements. Here it was found that $1x10^6$ cells/array performed the best with 29% cell viability compared to 9% for $1x10^5$ cells/array and 100% for $1x10^4$ cells/array (**Figure 2.3**). Together these results indicate that microraft arrays when plated with approximately 1 million cells produce healthier cultures than traditional multiwell plates used in screening.

2.3.2 hESC-Derived Neuron Cell Culture

Following the successful culturing of rat neurons, human embryonic stem cell (hESC) – derived neurons were tested on the microrafts. For these experiments the H9 ESC line was used and were differentiated as described in the Methods section.

After optimizing the microraft array sterilization method, plating density, and the frequency of media changes, 500 K neuro-progenitor cells were plated on poly-L-ornithine with laminin coated Cellrafft arrays. The microrafts were released after 1 DIV and transferred to a 12-well plate for further growth. In a previous experiment hESC-derived neurons did not survive past ten days, so after 8 DIV the cells were fixed and stained. The cells were observed daily and appeared healthy before and after transfer to the 12-well plate showing extended processes uniform dispersion (**Figure 2.4C and D**). Using DRAQ5 nuclear dye, and SYTOX green to label the dead cells (**Figure 2.4A and B**), a viability assay was performed showing 47% cell viability which was consistent with the rodent neurons (**Figure 2.4E**).

2.4 Conclusions

Neurons are considered more delicate than most cell types. Neurons cannot grow in single cell isolation because their growth depends on network communication, thus a certain cell density is required for healthy neuron cultures. This study concluded that neuron cultures on microrafts were somewhat superior to traditional well plates in terms of viability and final cell density. In regards to viability, the three probable reasons why the microrafts outperform traditional multiwell plates is related to nutrient concentration in the media, change in pH, and oxygen exchange.

The cell rafts support on average 300 cells whereas 384-well plates and 1536-well plates require between 5-20,000 cells per well and 1 – 10,000 cells per well respectively. When taking the ratio of these cell densities to the volume of the wells, there is large proportion of nutrients per cell for the Cell rafts. Thus, the significant increase in throughput for the same volume of media leads to cells with an adequate amount of nutritional resources.

Another reason for improved cell culture with the microrafts is the change in pH. Since the culture medium controls the pH of the culture and buffers the cells from changes in pH, as the media is consumed by the cells and as it evaporates, this pH change causes cell death. Since the surface area of each well of 384-well plates is larger than 1536-well plates, the evaporation rate is larger, however since the volume of each well in 1536-well plates are approximately $^{1}/_{2}$ to $^{1}/_{12}$ that of 384-well plates, the changes in pH are much more significant. Therefore we find that viability is worse in the 1536-well plates than the 384-well plates, and 384-well plates containing microrafts perform even better because they consume less media, keeping the pH stable.

The last reason for higher viability is associated with oxygen exchange. This phenomenon is also associated with the surface to volume ratio since vessels with small depths and large surface areas have high rates of oxygen diffusion. In terms of surface to depth ratio the 1536-well plates have a factor of 0.578 versus 1.55 for 384-well plates. Therefore, the 1536-well plates have reduced oxygen exchange leading to lower cell viability. Since microrafts have an approximate height of 150

µm, cells cultured on these particles are closer to the surface when placed in 384-well plates leading to better viability than culturing directly in the 384-well plates.

In addition to viability, a higher final cell density for Neurons plated on microrafts was observed compared to 384 and 1536-well plates. Final cell density is important to understanding how well neurons are attaching to the surface. It was observed that neurons plated on microrafts had a final plating density closest to the initial density. Therefore it can be concluded from these results that not only are neurons adhering well to the microrafts, but they also remain adherent during the process of release and transfer to 384-well plates which was seen nicely in the hESC-derived cultures. For neurons plated directly into 384-well or 1536-well plates, it's postulated that these cells more often either adhere to the sides of the well, or do not adhere at all.

2.5 Tables & Figures

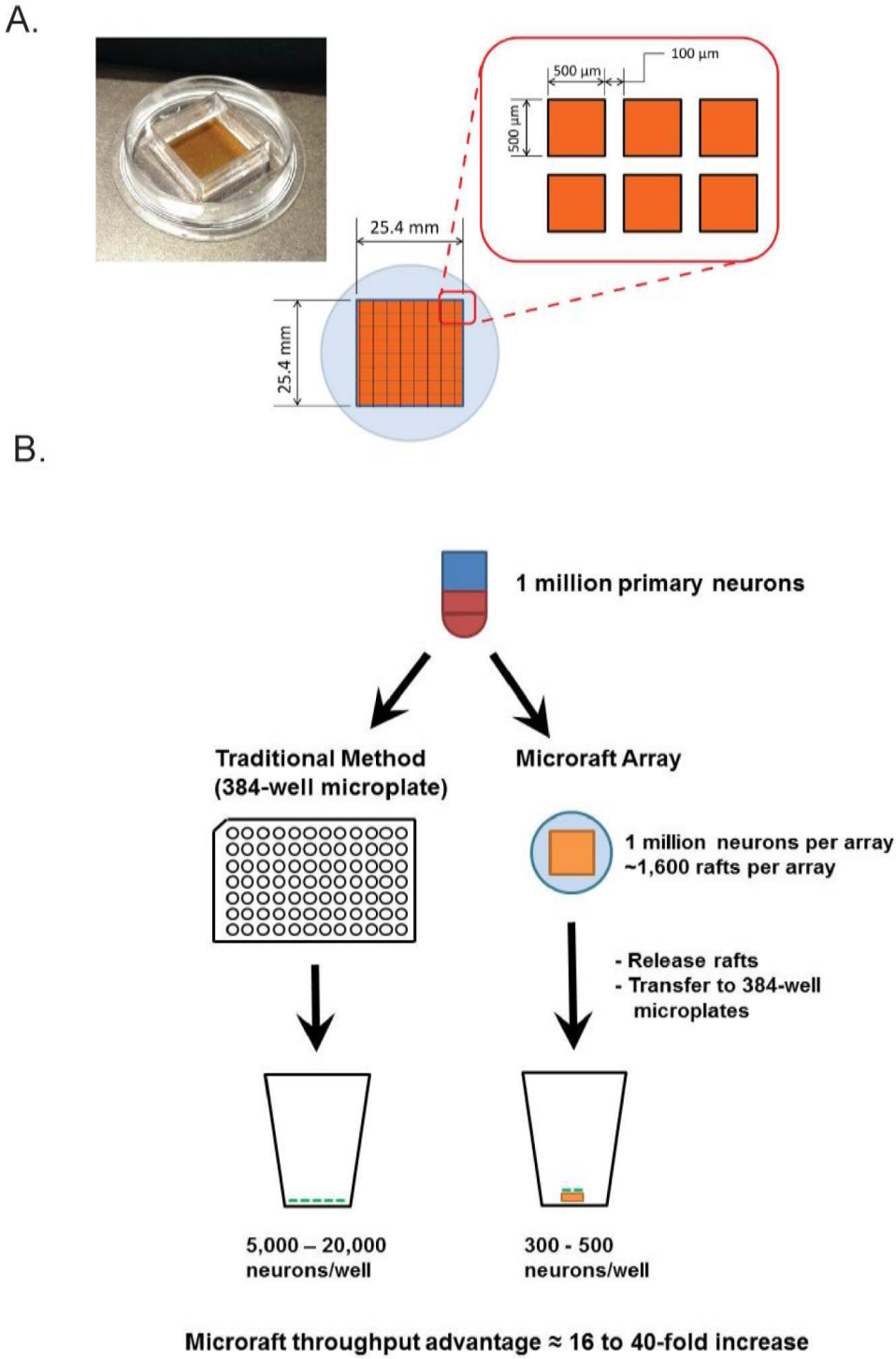

Figure 2.1. Microraft array design schematics (A) Image and design details of microraft array. (B) Throughput potential of microraft array

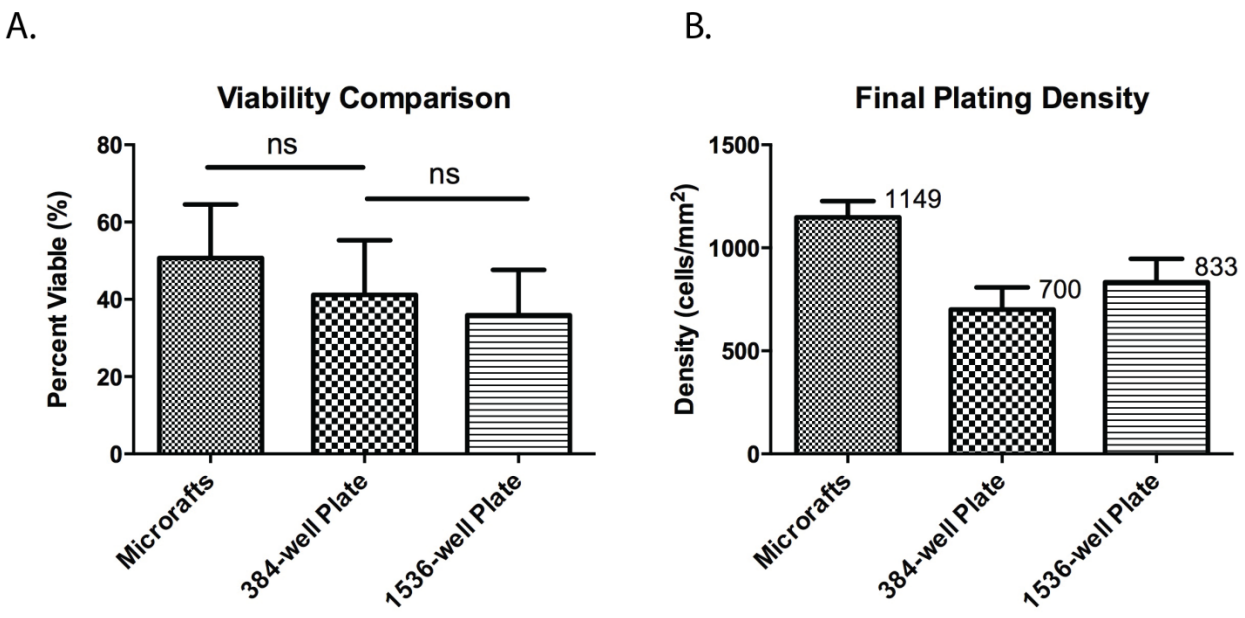

Figure 2.2. Cell culture performance of microrafts with rat neurons (A) Cell viability versus culture plate type. (B) Final plating density versus culture plate type.

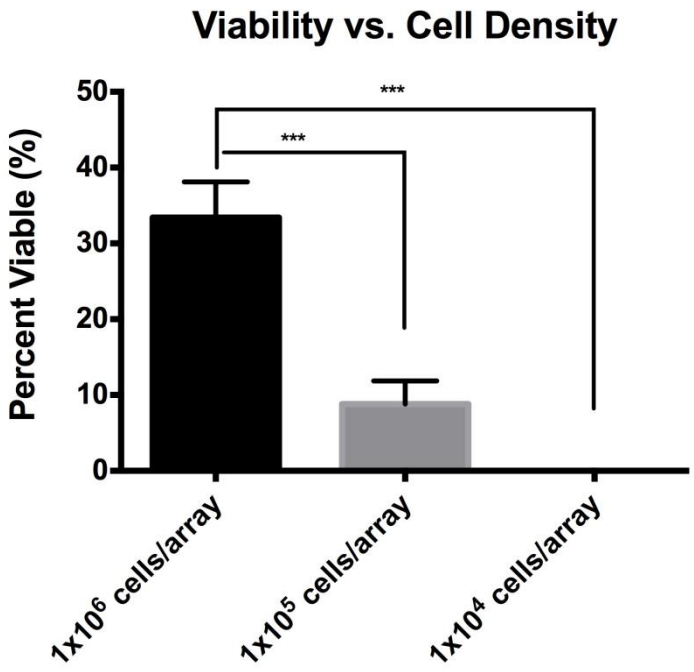

Figure 2.3. Neuronal cell viability versus cell density using microrafts

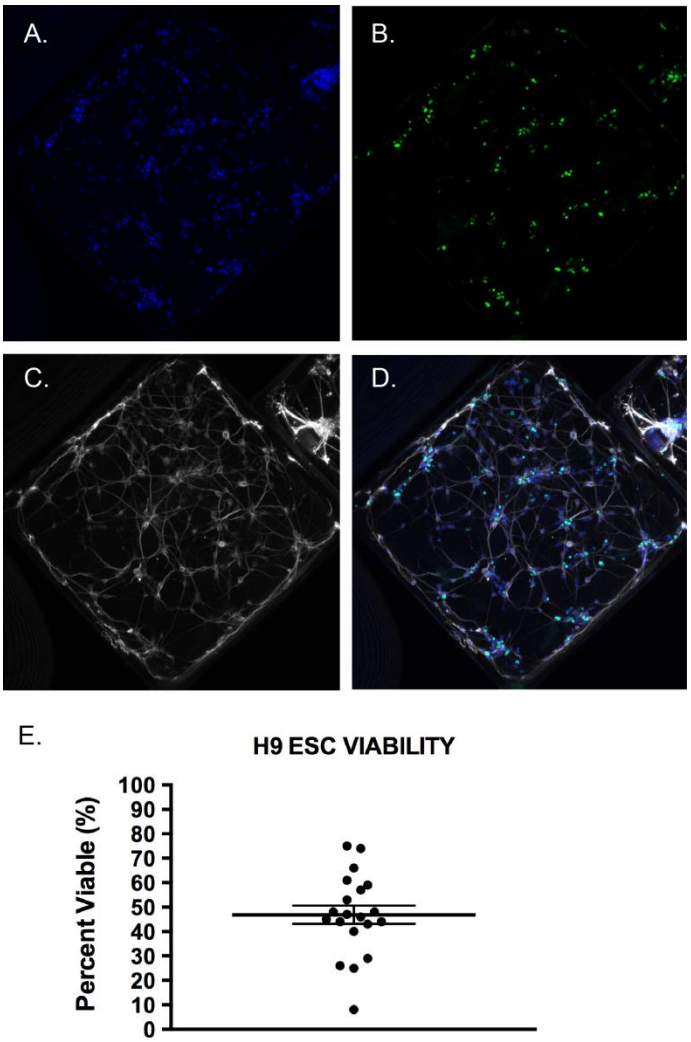

Figure 2.4. Human ESC-derived neurons grown on microrafts. (A) DRAQ 5 nuclear marker. (B) SYTOX Green dead cell marker. (C) MAP2 microtubule neuronal dendritic marker. (D) Merged channels. (E) Mean cell viability.

2.6 BIBLIOGRAPHY

1. Thorne N, Malik N, Shah S, Zhao J, Class B, Aguisanda F, Southall N, Xia MH, McKew JC, Rao M et al. 2016. High-throughput phenotypic screening of human astrocytes to identify compounds that protect against oxidative stress. Stem Cells Translational Medicine. 5(5):613-627.

2. Dai S, Li R, Long Y, Titus S, Zhao JH, Huang RL, Xia MH, Zheng W. 2016. One-step seeding of neural stem cells with vitronectin-supplemented medium for high-throughput screening assays. Journal of Biomolecular Screening. 21(10):1112-1124.

3. Fuller JA, Shaw GC, Bonnet-Wersinger D, Hansen BS, Berlinicke CA, Inglese J, Zack DJ. 2014. A high content screening approach to identify molecules neuroprotective for photoreceptor cells. Retinal Degenerative Diseases: Mechanisms and Experimental Therapy. 801:773-781.

4. Wang YL, Phillips CN, Herrera GS, Sims CE, Yeh JJ, Allbritton NL. 2013. Array of biodegradable microrafts for isolation and implantation of living, adherent cells. Rsc Advances. 3(24):9264-9272.

5. Attayek PJ, Hunsucker SA, Sims CE, Allbritton NL, Armistead PM. 2016. Identification and isolation of antigen-specific cytotoxic t lymphocytes with an automated microraft sorting system. Integrative Biology. 8(12):1208-1220.

6. Attayek PJ, Hunsucker SA, Wang YL, Sims CE, Armistead PM, Allbritton NL. 2015. Array-based platform to select, release, and capture epstein-barr virus-infected cells based on intercellular adhesion. Analytical Chemistry. 87(24):12281-12289.

7. Wang YL, Salazar GT, Pai JH, Shadpour H, Sims CE, Allbritton NL. 2008. Micropallet arrays with poly(ethylene glycol) walls. Lab on a Chip. 8(5):734-740.

8. Wang YL, Phillips C, Xu W, Pai JH, Dhopeshwarkar R, Sims CE, Allbritton N. 2010. Micromolded arrays for separation of adherent cells. Lab on a Chip. 10(21):2917-2924.

9. Niedringhaus M, Dumitru R, Mabb AM, Wang Y, Philpot BD, Allbritton NL, Taylor AM. 2015. Transferable neuronal mini-cultures to accelerate screening in primary and induced pluripotent stem cell-derived neurons. Sci rep. England. p. 8353.

10. Gach PC, Wang Y, Phillips C, Sims CE, Allbritton NL. 2011. Isolation and manipulation of living adherent cells by micromolded magnetic rafts. Biomicrofluidics. 5(3):32002-3200212.

11. Taylor AM, Wu J, Tai HC, Schuman EM. 2013. Axonal translation of beta-catenin regulates synaptic vesicle dynamics. J Neurosci. 33(13):5584-5589.

12. Niedringhaus M, Dumitru R, Mabb AM, Wang Y, Philpot BD, Allbritton NL, Taylor AM. 2015. Transferable neuronal mini-cultures to accelerate screening in primary and induced pluripotent stem cell-derived neurons. Sci Rep. 5:8353.

13. Hallfors N, Khan A, Dickey MD, Taylor AM. 2013. Integration of pre-aligned liquid metal electrodes for neural stimulation within a user-friendly microfluidic platform. Lab on a Chip. 13(4):522-526.

Chapter 3: Transfer of Microrafts

3.1 Introduction

Transport and manipulation on the cellular-scale is very important for biological research. Cell separation, sorting, and single cell analysis have been of interest to biologist for decades, and achieving these tasks requires manipulation on the micron-scale. Currently optical and acoustic techniques represent the most widely used methods for such manipulations.

Historically, the first of these two techniques to be implemented was the optical approach, or better known as “optical tweezers”. This technique was first demonstrated by Ashkin et al. in 1986. In this work, he demonstrated the trapping of microparticals using a single tightly focused laser beam.[1; 2] Even before using a single beam, Ashkin’s group demonstrated dual beam trapping, levitation of particles against gravity in both vacuum and air, and the movement of particles through liquid.[3; 4] These techniques are still widely used today with little modification.

In more recent years, there have been new developments in acoustic methods. In 2010 Courtney et al. demonstrated a method of trapping and manipulating micron-scaled particles in liquid using ultra-sound. In this method, spatially controlled standing waves are created with opposing piezoelectric transducers at either end of a liquid filled cavity. Using the transducers to control the phase difference between the counter-propagating traveling waves, 5 µm-radius

polystyrene spheres were trapped and moved in one direction at 0.14 mm increments.[5]

For the manipulation of particles in two directions, in 2012 Ding et al. developed a method to use acoustic standing surface waves to move and manipulate microparticles, cells, and microorganisms. With a single layer microfluidic chip featuring four opposing chirped interdigital transducers in a square layout, 10 µm-sized polystyrene beads were transported in an arbitrary path in two dimensions. Additional, demonstrating its biocompatibility Hela cells and C. elegans were maneuvered, and no significant damage was found in cell viability or proliferation.[6]

All of these methods, although very powerful, only transport particles on a single platform. In this work, the concept of transferring particles between platforms is addressed. Here methods were tested including standard fluidic pipetting as well as a novel magnetic wand to transfer microrafts from their original array to a 384-well plate. The primary objective in this study was to create a solution for transferring microrafts in a manual fashion to avoid the costly fluid handling infrastructure of commercial drug discovery laboratories.

3.2 Materials and Methods

3.2.1 Design and Analysis

3D solid modeling of the magnetic wand was created using SolidWorks 2012 (Dassault Systems). Detailed drawings of the magnetic wand were created in AutoCAD 2012 – Student Version (Autodesk). Finite element analysis was

performed using COMSOL Multiphysics version 4.3 (COMSOL Inc.). All finite element models were created axial symmetrically with a relative permeability of neodymium of 1.05 and a remenent flux density of 1.48T which is characteristic of a 52 MGOe neodymium magnet. A “physics controlled” extra fine mesh was used in all models.

3.2.2 Magnetic Wand Materials

For the design and testing of the magnetic wand 1/8” x 3/8” neodymium cylinder magnets grades N42 and N52 (D24 and D24-N52, K&J Magnetics, Inc.) were used as well as 1/8” x 1/4” neodymium cylinder magnets grades N42 and N52 (D26 and D26-N52, K&J Magnetics, Inc.). For the probe and magnet shielding material Hy Mu 80 (ASTM A-753 Alloy 4) (Scientific Alloys Inc.) was used. The probe used to attract the microrafts which was housed inside of the shield was fabricated from annealed “soft” iron.

3.2.3 Fabrication of Magnetic Wand

The magnetic wand probe and shield were fabricated with traditional machining techniques.

3.2.4 Microraft Array Fabrication

Microraft arrays were fabricated according to previously published methods[7; 8]. Briefly, soft lithography was used to make the poly(dimethylsiloxane) (PDMS) template containing an array of microwells (each well has width x length x height = 500 µm x 500 µm x 200 µm, array size = 25.4 mm x 25.4 mm). The PDMS template was then dip coated with a 20% polystyrene solution in gamma-butyrolactone (GBL)

containing 4% iron oxide particles. The arrays are then placed in a convection oven at 95°C for 16 hours to evaporate GBL to create the microrafts. The array was glued to a polystyrene cassette to facilitate handling, and then surface treated with air plasma (Harrick Plasma) for 2 min.

3.2.5 Fluid Handling Materials

Transfer of microrafts to 96-well plates was tested using a Thermo Scientific Multidrop Combi with the standard tube dispensing cassette (Cat # 24072670). The microrafts were suspended in PBS with 0.1% Triton X and the droplet size was specified at 50 µL.

Transfer of microrafts to 384-well plates was tested using a standard sixteen channel pipette manufactured by Eppendorf.

3.3 Results and Discussion

3.3.1 Design and Fabrication of Magnetic Wand

There are two main approaches to picking up and transferring microrafts to multiwell plates– magnetic and fluidic. The objective of the magnetic approach is to exploit the magnetic characteristics of the microrafts, picking up individual ones amongst a pool. In order to achieve this, the magnet must be shielded such that it only attracts a single raft. One of the major challenges with this approach is locating a magnet on the scale of the microraft which is 0.25 mm^2. There are Neodymium magnets you can purchase with diameters as small as 0.3 mm, however these magnets are very brittle and don't produce fields strong enough to hold single rafts throughout the transfer process. The ideal situation calls for a magnet that is big

enough and strong enough to attract and hold a single raft, but not so large that it attracts multiple rafts within the pool.

To achieve this goal, the technique of channeling the magnetic field through a ferromagnetic material such as iron can be used to focus and direct the magnetic field to a small point thus attracting a single microraft at the tip. This technique however still requires shielding of the magnet and probe to block the magnetic field from attracting additional microrafts to the sides. This technique also requires attaching and separating the magnet from the channeling probe to attach and then release the microraft. With these specifications in mind, a magnetic wand was designed based off of a standard push-button ball point pen (**Figure 3.1A**). Tooling files were created in SolidWorks for 3D printing of all the components except for the magnet, shield, and probe (**Figure 3.1B-D**).

The microraft must release from the probe tip when the magnet is separated from the probe, so the most desirable material for the probe is one with a low magnetic remanence. Soft (annealed) iron, which is commonly used in electric motor cores, was used for these purposes because it has a narrow magnetic hysteresis loop with a coercivity (H_c) on the order of 80 A/m. For the shielding, a material was needed that would block microrafts from being attracted to both the magnet and sides of the probe. Since magnetic fields can only be channeled and not blocked, the material chosen would have to have a high magnetic permeability in order to achieve this goal. Hy Mu 80 (ASTM A-753 Alloy 4) was chosen because it has a maximum relative permeability (μ_r) of 200,000.

After completing the design, the primary components for the magnetic wand including the probe and shield were fabricated. These parts were fabricated using standard machining techniques. The decision was made to forgo fabrication of the other components of the wand until the testing was concluded on the primary components.

3.3.2 Analysis of the Magnetic Wand

Finite element analysis was used throughout the design process to shape and define certain components as well as model their behavior. The probe was modeled first in order to ascertain the appropriate length. The objective in designing this component was to create a probe tip (probe + shielding) narrow enough to fit inside an individual well of a 384-well plate (Ø≈3.3 mm) to release the microraft, but long enough to maximize handling and decrease the transfer time. The probe was modeled and analyzed in three different lengths, 1 cm, 1.5 cm, and 2 cm – all with a 1 mm diameter. The results of this analysis showed that the peak magnetic field strength decreases as the probe length increases (**Figure 3.2**). Although a 2 cm probe would still be strong enough to attract a microraft, the 1.5 cm probe was chosen because a 2 cm probe would be almost impossible to machine with a 1 mm diameter.

After finalizing the length of the probe, it was necessary to determine the proper angle in which the tip narrowed to its desired point (**Figure 3.3**). The tip was designed to taper from a diameter of 1 mm to 0.25 mm. The final diameter of 0.25 mm was chosen because each microraft has a width of 0.5 mm and this will reduce the chance of attracting multiple microrafts. The angle with which the tip tapers is

important however because the magnetic field emanates from the surface of the probe at 90 degree angles, thus in order to block the field effectively with the shielding the objective is to maximize the amount of field that id blocked by the shield. Modeling various taper lengths revealed that longer lengths (more acute angles) provided higher magnetic field strengths along the axis of the probe and were more effective at blocking unwanted fields emitting perpendicular to the probe face (**Figure 3.3**).

With the length of the probe and taper angle of the tip, it was also necessary to determine the minimum separation distance between the probe and the magnet necessary to release the microraft. When separated, magnetic forces still transmit through the probe, thus a model was created to analyze the distance required for this force to reduce to a level insufficient to hold the microraft. This distance was then incorporated into the design as the magnet retraction and intersection operates with a push-button spring mechanism. After analyzing separation distances from 0 mm to 12 mm, it was determined that at 10 mm or more, the field strength along the axis of the probe was 0.0044 T (**Figure 3.4A-B**) which is two orders of magnitude less than a common bar magnet and nearly as low as the Earth's magnetic field which used as a near zero benchmark.

3.3.3 Testing of the Magnetic Wand

After completing the analysis and design, the probe and shield were fabricated for empirical testing. Using an Olympus MVX10 macro-view microscope, the probe dimensions were validated following fabrication. Three probes were fabricated and all were well within the range of the design specifications (**Figure**

3.5A-B). The wand and shield were then adjoined using epoxy and the tip was polished flat (**Figure 3.6A-B**).

In order to test the magnetic wand, a variety of magnets and magnet combinations were used. In this test, the fabricated components were handled in the same fashion as the proposed wand, i.e. the probe-shield combination was placed into a microraft array with a pool of released microrafts, a microraft was retrieved from the pool and transported over to a 384-well plate where it was released by separating the magnet from the probe. Four different magnets were used, D24, D24-N52, D26, and D26-N52 (K&J Magnetics). Initially these magnets were tested each by themselves, but none of them were effective at attracting the microrafts, so combinations of two and three magnets were used. Of the two magnet combinations, the D24+D24 and the D26-N52+D24 combinations transferred 1 microraft on average however the D24+D24 combination had more non-zero (transferring at least one microraft) transfers than the D26-N52+D24 combination making it slightly more efficient (**Figure 3.7A-B**). For the three magnet combinations the combination with the highest amount of non-zero transfers while also averaging 1 microraft was the D26+D26-N52+D26-N52 (**Figure 3.8A-B**).

3.3.4 Fluidic Approach

After testing the magnetic approach to transferring the microrafts two fluid based approaches were tested – using an established fluid handling machine and a multichannel pipette. The fluid handling machine used was a Thermo Scientific Multidrop Combi Reagent Dispensor. This instrument withdraws fluids from a single source and dispenses it into multiwell plates for high throughput plate preparation

and replication. The Multidrop Combi is combatable to multiwell plates with 6 to 1536 wells and has a dispense range from 0.5 to 2500 µL. In testing this device the standard tube dispensing cassette was used which has an inner diameter of 0.5 mm. This is the same size as the microrafts, but this is the largest cassette available, so the test was carried out anyway. In this experiment, a 50 µL setting was used to dispense a sample consisting of 64 rafts/mL into a 96 well plate. During this process, microrafts were sucked out of the sample holder (50 mL Falcon tube) and through the dispensing cassette tubes, but the Cell rafts clogged at the tips of the cassette head. Furthermore, in observing the cassette tubes, there were clumps of variable sizes and at variable frequencies throughout the tubes. At the tips, the clumps ranged in sizes with some tips fully clogged, but others completely empty.

With the failure of the Multidrop Combi Reagent Dispensor, attention was turned toward a traditional multichannel pipette. In using this tool, microrafts are first released from their array, transferred to a pipette trough using a single channel 1 mL pipette, and then transferred to a 384-well plate with a 16-channel pipette. In testing this method a range of volumes were used from 50 µL to 5 µL and the number of microrafts were counted per channel for each of the sixteen channels. Of these volumes, 30 µL and 10 µL dispenses showed the least variability among channels (**Figure 3.9**) however 30 µL dispenses was seen as most optimal because for the same number of occurrences of single raft transfers, 21% on average, the 30 µL dispense had a lower number of empty wells than the 10 µL dispense at 27% compared to 35% respectively (**Figure 3.10**).

3.4 Conclusions

There are few methods for physically transporting individual micron-size particles. Here two methods were presented including magnetic and fluidic. In the magnetic approaches a magnetic wand was successfully designed, analyzed, and fabricated to specifications. Finite element analysis illustrated that a magnetic field could be channeled through a ferromagnetic material and the numerical trends associated with these fields when dimensional changes are made to the form of these materials. Additionally, analysis also illustrated that the magnetic field could be focused in a single direction through the use of blocking materials which filter unwanted field lines. These principles and phenomena were demonstrated through empirical testing of the fabricated probe and shield. It was clear from these tests that it was possible to attract and transfer fewer than four microrafts and in some cases single microrafts although not as frequently as hoped and planned. One of the main reasons for the poor performance of this device was presence of adherent forces created by fluid capillary action, i.e. the microraft remains adhered to the wand after the magnet is separated due to fluid tensile forces. Unfortunately this phenomenon could not be adequately accounted for during the analysis phase of the design and was thus unanticipated.

In turning to the fluidic approaches for transferring the microrafts, it was clear after testing that the Thermo Scientific Multidrop Combi was not going to work. Even if the manufacturer produced a head with tips large enough for the microrafts to pass through, there was too much variability among the channels – with some tips

containing as many as ten microrafts clogged in it. Furthermore, the along each tube were clumps of microrafts of varying sizes at various spaces.

The concept of using a multichannel pipette to transfer the microrafts was a natural one. This is a well-established tool in biology and has already been used extensively for micro-sized particles such as microbeads. Furthermore it is manually operated and doesn't require expensive automated machines. Although this tool is variable among separate channels, this was expected, and in the use of this tool to transfer microrafts it was found to be effective overall. In all instances, the pipette transferred on average less than five microrafts which is adequate in demonstrating the advantages in throughput this technology promises. Taken together, this data illustrates that microrafts can be transported and manipulated manually by both magnetic and fluidic means with the best results achieved with the use of a multichannel pipette and low dispensing volumes.

3.5 Tables & Figures

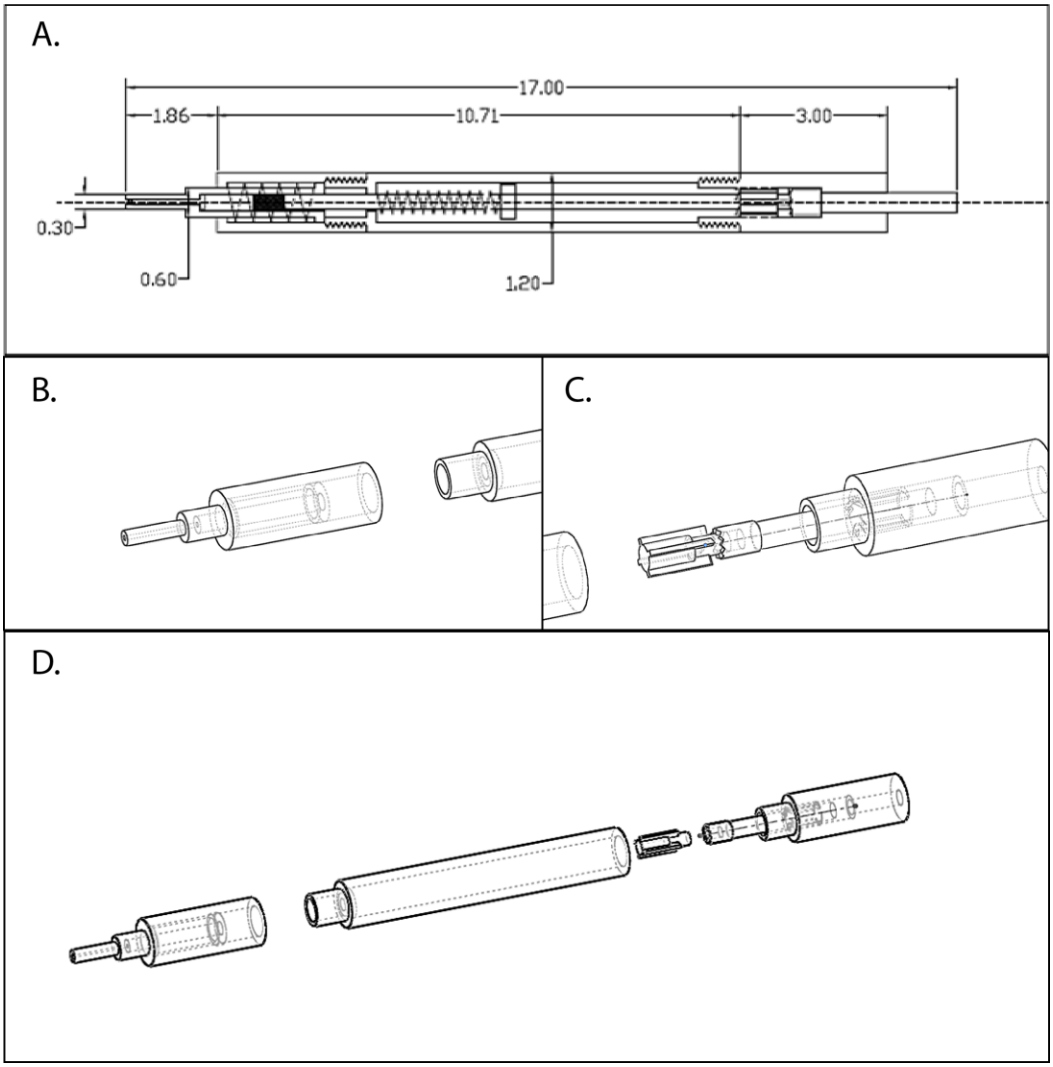

Figure 3.1. Magnetic wand detailed drawings and 3D assembly. (A) Detailed cross-sectional profile (B) Probe and magnetic shield assembly. (C) Rear mechanical assembly for magnet engagement and disengagement. (D) Full 3D part assembly. Units are in centimeters.

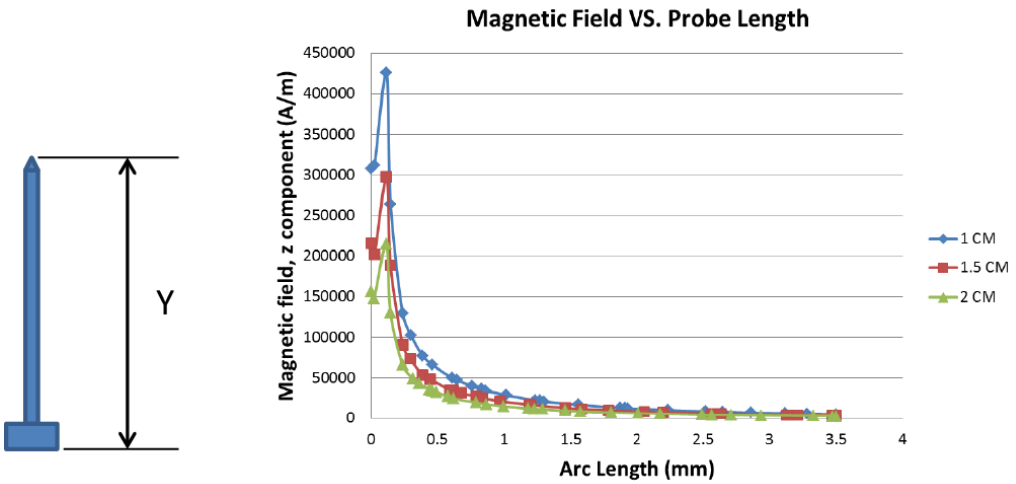

Figure 3.2. Finite element analysis of probe length. Magnetic field (ampere/meter) is measured at the probe tip, and the arc length is measured perpendicular from the probe centerline.

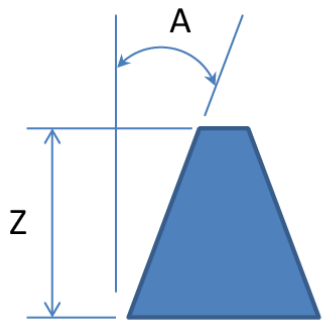

Z (mm)	A (deg)
0.5	37
0.75	27
1.0	21
1.25	17

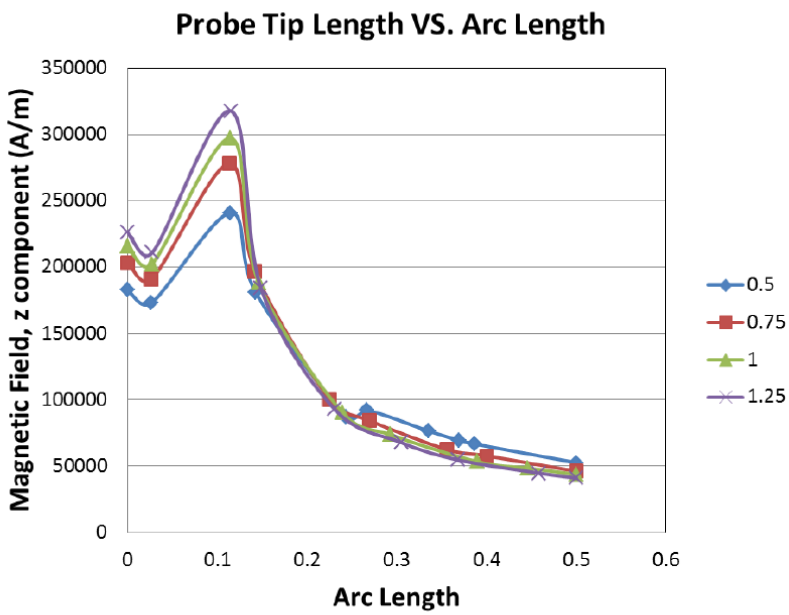

Figure 3.3. Finite element analysis of the probe tip. Magnetic field (ampere/meter) is measured at the probe tip, and the arc length is measured perpendicular from the probe centerline.

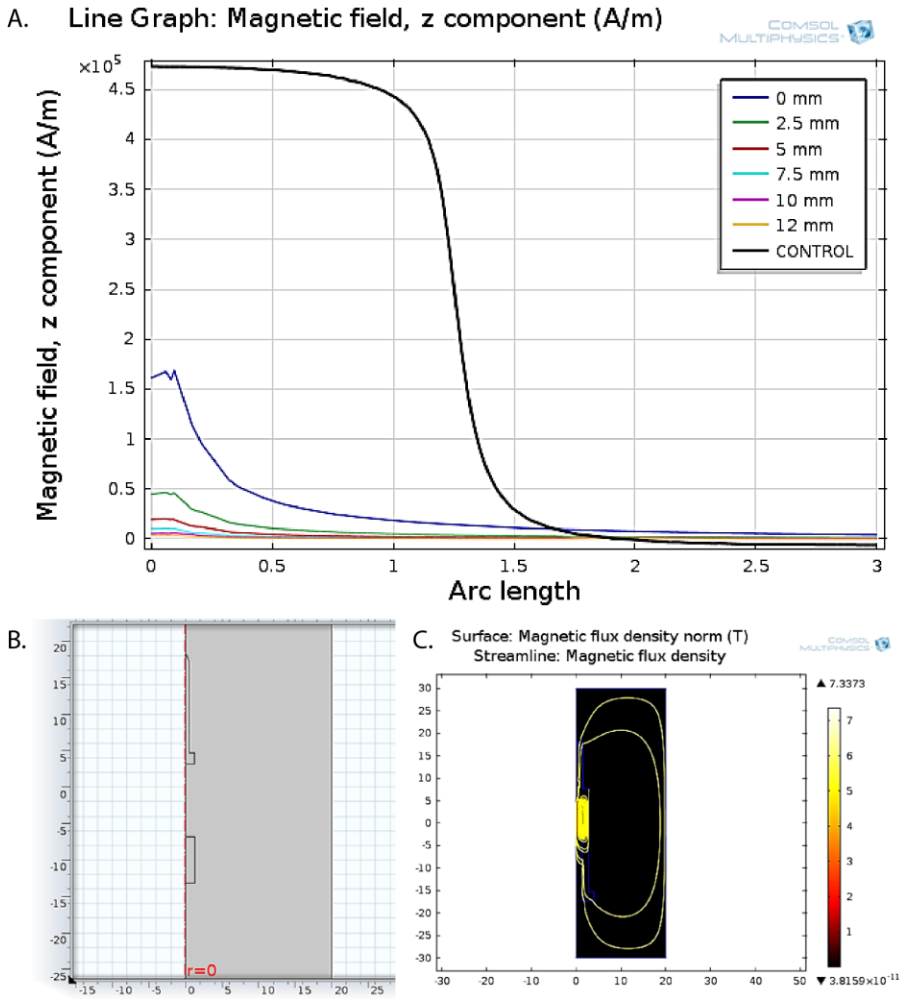

Figure 3.4. Finite element analysis of magnet probe-probe interaction. (A) Magnetic field (ampere/meter) from probe tip measured at multiple separation distances. (B) Computational model layout. (C) Model of probe with magnetic shielding. Magnetic field lines are in yellow.

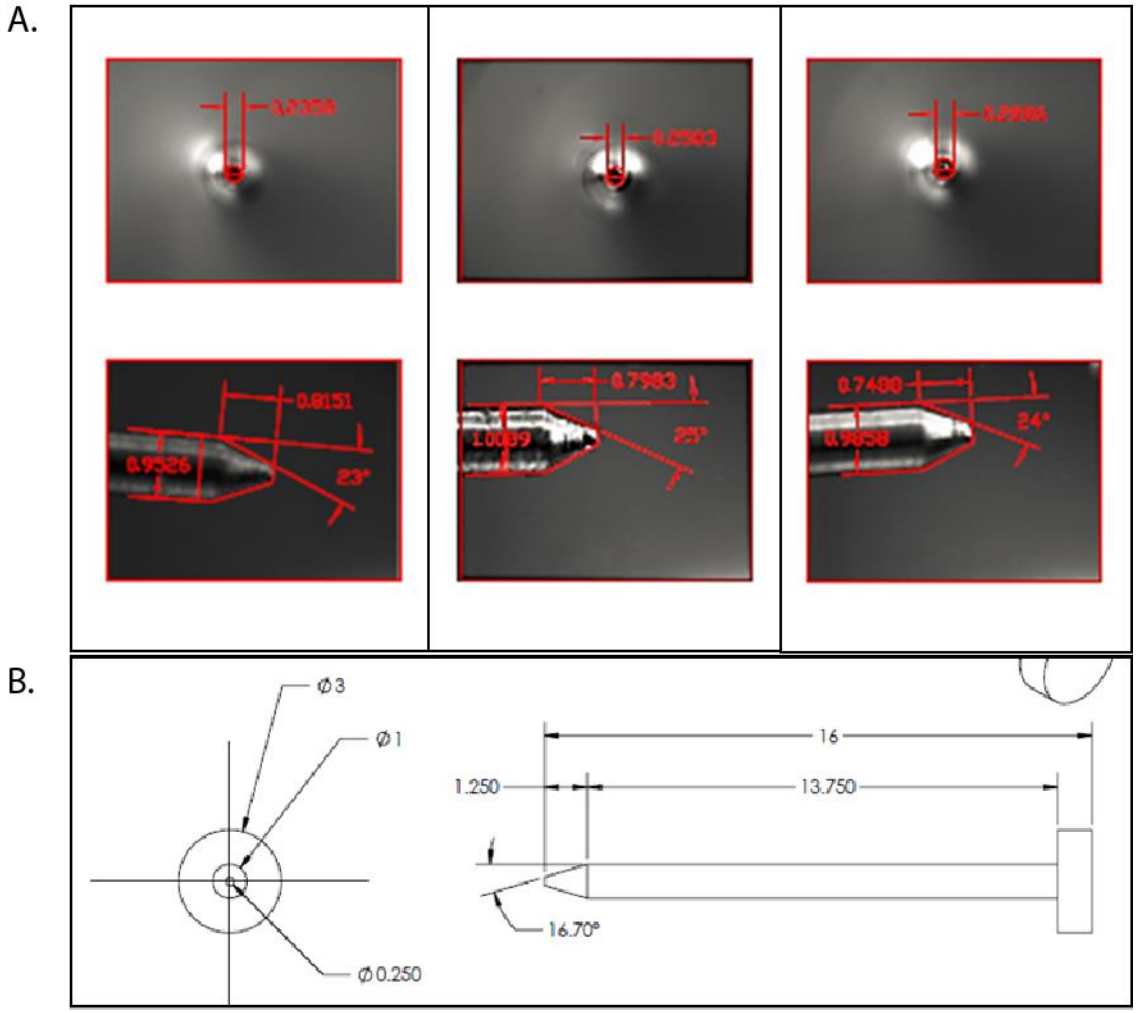

Figure 3.5. Fabricated probe tip verification. (A) Comparison of three separate probes for accuracy. (B) Detailed drawing of probe with specified dimensions. Units are in millimeters.

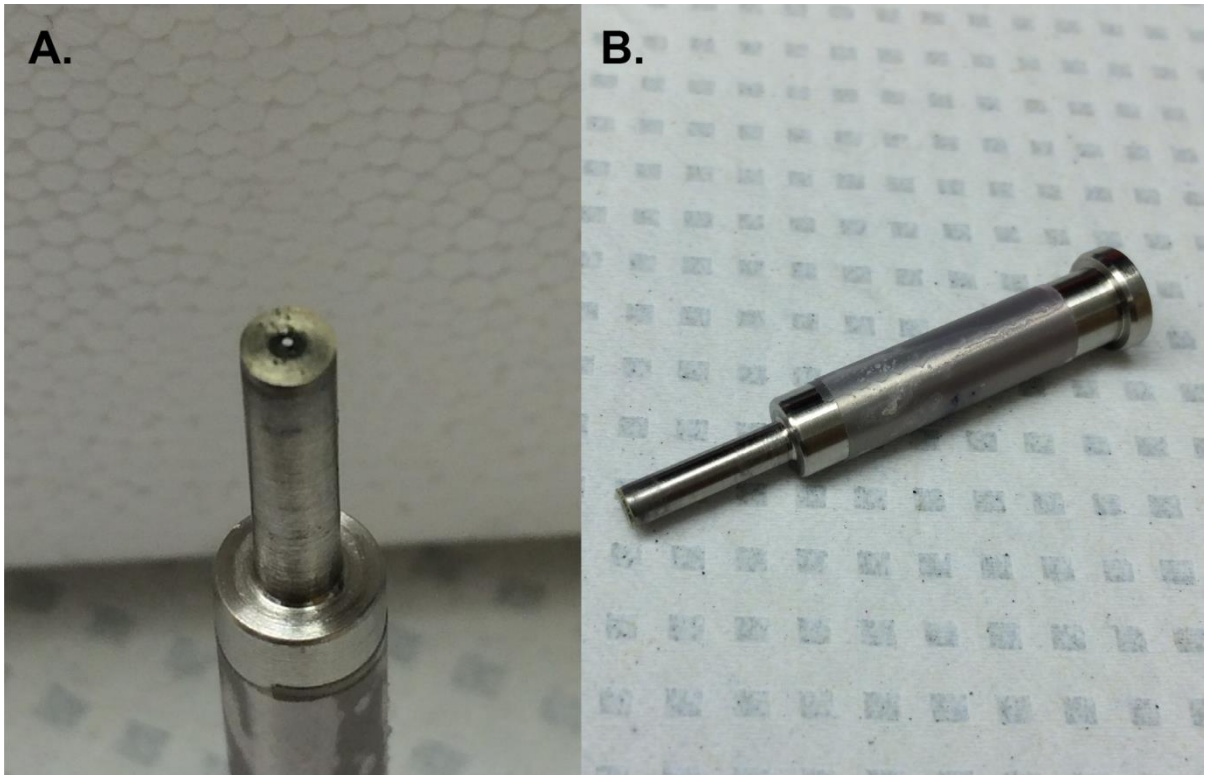

Figure 3.6. Magnetic probe encased with Hy-Mu80 magnetic shield. (A) Focused image shows tip of probe at center of magnetic shield. (B) Profile of probe-shield assembly.

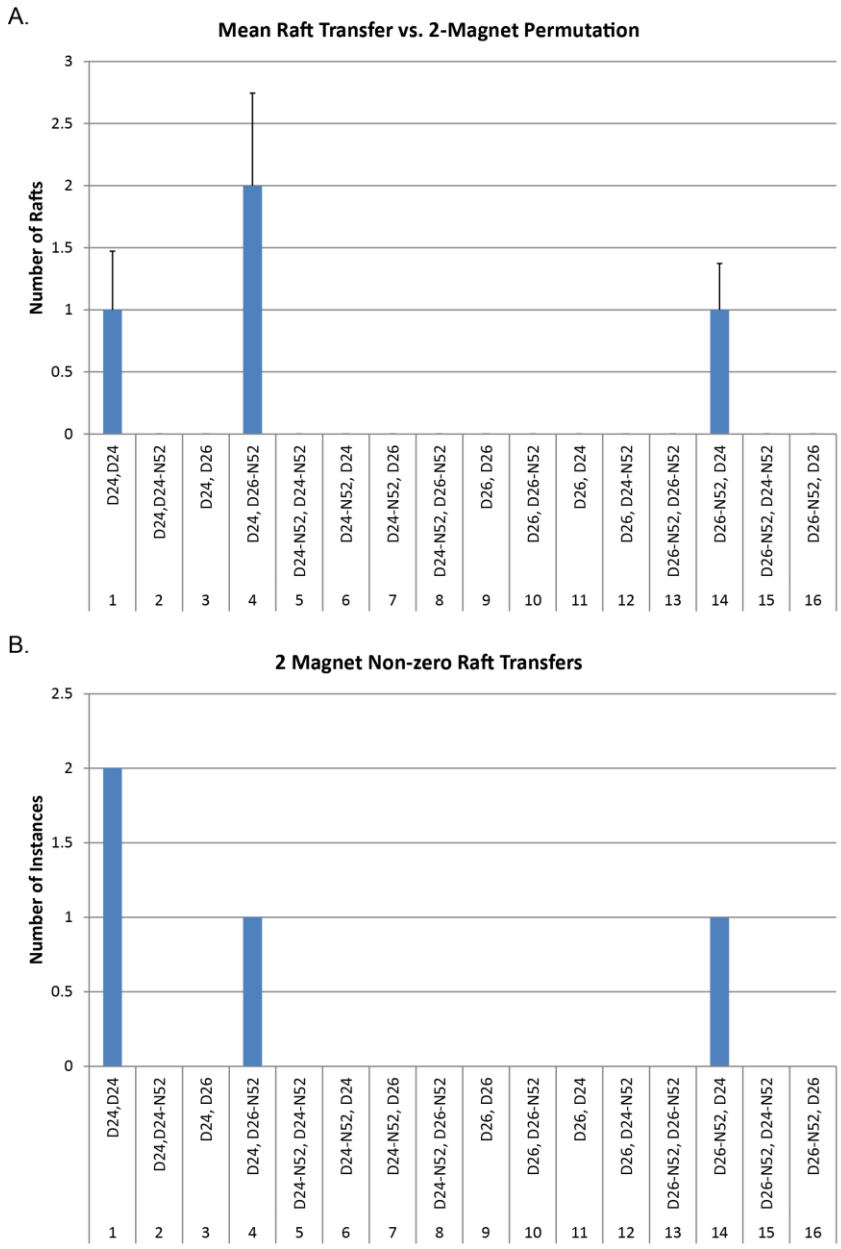

Figure 3.7. Magnetic wand performance testing with 2-magnet combinations. (A) Mean (rounded to whole number) number of microrafts lifted and transferred to a 384-well plate for each magnet permutation. (B) The number of times a microraft was transferred out of six attempts.

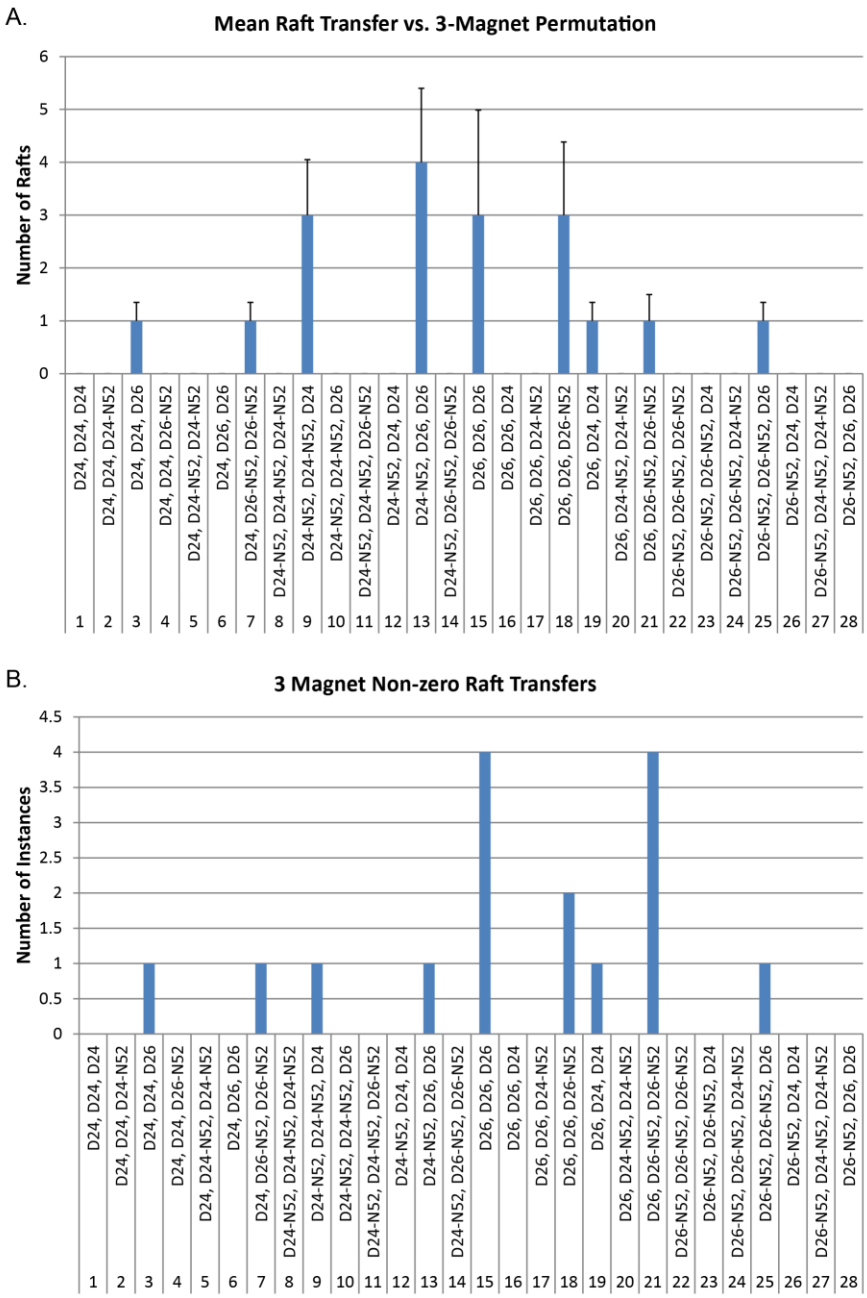

Figure 3.8. Magnetic wand performance testing with 3-magnet combinations. (A) Mean (rounded to whole number) number of microrafts lifted and transferred to a 384-well plate for each magnet permutation. (B) The number of times a microraft was transferred out of six attempts.

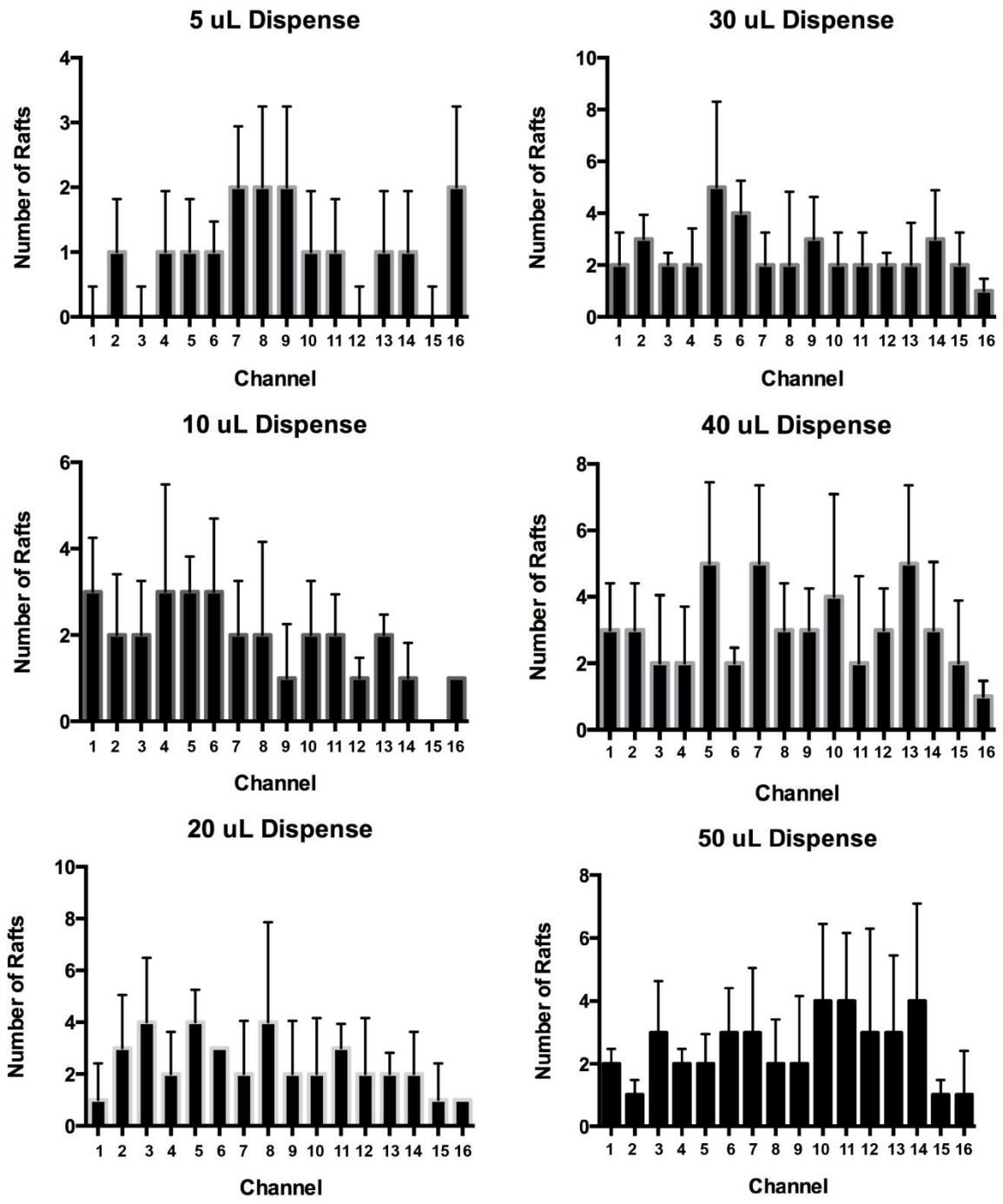

Figure 3.9. Microraft transfer performance with a sixteen-channel pipette at various draw/dispense volumes.

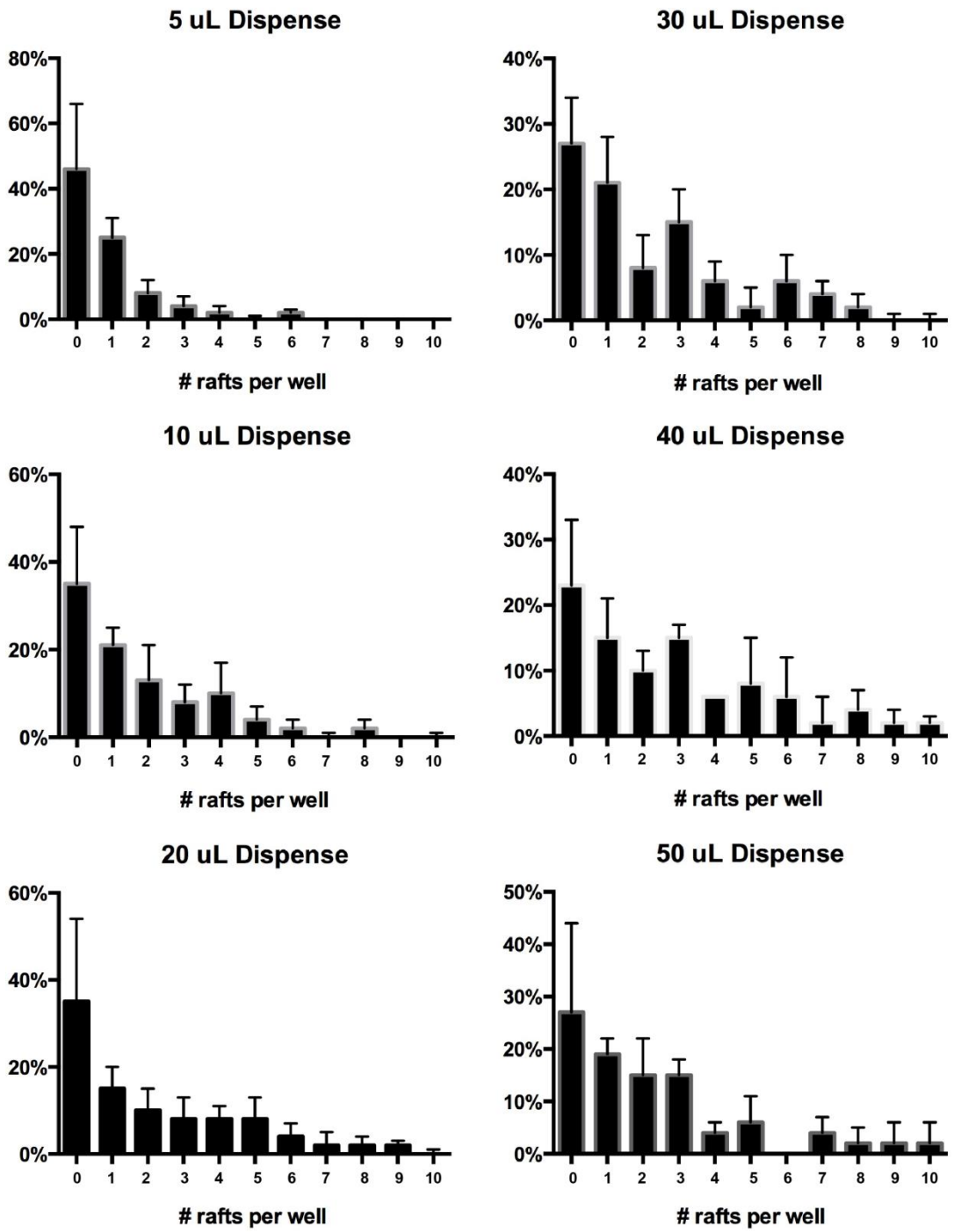

Figure 3.10. Success rate for each number of microrafts transferred using a sixteen-channel pipette at various draw/dispense volumes.

3.6 BIBLIOGRAPHY

1. Ashkin A, Bjorkholm JE, Chu S. 1986. Caught in a trap. Nature. 323(6089):585-585.

2. Ashkin A, Dziedzic JM, Bjorkholm JE, Chu S. 1986. Observation of a single-beam gradient force optical trap for dielectric particles. Optics Letters. 11(5):288-290.

3. Ashkin A. 1970. Acceleration and trapping of particles by radiation pressure. Physical Review Letters. 24(4):156-&.

4. Ashkin A, Dziedzic JM. 1971. Optical levitation by radiation pressure. Applied Physics Letters. 19(8):283-&.

5. Courtney CRP, Ong CK, Drinkwater BW, Wilcox PD, Demore C, Cochran S, Glynne-Jones P, Hill M. 2010. Manipulation of microparticles using phase-controllable ultrasonic standing waves. Journal of the Acoustical Society of America. 128(4):E195-E199.

6. Ding XY, Lin SCS, Kiraly B, Yue HJ, Li SX, Chiang IK, Shi JJ, Benkovic SJ, Huang TJ. 2012. On-chip manipulation of single microparticles, cells, and organisms using surface acoustic waves. Proceedings of the National Academy of Sciences of the United States of America. 109(28):11105-11109.

7. Gach PC, Wang Y, Phillips C, Sims CE, Allbritton NL. 2011. Isolation and manipulation of living adherent cells by micromolded magnetic rafts. Biomicrofluidics. 5(3):32002-3200212.

8. Wang YL, Phillips C, Xu W, Pai JH, Dhopeshwarkar R, Sims CE, Allbritton N. 2010. Micromolded arrays for separation of adherent cells. Lab on a Chip. 10(21):2917-2924.

[1]Chapter 4: Magnetic Centering of Microraft in 384-Well Microtiter Plates

4.1 Introduction

Neurological diseases such as Alzheimer's disease, Parkinson's disease, and autism affect millions of people worldwide. However, most of the drugs available for these diseases are ineffective. With the increased prevalence of phenotypic screening, new opportunities exist to discover both new targets and new drugs to treat these diseases. Of the 28 new small-molecule entities (NMEs) approved by the FDA between 1999 and 2008, seven were developed from phenotypic screens based on the central nervous system (CNS).[2]

The typical cost of a high throughput screening (HTS) campaign is estimated to be ~$1.00 per well or $500,000 for a screen of a half a million compounds.[3] These costs however are greatly increased for screens using primary cells because of the high cost of raising and sacrificing animals to harvest tissue. For neurons specifically, an even greater cost is incurred because of the post mitotic nature of these cells and the density with which they must be plated. Plating densities vary depending on the type of assay performed, but typically screens use between 5,000 – 20,000 neurons per well for proper growth and maturation[4; 5, 6]. In a high content screen using primary neurons to identify compounds that promote neurite growth, Al-

[1] This chapter previously appeared as an article in the Journal of Biomolecular Screening. The original citation is as follows:
1. Gordon KR, Wang YL, Allbritton NL, Taylor AM. 2015. Magnetic alignment of microelements containing cultured neuronal networks for high-throughput screening. Journal of Biomolecular Screening. 20(9):1091-1100.

Ali et al. used 1,000 cells per well in 96 well plates; however, these cells were fixed and imaged after 48 hours.[4]. For assays requiring functional neuronal networks, higher densities and longer culturing periods are required[7]. Thus due to the high costs and the large number of neurons required, there is an unmet need to develop higher throughput methods for neuronal screens. Plating neurons in 1,536 well microtiter plates would increase throughput, but this approach is hindered by evaporation issues and difficulty seeding cells at the bottom of the wells.

As highlighted in a recent review by Moraes, novel microfluidic and microengineered systems are quickly coming online to address the pitfalls that exist in modern screening methods[8]. Along these lines, we previously reported the use of 'microraft' array technology for screening (**Fig. 1A,B**). Using this technology we demonstrated the ability to increase the number of samples per unit cells > 30-fold[9]. Further, we successfully demonstrated the use of these microrafts in a previously established drug screening assay developed for Angelman's syndrome using embryonic cortical neurons from *Ube-3a-YFP* transgenic mice[5; 9]. These arrays contain 1,600 polystyrene microelements (each termed microraft) doped with paramagnetic nanoparticles and arranged in an array on a polydimethylsiloxane (PDMS) membrane (25.4 mm x 25.4 mm). Each microraft measures 500 x 500 x 200 µm and serves as a surface suitable for culturing cells[10; 11]. Cells are cultured *en masse* on the array and then microrafts are detached from the PDMS membrane and transferred either magnetically or via pipette to microtiter plates.

One foreseeable application of this technology to screening is in the area of high-content screening. High content screening is the simultaneous extraction of

data from multiple cellular parameters from many cells usually using high-content imaging systems[12]. High content imaging systems use automated platforms, plate and fluid handlers, and special software beyond that of regular microscopes, designed specifically for high density microtiter plates. Unlike plate readers, high-content imagers provide morphological and spatial information about the cells being screened[13]. This information is vital in screens for diseases such as Alzheimer's and fragile X syndrome where it is beneficial to observe synapse morphology and function. However, a major caveat to these systems is that in their automated processes, the objectives are usually positioned at the center of the wells by default as they traverse through the plate. Because microrafts are approximately 11 times smaller than the wells, they can be positioned at various locations at the bottom of the well. Therefore, to realize the potential for the microraft array technology and increase throughput for high-content screening, we focused on centering the small microrafts within the microtiter wells to facilitate automated imaging. To do this we developed a special magnet array plate which functions as a centering device to fully exploit the advantages of using microraft arrays for screens.

4.2 Materials and Methods

4.2.1 Design and Analysis

3D modeling and detailed drawings of the magnet array plate were created using SolidWorks 2012 (Dassault Systemes). Finite element analysis was performed using COMSOL Multiphysics Version 4.3 (COMSOL Inc.). Model I was created axial symmetrically, while Models II & III were created three dimensionally. In all cases the magnets were modeled with a relative permeability of neodymium of

1.05 and a remanent flux density of 1.48T which is characteristic of a 52 MGOe neodymium magnet. A “physics controlled” extra fine mesh was use in all models.

4.2.2 Magnet Array Plate Materials

The magnet array plate was fabricated from LEXAN polycarbonate. 384 magnets (Model D14-N52, K&J Magnetics, Inc.) were used for the plate. The magnets were cylindrical in shape with a diameter of ~1.6 mm and a length of 6.35 mm. These magnets are made of grade N52 NdFeB with a NiCuNi plating and a maximum field strength of 1.48 T.

4.2.3 Magnet Array Plate Fabrication

The magnet array plate was fabricated via a CNC milling process. Holes were drilled at max tolerance. Following the machining process, the magnets were inserted by hand and/or glued with cyanoacrylate when a snug fit was not available.

4.2.4 Microraft Array Fabrication

Microraft arrays were fabricated according to previously published methods[10; 11]. Briefly, soft lithography was used to make the poly(dimethylsiloxane) (PDMS) template containing an array of microwells (each well has width x length x height = 500 µm x 500 µm x 200 µm, array size = 25.4 mm x 25.4 mm). The PDMS template was then dip coated with a 20% polystyrene solution in gamma-butyrolactone (GBL) containing 4% iron oxide particles. The arrays are then placed in a convection oven at 95°C for 16 hours to evaporate GBL to create the microrafts. The array was glued to a polystyrene cassette to facilitate handling, and then surface treated with air plasma Harrick Plasma) for 2 min.

4.2.5 Microraft Transport

For this study microrafts were ejected from the array and individually transported to microtiter plates in ~5 µl volumes using a single channel pipette with a large orifice tip (Fisher Scientific; 02-707-134). Microtiter plates used for this study were 384-well Small Volume, LoBase, Polystyrene, µClear, black, tissue culture treated, sterile plates (Greiner BioOne; 788092)

Centering Performance Assessment

Centering performance was evaluated based on the percent centering and centering efficiency as follows (see **Fig. 4**):

$$\%\ Centering = \frac{(L - d)}{L} * 100$$

Where:

L = The distance from the center of the well to the center of the microraft when it is located flat on the bottom and against the edge of the well. (0.643 mm for Greiner BioOne 788092)

d = The distance from the center of the well to the center of the microraft at the position where it rests in the well.

$$Centering\ Efficiency = \frac{\#\ Wells\ \geq\ 75\%\ Cnt.}{Total\ \#\ Centered\ Wells}$$

Please note that in calculating centering efficiency, the value of % centered was taken relative to 75% as this value of centering represents that a sufficient portion of the centered microraft is within the field of view for automated imaging.

4.2.6 Cell Culture

All animal procedures were carried out in accordance with the University of North Carolina at Chapel Hill Institutional Animal Care and Use Committee (IACUC). Dissociated hippocampal cultures were prepared at embryonic day 18 from Sprague Dawley rat embryos as previously described[14] with some modifications. Briefly, hippocampal tissue was dissected in dissociation media (DM) containing 82mM Na2SO4, 30mM K2SO4, 5.8mM MgCl2, 0.25mM CaCl2, 1mM HEPES, 20mM Glucose and 0.001% Phenol red. Equal volumes of TrypLE Express (Invitrogen) and DM were added to the tissue and incubated at 37°C for 8 min. Tissue was then rinsed and gently triturated in Neurobasal media (NBM, Invitrogen) supplemented with 1x B27 (Invitrogen), 1x Antibiotic-antimycotic (Invitrogen), 1x Glutamax (Invitrogen). Dissociated cells were then centrifuged (67xg) for 7 minutes at 4°C, and resuspended ($12x10^6$ neurons/mL) in NBM. Prior to cell dissociation, microraft arrays were coated with poly-D-lysine (80 µg/mL; high molecular weight – 500-550 kDa) at 37˚C overnight and then rinsed three times with PBS. Neurons were then plated on the poly-D-lysine-coated raft arrays (1 million neurons/array). Rafts were released the following day and maintained in NBM until 8 DIV. We released and transferred the microrafts after 1 DIV because at this stage their processes are not long enough to extend over the PDMS borders between the microrafts while they are still embedded in the array. Waiting longer to release and transfer microrafts may cause injury to the neurons through shearing of processes that have grown over the borders.

4.2.7 Fluorescent dye labeling

The cell viability assay was performed as described previously[9]. Briefly, cells were grown for 8 DIV and then stained with a solution containing Sytox Green Nucleic Acid Stain (1:1000; Life Technologies, Inc.) and NucBlue Live Cell Stain Ready Probes/ Hoechst33342 (2 drops/mL; Life Technologies, Inc.) for 5 minutes at room temperature to label dead/dying cell nuclei and all cell nuclei respectively. Following staining, the cells were rinsed three times for two minutes each with PBS and then fixed for 30 minutes with 4% formaldehyde. After fixation, cells were rinsed three times for two minutes each with PBS and finally placed in 0.1% NaN_3 before imaging.

4.2.8 Imaging and Image Processing

Imaging was performed on an Andor XDi imaging system featuring a Yokogawa spinning disk confocal unit and an Olympus IX81-ZDC2 inverted microscope with a motorized stage by Ludl as described previously [15]. The speed of image acquisition of this spinning disk confocal imaging system is comparable to high content imagers (e.g., the BD Pathway) with a scan speed of 36 sec per well for 2-channel fluorescence.

Montages (2 x 2) were taken of each microraft with a 20X objective and stacks ranging from 10 – 20 slices each spaced 0.85 µm (z-distance) apart. Dead cells stained by Sytox were captured using 488 nm laser excitation and a 525-30nm single band fluorescence filter (Semrock Brightline), while the cell nuclei representing all cells were captured using 405 nm laser excitation and a 447-60nm single band fluorescence filter (Semrock Brightline). After acquisition, all images

were analyzed with ImageJ as described previously [9]. Briefly, images were imported using the Bio-formats plugin, slices were summed using maximum intensity projection, and then converted to 8-bit. The projected images were thresholded and the number of stained nuclei were counted within a 300 µm diameter region of interest in the center of the rafts using the 'Analyze Particles' command.

4.2.9 Statistical Analysis

Statistical analysis was performed using GraphPad Prism 6 software. Mean percent centering, centering efficiency, and percent viability were plotted as mean ± SEM. Statistical significance was tested with a nonparametric Mann-Whitney test. Statistical significance with p-values < 0.01 are indicated with asterisks. Correlation values for the magnetic field analysis were calculated using Microscoft Excel's correlation function which is based on the sample Pearson correlation coefficient.

4.3 Results

4.3.1 Design and Fabrication of Magnet Array Plate

The goal was to design a magnet array plate that would center microrafts within each well of a standard 384-well microtiter plate and be compatible with high-throughput fluid handling systems. The design of the magnet array plate began with the ANSI/SLAS 2004 micro-titer plate standard footprint, which has been adopted by all major manufacturers and defines the outside footprint and corner radius of all micro-titer plates regardless of their well density. Using this standard and typical well-to-well spacing found in 384-well microtiter plates, the geometry of the magnet array plate was designed in plan (**Figure 4.1C**).

In this design the magnets were positioned at the centers of each well with a center–to-center distance of 4.5 mm. Port holes located on the bottom of the plate, centered under each magnet, allow the insertion and ejection of the magnets at-will (**Figure 4.1D**). The outer rim of the plate is approximately 5 mm thick and serves to frame and secure the microtiter plate it supports.

The plate was designed to adapt with commonly used high-throughput fluid handling machines (e.g., Tecan or Hamilton) (**Figure 4.1D**). To magnetically secure the microrafts during automated fluid handling operations, we designed the magnet array plate to fit within fluid handling plate brackets designed for ANSI/SLAS 2004 microtiter plate footprints. The tops of the magnets were positioned flush with the top of the inside plate face and 2 mm above the channel. This design feature was intended to adhere to the design of low base microtiter plates such that the magnets are flush against the bottoms of these plate types. Low base plates are most commonly used in automated imaging as they facilitate the imaging of all wells including those located on edges, and the flushness of the mangnets is important for maximum attraction and centering of the microrafts to the bottom of the microtiter wells.The final design was machine milled from LEXAN polycarbonate, and features 384 neodymium magnets (**Figure 4.1E and F**).

4.3.2 Magnetic Field Analysis

Finite element modeling and analysis was performed to assess the nature of the magnetic field of the cylinder magnets relative to microrafts at various positions within the microtiter wells (**Figure 4.2A**). We modeled commercially available magnets and analyzed 1.5 mm diameter (smallest practical size for fabrication) and

1.6 mm diameter magnets which are both similar in diameter to wells of a low-base 384-well plate. Results using the 1.5 mm diameter (results not shown) and 1.6 mm diameter cylinder magnets clearly showed that the magnetic field in the axial direction peaked at the center of the magnet (**Figure 4.2B**) while the field in the radial direction peaked at the edge of the magnet (**Figure 4.2C**). Furthermore, both magnetic fields followed a non-linear decay the further away from the surface of the magnet (**Figure 4.2D**). Since the magnetic field in the radial direction peaks at the edge of the magnet it is more beneficial to use a magnet with a similar diameter to the bottom of the well thus allowing the magnetic field in axial direction which peaks at the center to dominate and better serve to center the microrafts. The 1.6 mm diameter magnet is nearly coincident with the area of the bottom of the well, so this magnet was selected and used in the remainder of the study.

We next analyzed whether field interference existed between adjacent magnets. We created a model with two magnets spaced exactly at the center-to-center distance of adjacent wells. When analyzing the magnetic field in both the axial and radial directions (**Figure 4.2E and F**)**,** we found a strong correlation (radial correlation = 0.986, axial correlation = 0.994) for both directions between the field of multiple magnets and that of a single magnet. Since the fields for multiple magnets were so similar to that of a single magnet we were able to conclude that there is no interference between adjacent magnets in our designed magnet array plate.

4.3.3 Magnetic Force Analysis

With the proper size of the magnet determined and the nature of the interaction between adjacent magnets understood, we next sought to determine the

force experienced by the microrafts at various locations within the microwells. It was important for us to understand the general trends of these forces in terms of how the forces on the microrafts relate to each other as their position changes both axially and radially within the well, but also how those forces relate to the force required to move the raft from a stationary positon on the well bottom which was calculated kinematically. Forces were analyzed at center, quarter, and edge positions and heights ranging from 0 – 600 µm above the bottom of the micro titer plate to evaluate the influence of different locations where the rafts would be positioned following transfer (**Figure 4.3A**). In the radial direction (**Figure 4.3B**) all locations were significantly less than the forces experienced in the axial direction, however these forces were still greater than the calculated 4.54×10^{-8} N force required to move a stationary microraft on the bottom of the microwell. The forces in the axial direction were clearly dominant over those in the transversal direction, due in large part to the size of the magnet relative to the microwell as previously discovered. More significant however was that for similar lateral positions (i.e. center, quarter, and edge locations), the forces were approximately the same (**Figure 4.3C**). This implies that microrafts falling along the side of the wall would still be centered.

4.3.4 Centering Performance Evaluation

After performing finite element analysis supporting the proper design of the magnet array plate, we next wanted to experimentally test the performance of our prototype. Our goal was to first test the effectiveness of centering using the magnet array plate compared to the use of a conventional flat magnet. We wanted to determine whether having the magnet array plate in place during loading or after

loading would yield equivalent centering efficiencies. The metrics used in these tests include percent centering and centering efficiency which are formulated in the Methods section (**Figure 4.4A and B**). Percent centering measures the amount the microraft is centered, with the center of the microtiter plate well coincident with the center of the microraft equal to 100% and the center of the microraft with one edge abutted against the edge of the well equal to 0%. This metric is calculated as the fraction of the distance from the center of the microtiter plate well to the center of the microraft divided by the distance from the center of the microtiter plate well to the center of the microraft when its edge is abutted against the edge of the well. To calculate the centering efficiency, we counted the number of times percent centering was greater than or equal to 75% and divided that by the total number of wells where rafts were not flipped on edge.

In our first test, the microtiter plate was positioned on top of the magnet array plate during loading of the microrafts (Test 1), and individual microrafts were transferred to the wells using a pipette as described in Methods. The centering performance of the magnet array plate was compared to a flat magnet plate which contains a single flat plate magnet with an area similar to that of the microtiter plate, and a control sample which used no magnets. The magnet array plate showed a mean percent centering of 88.16% compared to 7.8% for the flat magnet plate and 35.85% for the control (**Figure 4.4C and D**). For the centering efficiency, the magnet array plate performed at 100% versus 4.35% for the flat magnet plate and 17.86% for the control (**Figure 4.4E**), demonstrating that whenever the magnet array plate is in use, it centers the microrafts to 75% or better. This is excluding the

number of times the microrafts flipped on edge. For the magnet array plate this happened 10% of the time while the flat magnet plate was 20% and the control was 3% (**Figure 4.4F**). When the microrafts land on their edge it renders that well useless in a high content screen because the cells cannot be imaged, therefore it is critical to know the frequency in which this happens. We believe however that the times in which microrafts flipped on their edge can be attributed to a small amount of magnets that were placed in the reverse direction while manually inserted during the fabrication process. Furthermore we believe that this statistic can easily be decreased by correcting this problem and increasing our sample size.

Although it did not occur in this study, in rare instances microrafts may land cell side down. However, in these instances neither screening nor imaging is affected because the microrafts are slightly concave on their top surface which prevents the adhered cells from coming in contact with the bottom of the well when it lands cell side down. This concavity also conveniently allows for similar objective distances whether or not the microraft is cell side up or cell side down[11]. We found that the microrafts land cell side up the majority of the time and we believe this may be attributed to the drag created from the slight concavity on the top surface of the microrafts.

To observe whether the magnet array plate was able to center microrafts after microraft loading, we loaded microrafts into the micro-titer plate, let them settle, and then placed the microtiter plate on top of the magnet array plate (Test 2). Images show that the microrafts were initially scattered within the wells, but after placing the micro-titer plate on the magnet array plate, centering was achieved (**Figure 4.4G**).

When quantified, the mean centering was 10.8% before placement versus 78.1% after placement (**Figure 4.4H**). Finally, comparing the technique used in Test 1 versus Test 2, the centering efficiency was 100% versus 66.7% respectively (**Figure 4.4I**). This result shows that to best achieve centering, it is better to first place the microtiter plate on top of the magnet array plate before loading the microrafts. However should the microrafts become decentered as the result of the movement or the plate being hit, centering can still be achieved by placing the loaded microtiter plate back on the magnet array plate. We've determined however that dislodging of the microrafts is unlikely as it would require moving the plate at a speed of 5.66 ft/s (calculation not shown) and stopping abruptly in order to create enough inertial force to overcome the frictional forces holding the raft in place.

4.3.5 Cell Viability Evaluation

We successfully demonstrated the ability of the magnet array plate to center microrafts. As a final measure of performance, we tested whether centering the microrafts affected cell viability. With the added acceleration of the microrafts, beyond that of gravity, due to the attractive force of the magnet, there was some concern that increased fluid shear forces may endanger the neurons attached to the microrafts. To determine if this was a threat, a cell viability assay was performed to determine the differences in viability between unreleased microrafts, microrafts which have been released and transferred, and microrafts which have been released, transferred, and centered.

Primary hippocampal neurons were plated on a microraft array at a density of 1 million cells. After 1 DIV the microrafts were released from the array and

transferred to a 384-well micro titer plate. At 8 DIV cell viability was quantified using a live/dead assay and immunostaining for MAP2 was used as a neuronal marker to characterize neuronal morphology (**Figure 4.5A, B**). After imaging and quantification, the results showed that centering the cells had no significant effect on cell viability compared to unreleased or released and transferred microrafts (**Figure 4.5C**).

4.4 Conclusions

Although other magnetic plates exist commercially, mostly used for PCR assays, these plates are usually designed for 96-well microtiter plates, and operate by pulling magnetic beads to the side of the wells. To the authors' knowledge, the magnet array plate described herein is the only one designed for high throughput screening in 384-well microtiter plates and is unique in that it centers microraft culture platforms which offer the opportunity to scale-up screening for neurological diseases.

With a well-to-well spacing half that of 96-well microtiter plates, fabricating a 384 magnet array plate can be difficult because of the risk of thermally induced cracking when drilling the magnet holes. For this reason we wanted to use a hard plastic with a low glass transition temperature to comply with the heat produced during machining. LEXAN is form of polycarbonate which has a relatively low glass transition temperature and an extremely low thermal expansion coefficient, which allows it to be machined relatively easily without cracking.

Another factor in the fabrication of the plate was imaging. Importantly, we found that after the magnet array plate centers the microrafts, they remain in place

after removing the magnet array plate and also while subjected to mild perturbations. Thus it is unnecessary for the magnet array plate to be in place during imaging. However, an additional reason why LEXAN was chosen was its semi-translucency. This characteristic is beneficial for situations in which microrafts must be centered and secured while simultaneously performing tasks and imaging stereoscopically.

In creating the magnet array plate, one of the unique design features is its ability to fit within commercial fluid handling machines which allows it to secure the microrafts during fluid processes while preserving their centered position for imaging. In honing this design we conducted a thorough analysis and concluded that it was better to use magnets similar in diameter to the microtiter well in order to achieve the best centering results. Smaller magnets would trap the microrafts at the magnet edge where the field in the radial direction peaks, and prevent centering. Our design decision was confirmed by our empirical results which not only showed a centering efficiency far beyond that of a flat magnet plate, but also proved that it is preferable to have the magnet array plate positioned under the microtiter plate prior to loading the microrafts. This conclusion concurred with our analysis that microrafts loaded with a magnetic field already in place aligned themselves with the axial field and they were drawn towards the center where this field peaks. However when loaded prior to placement of the magnetic field, the settled microraft at the bottom of the well must rely on a weak radial field to be centered. Although this radial field is weaker, we found that centering occurred after microrafts randomly settled within the microtiter plate well as shown in Test 2. This result is important in the event that

microrafts become dislodged from their centered position, although our calculations show it would take a significant amount of acceleration for dislodging to occur.

Finally, viability experiments further validated the effectiveness of the magnet array plate proving that neither transporting, nor transporting *and* centering create adverse effects on cell viability. These experiments concluded the overall success of this tool as a device to center paramagnetic microraft culture platforms for automated imaging, opening the opportunity for these microrafts to reduce costs, preserve animal life, increase throughput, and make cell-based screens of neurological disorders more accessible.

4.5 Tables & Figures

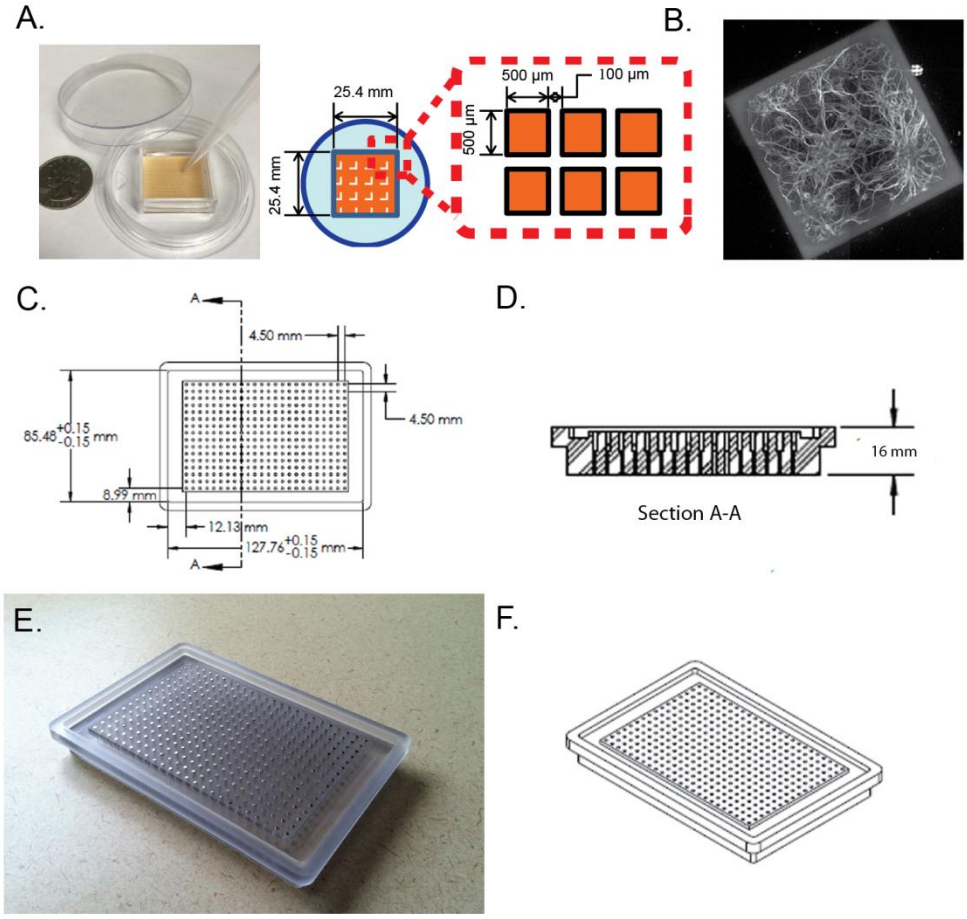

Figure 4.1. Microraft arrays and three dimensional modeling and drawings of the magnet array plate. (A) Photograph of microraft array with schematic drawing showing dimensions. (B) MAP2 immuno stained neurons cultured on a single microraft. (C-D) Computer-aided design (CAD) drawings of magnet array plate, plan and section views. (E) Photograph of magnet array plate. (F) CAD renderings of the magnet array plate in isometric view.

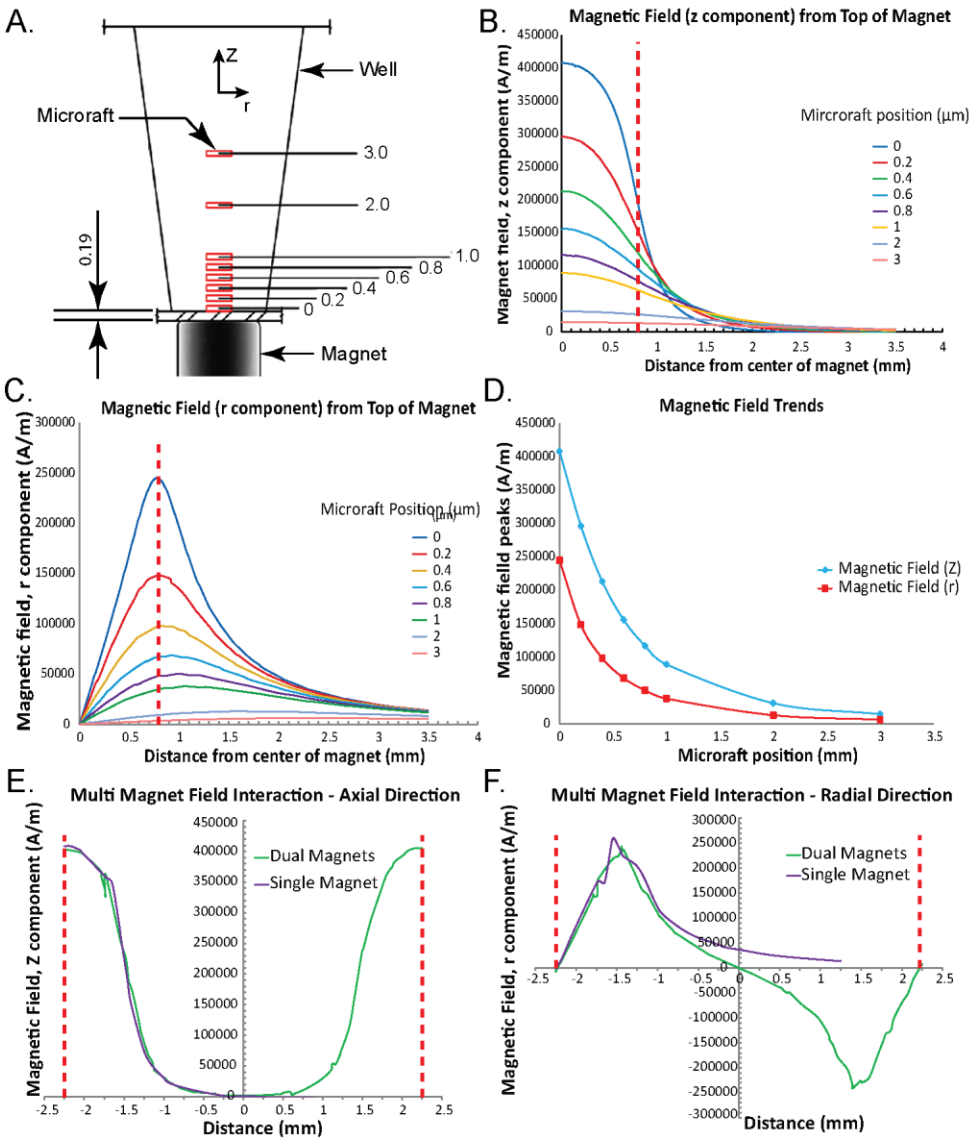

Figure 4.2. Results of the magnetic field analysis of a microraft at various heights within a microtiter plate well. The magnetic field peaks in the center and edge in the axial and radial directions of the microwell, respectively. Adjacent magnetic fields do not interfere. (A) Analysis positions of microrafts (in µm) in the axial (Z) direction. Red rectangles represent microrafts. (B) Magnetic field in the axial direction. (C) Magnetic field in the radial direction. (D) Magnetic field decay curves. (E) Dual magnet field in the axial direction. (F) Dual magnet field in the radial direction. For B and C, the red dashed line represents the outside edge of the cylinder magnet. For E and F, the red dashed line represents the center axis of the cylinder magnet.

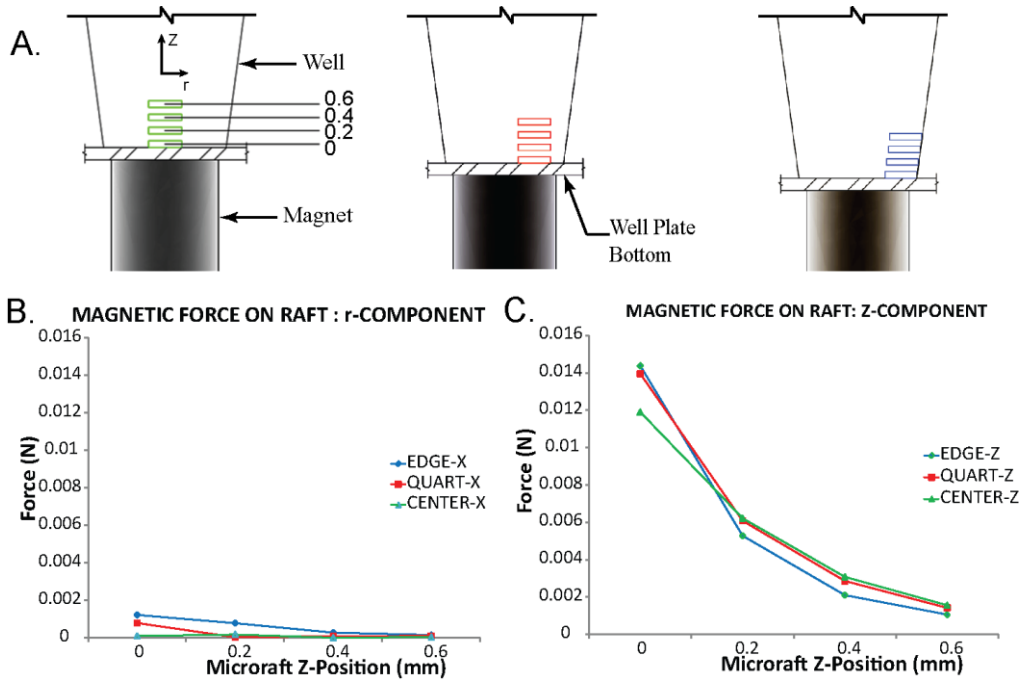

Figure 4.3. Magnetic force analysis of microrafts at different axial (Z) and radial positions. (A) Analysis positions of microrafts (in µm) in the axial direction in the center, quarter, and edge of the well, respectively. Rectangles represent microrafts. (B) Magnetic force on microraft in the radial direction. (C) Magnetic force on microraft in the axial (Z) direction.

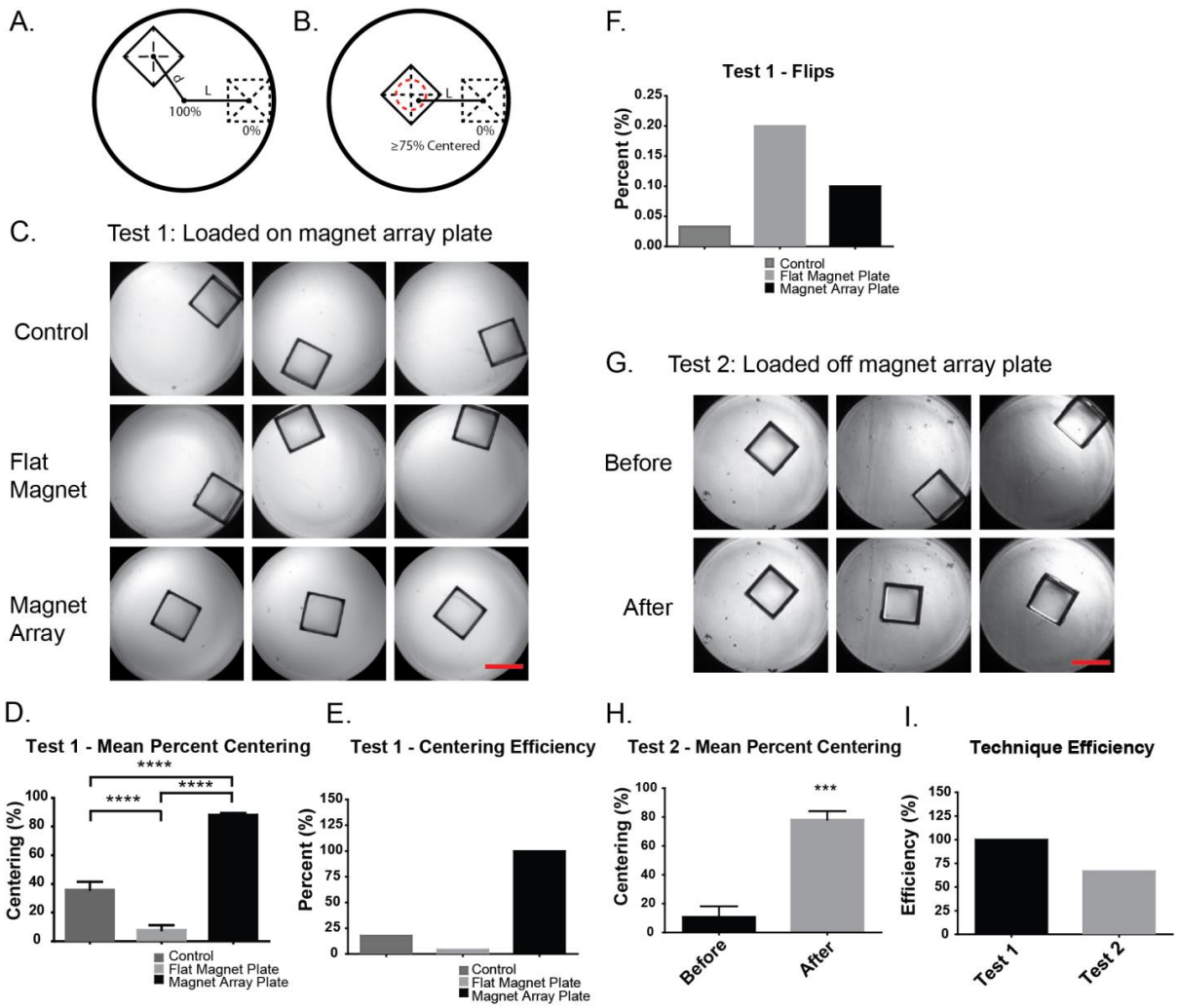

Figure 4.4. The magnet array plate effectively centers the microrafts. (A) Percent centering metric in which 100% represents the center of the microwell and 0% represents the microrafts abutted against the microwell. *d* represents the distance of the microraft from the center of the microwell, and *L* is the distance between 0% and 100% centering. (B) Centering efficiency in which the red dashed line represents a ≥75% centered value. (C) Representative images of Test I centering. (D) Test I mean percent centering. (E) Test I centering efficiency. (F) Percentage of microrafts flipped on edge. (G) Representative images of Test 2 centering. (H) Test 2 mean percent centering. (I) Overall technique efficiency. For all n=30. ****=p<0.0001; scale bar = 500 µm.

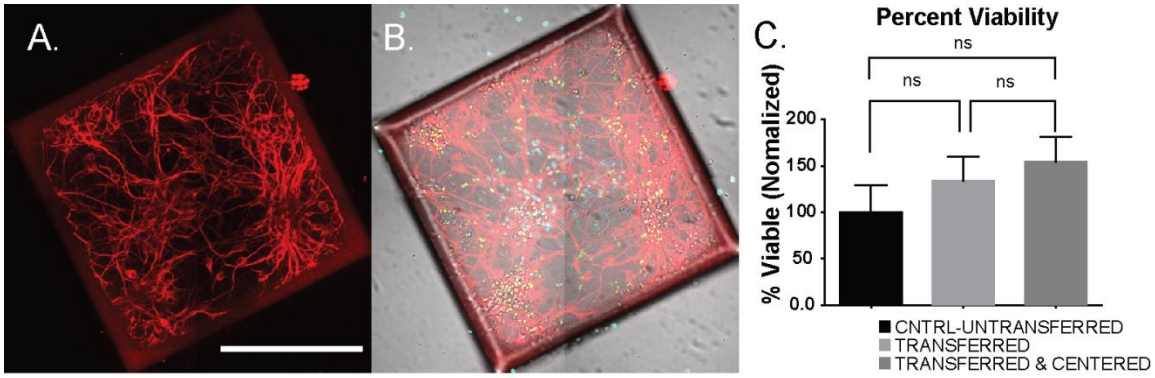

Figure 4.5. Cell viability was not affected by the transfer and centering process. (A) neurons cultured for 8 days on released and transferred microrafts are immunolabeled for MAP2 (red), a neuron specific marker; scale bar = 250 µm. (B) Merged image of MAP2 (C) Percent viability results (n=12 wells). Stain located off of microraft is dead cell debris.

4.6 BIBLIOGRAPHY

1. Gordon KR, Wang YL, Allbritton NL, Taylor AM. 2015. Magnetic alignment of microelements containing cultured neuronal networks for high-throughput screening. Journal of Biomolecular Screening. 20(9):1091-1100.

2. Zhang MH, Luo GR, Zhou YJ, Wang SH, Zhong Z. 2014. Phenotypic screens targeting neurodegenerative diseases. Journal of Biomolecular Screening. 19(1):1-16.

3. An WF, Tolliday NJ. 2009. Introduction: Cell-based assays for high-throughput screening. In: Clemons PA, Tolliday NJ, Wagner BK, editors. Cell-based assays for high throughput screening: Methods and protocols. New York, NY: Human Press. p. 218.

4. Al-Ali H, Schuerer SC, Lemmon VP, Bixby JL. 2013. Chemical interrogation of the neuronal kinome using a primary cell-based screening assay. Acs Chemical Biology. 8(5):1027-1036.

5. Huang HS, Allen JA, Mabb AM, King IF, Miriyala J, Taylor-Blake B, Sciaky N, Dutton JW, Lee HM, Chen X et al. 2012. Topoisomerase inhibitors unsilence the dormant allele of ube3a in neurons. Nature. 481(7380):185-+.

6. Götte M, Hofmann G, Michou-Gallani A-I, Glickman JF, Wishart W, Gabriel D. 2010. An imaging assay to analyze primary neurons for cellular neurotoxicity. Journal of Neuroscience Methods. 192(1):7-16.

7. Biffi E, Regalia G, Menegon A, Ferrigno G, Pedrocchi A. 2013. The influence of neuronal density and maturation on network activity of hippocampal cell cultures: A methodological study. PLoS One. 8(12):e83899.

8. Moraes C. 2015. The discovery channel: Microfluidics and microengineered systems in drug screening. Integrative Biology.

9. Niedringhaus M, Dumitru R, Mabb AM, Wang Y, Philpot BD, Allbritton NL, Taylor AM. 2015. Transferable neuronal mini-cultures to accelerate screening in primary and induced pluripotent stem cell-derived neurons. Sci Rep. 5:8353.

10. Gach PC, Wang Y, Phillips C, Sims CE, Allbritton NL. 2011. Isolation and manipulation of living adherent cells by micromolded magnetic rafts. Biomicrofluidics. 5(3):32002-3200212.

11. Wang YL, Phillips C, Xu W, Pai JH, Dhopeshwarkar R, Sims CE, Allbritton N. 2010. Micromolded arrays for separation of adherent cells. Lab on a Chip. 10(21):2917-2924.

12. Al-Ali H, Blackmore M, Bixby JL, Lemmon VP. 2013. High content screening with primary neurons. In: Sittampalam G, Coussens N, Nelson H, editors. Assay

Guidance Manual [Internet]. Bethesda, MD: Eli Lilly & Company and the National Center for Advancing Translational Sciences.

13. Jones E, Michael S, Sittampalam GS. 2012. Basics of assay equipment and instrumentation for high throughput screening. In: Sittampalam G, Coussens N, Nelson H, editors. Assay Guidance Manual [Internet]. Eli Lilly & Company and the National Center for Advancing Translational Sciences.

14. Taylor AM, Wu J, Tai HC, Schuman EM. 2013. Axonal translation of beta-catenin regulates synaptic vesicle dynamics. J Neurosci. 33(13):5584-5589.

15. Hallfors N, Khan A, Dickey MD, Taylor AM. 2013. Integration of pre-aligned liquid metal electrodes for neural stimulation within a user-friendly microfluidic platform. Lab on a Chip. 13(4):522-526.

Chapter 5: Protein Measurement Assay using Microrafts

5.1 Introduction

One of the most direct approaches for discovering new treatments for fragile x syndrome is to identify compounds that unsilenced the fmr1 gene and produce FMRP. In recent years assays have been developed to detect and measure FMRP in a number of ways.

In 2009 Iwahashi developed a quantitative enzyme-linked immunosorbent assay (ELISA) to detect FMRP in peripheral blood lymphocytes. Using 96-well plates and luminescence as a readout, this assay proved to be accurate and reliable in detecting FMRP throughout the biologically relevant range of protein concentrations.[1]

In a similar yet less complex approach, Schutzius developed a time-resolved Forster's resonance energy transfer (TR-FRET) assay for measuring FRMP using maltose binding protein (MBP)-FMRP and patient peripheral blood mononuclear cells. This assay was performed in 384-well format with 5 µL of sample lysate per well.[2] Following this development, in 2015 Kumari, also using a TR-FRET assay performed a screen of 5,000 compounds to identify candidates which increase FMRP expression in patient iPSC-derived neural stem cells. Using a standard plate reader for detection, cells were screened in a 1,536-well format with 2,500 cells per

well. Unfortunately, this screen produced six hits which only produced small increases in FMRP expression.[3]

Finally, in another approach, Kaufmann et al. in 2015 used a high-content imaging assay to screen 50,000 compounds to identify potential candidates which upregulate production of FMRP in patient iPSC-derived neural progenitor cells. In this process, cells were fixed and stained with an anti-FMRP antibody in a 384-well format with 20,000 cells per well. The screen identified only a small subset of compounds that produced a weak but noticeable expression of FMRP.[4]

In this chapter an assay is developed to measure FMRP from recombinant sources as well as cell lysate in an effort to demonstrate the use of microrafts in a scalable high-throughput screening assay. This assay is composed of a two stage process in which the microrafts in each well are first quantified in a high-throughput manner to normalize the resulting data, and then FMRP is measured. Two approaches were explored for the FMRP detection including a bead-based ELISA using flow cytometric for data acquisition and an immunofluorescence assay.

5.2 Methods

5.2.1 Rhodamine B Microraft Fabrication

Microrafts were infused with Rhodamine B (Sigma R6626) fluorescent dye by adding it to the magnetic polystyrene solution at 0.01 wt%. The solution was then mixed for >1 hr on a standard bottle roller for even distribution. The microrafts were then created through the dip-coating process as previously described.

5.2.2 Quantification of Microrafts

Microrafts were quantified via fluorescence using a Perkin Elmer Envision 2103 multilabel plate reader. Fluorescence detection was set to the emission spectra wavelength of Rhodamine B and measurements were conduction in a well-to-well sequential order with 25 (5 x 5) detections per well. The protocol was optimized for Greiner Small Volume, Lo Base, 384-well microtiter plate (788096).

5.2.3 Cell Culture

All animal procedures were carried out in accordance with the University of North Carolina at Chapel Hill Institutional Animal Care and Use Committee (IACUC). Dissociated hippocampal cultures were prepared at embryonic day 18 from Sprague Dawley rat embryos as previously described[5] with some modifications. Briefly, hippocampal tissue was dissected in dissociation media (DM) containing 82mM Na2SO4, 30mM K2SO4, 5.8mM MgCl2, 0.25mM CaCl2, 1mM HEPES, 20mM Glucose and 0.001% Phenol red. Equal volumes of TrypLE Express (Invitrogen) and DM were added to the tissue and incubated at 37°C for 8 min. Tissue was then rinsed and gently triturated in Neurobasal media (NBM, Invitrogen) supplemented with 1x B27 (Invitrogen), 1x Antibiotic-antimycotic (Invitrogen), 1x Glutamax (Invitrogen). Dissociated cells were then centrifuged (67xg) for 7 minutes at 4°C, and resuspended ($12x10^6$ neurons/mL) in NBM.

5.2.4 Cell Lysis and Recombinant FMRP

Cells were lysed using RIPA buffer (Sigma R0278) according to the manufacturer's procedure. Briefly, growth media was first aspirated from the cells. Then cells were gently washed twice with DPBS. Ice cold RIPA buffer was then

added to each well and incubated on at 4°C for five minutes. The cellular material was then scraped from the coverslips and aspirated up and down vigorously 3-4 times. On the last aspiration, the cell lysate is removed and placed in a chilled tube and centrifuged at at 8,000 g for 10 minutes at 4°C to clarify. Finally, the lysate was stored at -80°C for later use.

For experiments using recombinant protein, FMRP overexpression lysate (native) (Novus Biologicals NBP2-08154) was used. This protein was created from plasmid transfected HEK293T cells based on NP_002015.

5.2.5 ELISA Assay

DevScreen Streptavidin QBeads (Intellicyt Inc.) were briefly centrifuged. The bead vial was then Vortexed for ~30 seconds to thoroughly mix the beads. The appropriate volume of bead solution was then tranfered to a 1.5 mL microcentrifuge tube. The sample was then centrifuged at 8,000 g for 5 minutes followed by removal of the supernatant and resuspension in the appropriate volume of PBS-1%BSA. Capture antibody (US Biological, F6072-10G-Biot) was then added to the bead solution at the necessary concentration and the combined solution was vortexed to evenly mix. The bead-capture antibody solution was then incubated at room temperature for 2 hrs.

Following incubation, the bead-capture antibody solution was washed twice by centrifuging at 8,000 g for 5 minutes, removing the supernatant, adding PBS-1%BSA and repeating. Ten microliters of this solution were then added to each well of a 384-well plate. Ten microliters of sample (lysate, recombinant FMRP) were

then added to the solution in each well and this combination was incubated overnight at room temperature on an orbital shaker.

Following overnight incubation, 10 µL of detection antibody (Developmental Studies Hybridoma Bank, University of Iowa, 2F5-1-s) solution at the appropriate concentration was added to this rest of the mixture. The combined solution was then incubated for 1 hour at room temperature. Lastly, the secondary conjugated antibody was added and incubated room temperature for 1 hour.

5.2.6 Flow Cytometry

FMRP was measured on an iQue Screener Plus (Intellicyt Inc.). The settings were used in data acquisition:

Laser acquisition:	blue
Pre-plate shake:	180 secs at 1800 rpm
Sip time:	30 sec
Pump speed:	19 rpm

5.2.7 Immunofluorescence

For the final immunofluorescence assay, media was first removed from the 384-well plate and replaced with the same volume of Neurobasal media containing DRAQ5 nuclear dye (1:500; Thermo Scientific). After incubating for five minutes at 37°C, the dye solution was aspirated and cells were fixed for 30 minutes with 4% formaldehyde in PBS containing 40 mg/ml sucrose 1 µm $MgCl_2$, and 0.1 µm $CaCl_2$. After fixation, cells were rinsed three times for two minutes each with PBS. Neurons were permeabilized in 0.25% Triton X-100 for 15 min and then blocked in PBS containing 10% goat serum for 15 min. Primary antibodies to FMRP (1:10; mouse ;

2F5-1 [developed by Tartakoff, A.M./Fallon, J.R. and obtained from the Developmental Studies Hybridoma Bank developed under the auspices of the NICHD and maintained by the University of Iowa, Department of Biology, Iowa City, IA 52242]) was diluted in PBS with 1% goat serum and incubated overnight at 4°C. AlexaFluora goat anti-mouse conjugated to a 488 nm fluorophore (1:1000; Invitrogen) was diluted in PBS and incubated for 1 h at room temperature.

5.2.8 Image Acquisition

Imaging was performed on an Olympus FV1000 inverted confocal microscope with motorized stage. Images were capture with a 20X LUCPLFLN objective and a 488 nm multiline Argon laser and 633 nm Helium-Neon laser for FMRP and DRAQ5 excitation respectively.

5.2.9 Image Analysis

After acquisition, all images were analyzed with ImageJ. Images were imported using the Bio-formats plugin, slices were summed using maximum intensity projection, and then converted to 8-bit. The 488 nm and 633 nm channels were split, and the projected images were thresholded. The area of FMRP was quantified within a 300 µm diameter circular region of interest in the center of the microrafts using the ‘Analyze Particles’ command.

5.2.10 Statistical Analysis

Statistical analysis was performed using GraphPad Prism 6 software. FMRP area was plotted as mean ± SEM. Statistical significance was tested using one-way ANOVA with p-values < 0.001 are indicated with asterisks.

5.3 Results

5.3.1 Quantification of Microrafts

Measuring cellular FMRP using microrafts where more than one raft is in each well requires normalization of the data, so each well can be properly compared to each other. Therefore, in order to count the number of microrafts per well in a high-throughput fashion, a method was conceived were the microrafts were infused with fluorescent dye, and then the fluorescence would be detected using a plate reader. Thus, the number of rafts would be proportional to the fluorescence intensity of the well.

To test this concept, an initial experiment was designed and performed (results not shown) to insure that Rhodamine B could be detected in small volumes. For this experiment, Rhodamine at 0.01 wt% (the same concentration used for the microrafts) was aliquoted at 10 µL per well, and controls of Celltiter Glo, and blank wells were used to assess the difference in fluorescence. With wells containing Rhodamine, Celltiter Glo, Rhodamine plus Celltiter Glo, and blank wells, it was observed that the Rhodamine was easily detected above the Celltiter Glo which is normally detected through luminescence, not fluorescence. Furthermore, at 50 µL, the Rhodamine showed at higher fluorescence demonstrating a certain scaling effect of the signal.

With this information, the microrafts were fabricated with the Rhodamine B as described in the Methods section. Arranged in populations of 0, 1, 2, 3, 4, and 5 microrafts as well as a random population (**Figure 5.1**), the plate was scanned using a Perkin Elmer plate reader. This scan produces a heat map of each well and the

sums the total fluorescence for that well (**Figure 5.2 and Figure 5.3A**). This process was greatly aided by the magnet array plate in centering the microrafts as it helped focus the fluorescence signal to the center of the well. Using the midpoints between the min and max fluorescence for each group (**Figure 5.3B**), an algorithm was created to estimate the number of microrafts per well. Testing this algorithm on the random population produced a 98% success rate at identifying the correct number of microrafts in those wells.

5.3.2 Development of Screening Assay

In order to demonstrate the high-throughput capability of the microrafts, a scalable screening assay needed to be developed to show that useful information related to a disease marker could be extracted in a cell-based screen. In selecting the type of assay, it was critical to choose one with very high sensitivity because each microraft supports only a few hundred cells and thus produces a small amount of FMRP. It was also important to choose an assay and platform that had high-throughput capabilities. For these reasons, a bead-based enzyme-linked immunosorbent assay (ELISA) was chosen using flow cytometry to interrogate each bead and measure any bound FMRP (**Figure 5.4**). The iQue Screener Plus from Intellicyte Inc. was used for the flow cytometric analysis because it's specifically designed for high-throughput applications, capable of working with 384- and 1536-well plates.

5.3.2.1 Assay Proof of Principle

In the first experiment conducted, the previously described assay was tested with cell lysate from hippocampal rat neurons as a proof of principle. The goal in this

case was to detect a signal produced from the capture of FMRP contained within the lysate compared to a set of controls. After analyzing the results, it was observed that a significant signal was detected above the blank beads and the beads combined with capture antibody (**Figure 5.5**). The sample signal was also higher than the last condition in which beads were combined with the capture antibody, detection antibody, and secondary antibody. However, the difference between these signals was not statistically significant. Furthermore, the result of such a high signal without the presence of lysate is a strong indication of non-specific binding of the detection and secondary antibodies.

5.3.2.2 Antibody Concentration Optimization

To determine the optimal capture and detection antibody concentration, various dilutions were tested including $^{1}/_{100}, ^{1}/_{250}, ^{1}/_{500}, ^{1}/_{1000}, ^{1}/_{2000}$ for the capture antibody combined with detection antibody in dilutions of $^{1}/_{2}$, $^{1}/_{5}$, $^{1}/_{10}$. However, in analyzing the results (not shown), there was only minor differences in the fluorescence between these groups. These unfortunate results were further evidence of non-specific binding.

In an effort to determine if the results of this experiment were affected by an environmental element, another experiment was conducted in which the capture antibody was diluted to $^{1}/_{100}, ^{1}/_{500}, ^{1}/_{1000}$ and the detection antibody was diluted to $^{1}/_{2}$, $^{1}/_{5}$, $^{1}/_{10}$. In both cases it was expected that signal would reduce according to reduction in the capture and detection antibody concentrations, but instead there was no clear trend. As expected, the max and mean fluorescence for

these groups was above the negative control (beads + capture ab), however, compared to the other negative control (detection ab + secondary ab) they were almost equivalent. It's not exactly clear why the fluorescence levels for the second negative control were so high since there were no beads present, but it could possibly be due to aggregation of the antibody or somehow an errant bead or beads in the wells.

In addressing these errors another experiment was conducted in which the samples and controls were spread even further from each other on the plate in order to avoid errant beads that may have traversed into other wells during the shaking phases of the data acquisition protocol. Additionally, the plate was washed before data acquisition to remove any loose antibody floating in the samples in an effort to reduce antibody aggregation. Even with these measure however, there was still no clear trends among the dilutions and even some strange spikes in fluorescence representing inexplicable outliers. Furthermore, controls without lysate but all the other components for the ELISA showed very high fluorescence indicating a high occurrence of non-specific binding of the antibodies.

In order to better assess the problem of non-specific binding and determine what the cause was, another experiment was devised eliminating the antibody dilution series and increasing the number of controls (**Figure 5.6**). In addition, the recombinant FMRP was used at a low concentration (1/250) and a high concentration (1/50).

Upon removal of major outliers, it was clear from the analysis of this new data (**Figure 5.7A and B**) that the probable cause of the non-specific binding was due to

interaction between the bead and the secondary antibody or the capture antibody and the secondary antibody. To investigate this hypothesis, another experiment was performed with very low and extreme dilutions of the secondary antibody with the logic that previous experiments had an excess amount (**Figure 5.8**). Unfortunately even a vastly diluted secondary antibody only reduced, but did not eliminate the non-specific binding problem (**Figure 5.9**). And the presence of outliers only highlighted the inconsistencies between samples.

In a final effort to show that the same results arise when microrafts are used, primary hippocampal rat neurons were cultured on a microraft array. After plating the neurons, the microrafts were released and transferred after 1 DIV and transferred to a 384-well plate for additional growth. After 2 DIV the cells were lysed, and the lysate was used in the same bead-based ELISA as previously discussed. Similar to the previous experiments however the samples did not create signals above that of the controls suggesting that the presence of the microrafts did not change the outcome in any way (**Figure 5.10**).

5.3.3 Immunofluorescence FMRP Measurement

Due to the surprising results of the bead-based ELISA, an immunofluorescence assay was performed to show that FMRP could be measured using the microrafts by other means. Demonstrating FMRP immunofluorescence measurement is also important for its use in high-content screening.

For this experiment three microraft arrays were plated with densities of 1 MM, 500 K, and 250 K respectively in order to show that different amounts of FMRP could be measured. Blank microrafts were used as a control, and Draq 5 was used

as a co-localized stain of the nucleus. Microrafts were released and transferred after 1 DIV to a 384-well plate and then fixed and stained after 4 DIV.

Using confocal microscopy and FIJI image analysis, it was found that smaller cell densities produced significantly smaller amounts of FMRP (**Figure 5.11**). Furthermore, as previously reported, FMRP was localized around the cell nucleus as it serves as an mRNA shuttle protein (**Figures 5.12 – 5.15**).

5.4 Conclusions

In using manual transfer methods such as the magnetic wand or pipette, it is important to have a high-throughput method for quantifying microrafts. Regardless of the type of assay used, knowing the number of microrafts per well prior to data acquisition is important because this information allows you to accurately compare each well on a relative basis.

Fabricating the microrafts with Rhodamine B and scanning them with a standard plate reader produced very positive results, and it's clear that this method represents a fast high-throughput solution for quantifying the microrafts. Although there were some inconsistencies in fluorescence between plates, the main algorithm can be simply modified for each run sot maintain the high success rait in counting the microrafts.

It was unfortunate the quantification method could not be used for the bead-based ELISA. The bead-based ELISA, selected for its sensitivity, to measure FMRP overall failed to produce a signal significantly above the negative controls, and there were some inconsistencies between wells of the same sample groups. Based on

analysis of the investigative experiments performed, it was clear that these results were caused by some sort of non-specific binding between the secondary antibody and the bead or capture antibody. Unfortunately steps to ameliorate this such as dilution or plate washing did not have positive impacts on the outcome.

In theory, this bead-based ELISA should be effective in measuring small quantities of FMRP since each bead is individually interrogated in the flow cytometer. Therefore, future efforts will require the testing of many types of beads, capture antibodies, as well as custom made detection antibodies preconjugated to fluorophores in order to eliminate the need for a secondary antibody. Unfortunately the means for this type of campaign was not within the financial scope of this project.

As an alternative to the bead-based ELISA, immunofluorescence was used to measure FMRP, and this showed positive results. FMRP could reliably be measured using image analysis, and was proportional to the cell density used. Such results suggest that this approach could be used in a future high content screen. High content screening provides rich phenotypic information, but is also very costly and time consuming. Such a endeavor requires optimization of cellular staining, image acquisition, and image analysis. Future work along these lines would pair FMRP immunofluorescence with other morphologic and functional markers such as spine density and electrophysiology.

5.5 Tables & Figures

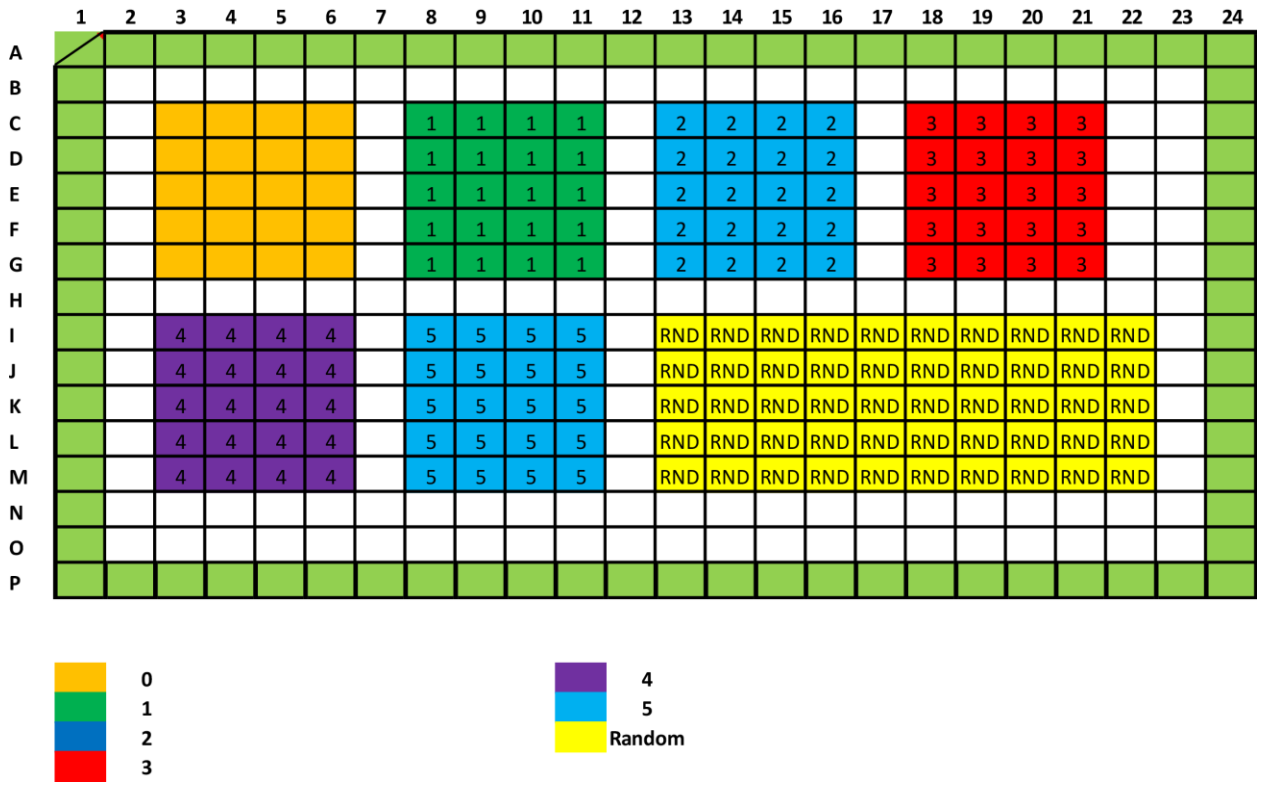

Figure 5.1 384-well microplate experimental layout showing distribution of different numbers of microrafts per well.

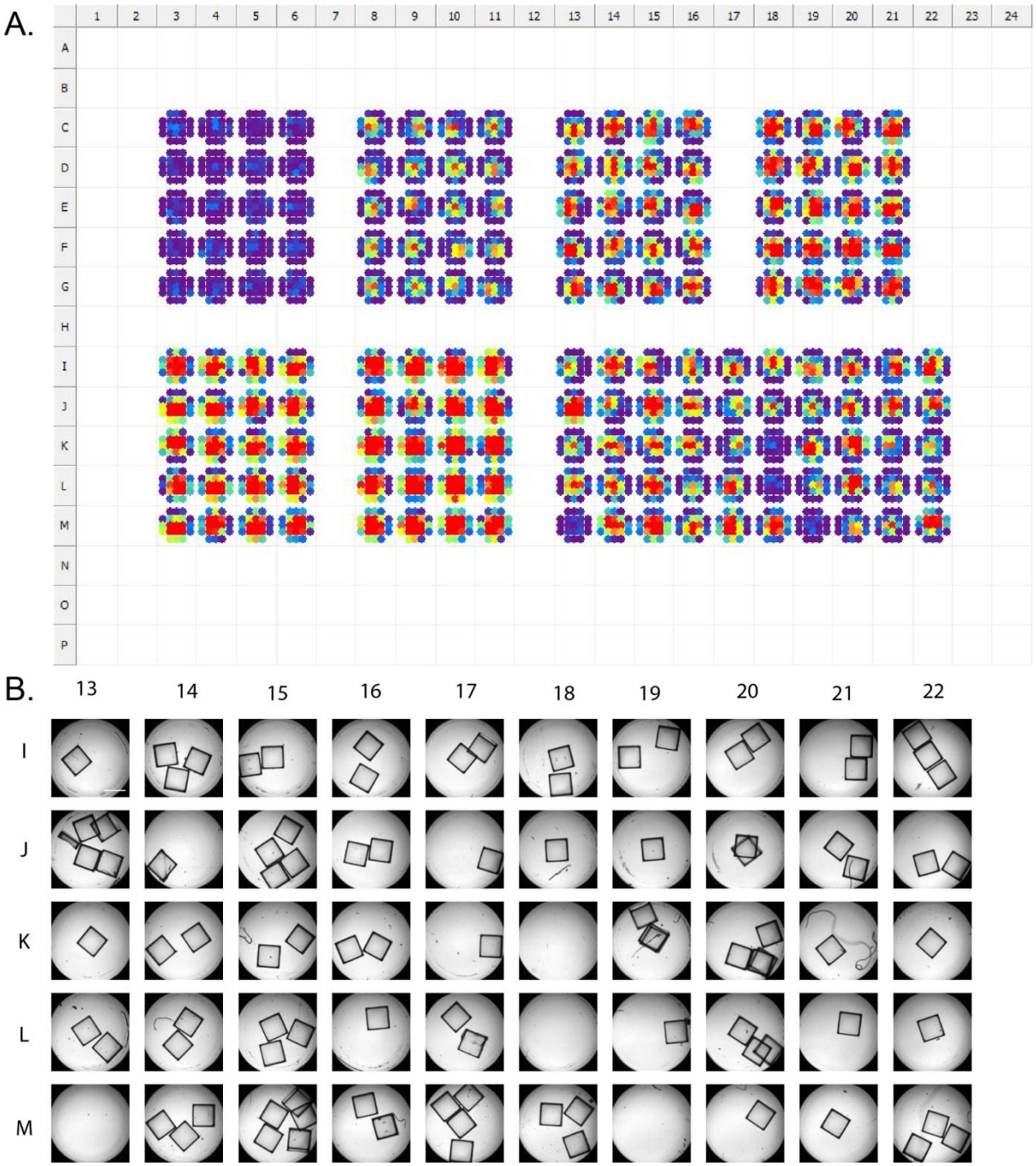

Figure 5.2 Rhodamine B infused microrafts quantified using plate reader. (A) Plate reader heat-map showing variance in fluorescence relative to the number of microrafts per well. (B) 10X Images of microrafts in microwells from the "Random" group. Scale bar in the image represents 250 µm (same for all images)

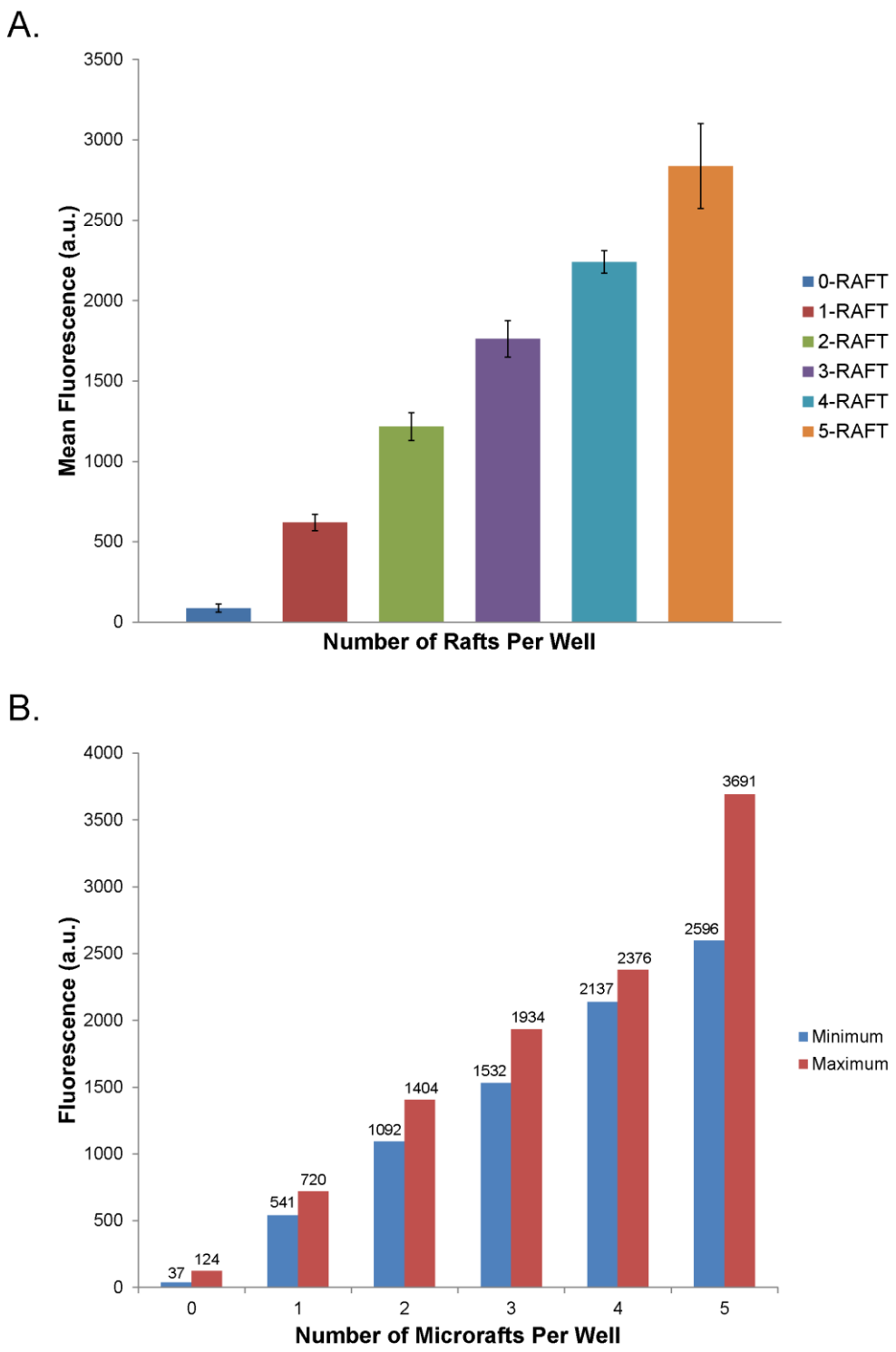

Figure 5.3. Fluorescence signals for rhodamine B infused microrafts. (A) Mean fluorescence values for different size groups of microrafts per well. (B) Minimum and maximum fluorescence values for different size groups of microrafts per well.

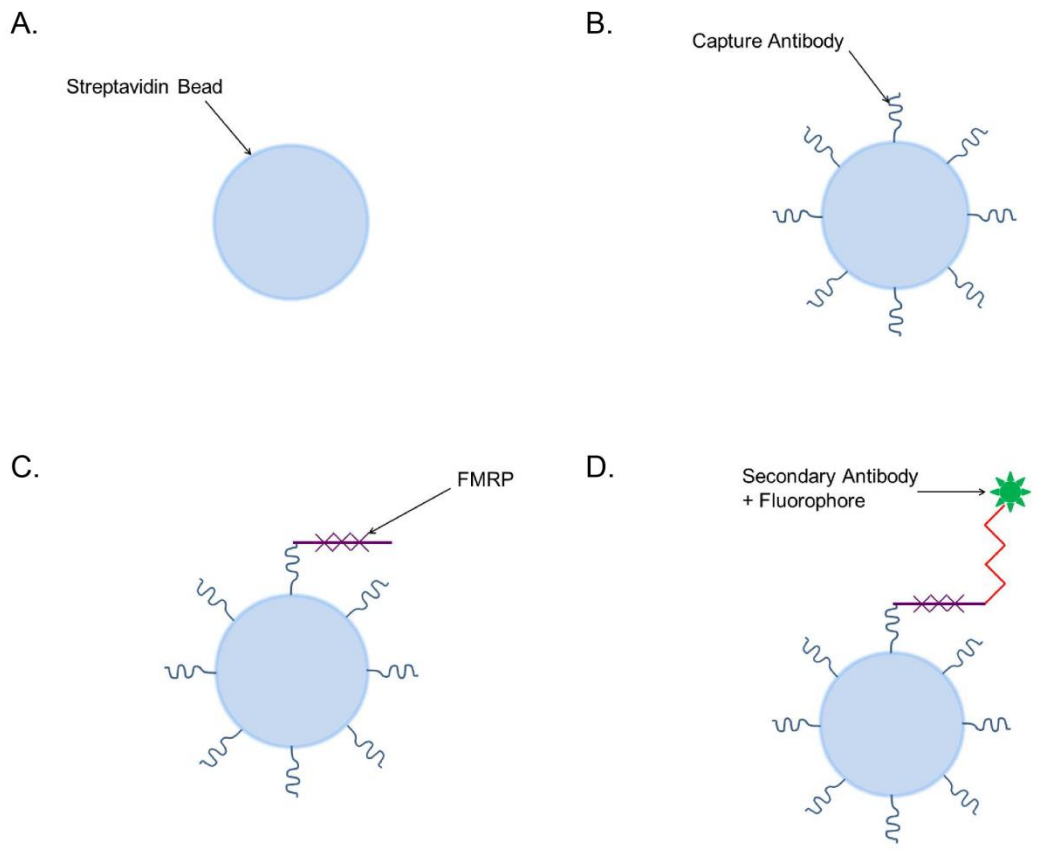

Figure 5.4. Bead based ELISA format (A) Streptavidin beads are centrifuged and washed. (B) Capture antibody is bound to streptavidin bead. (C) Cell lysate is incubated with bead-capture construct to bind FMRP. (D) Detection anti-FMRP and secondary conjugated antibodies are introduced in separate steps.

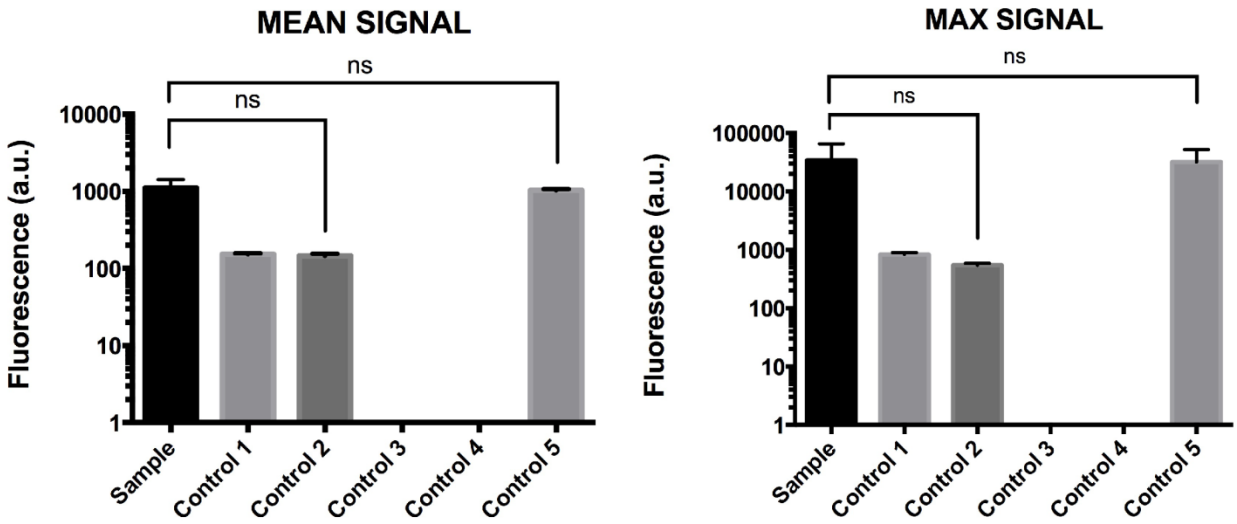

		Mean	Max
Sample	Beads+Cap+Lysate+Det+Sec	1,099	34,351
Control 1	Beads (no wash)	153	825
Control 2	Beads+Cap	145	547
Control 3	Det+Sec	0	0
Control 4	Lysate+Det+Sec	0	0
Control 5	Beads+Cap+Det+Sec	1,027	31,895

Figure 5.5. FMRP detection using flow cytometer and a bead-based ELISA..

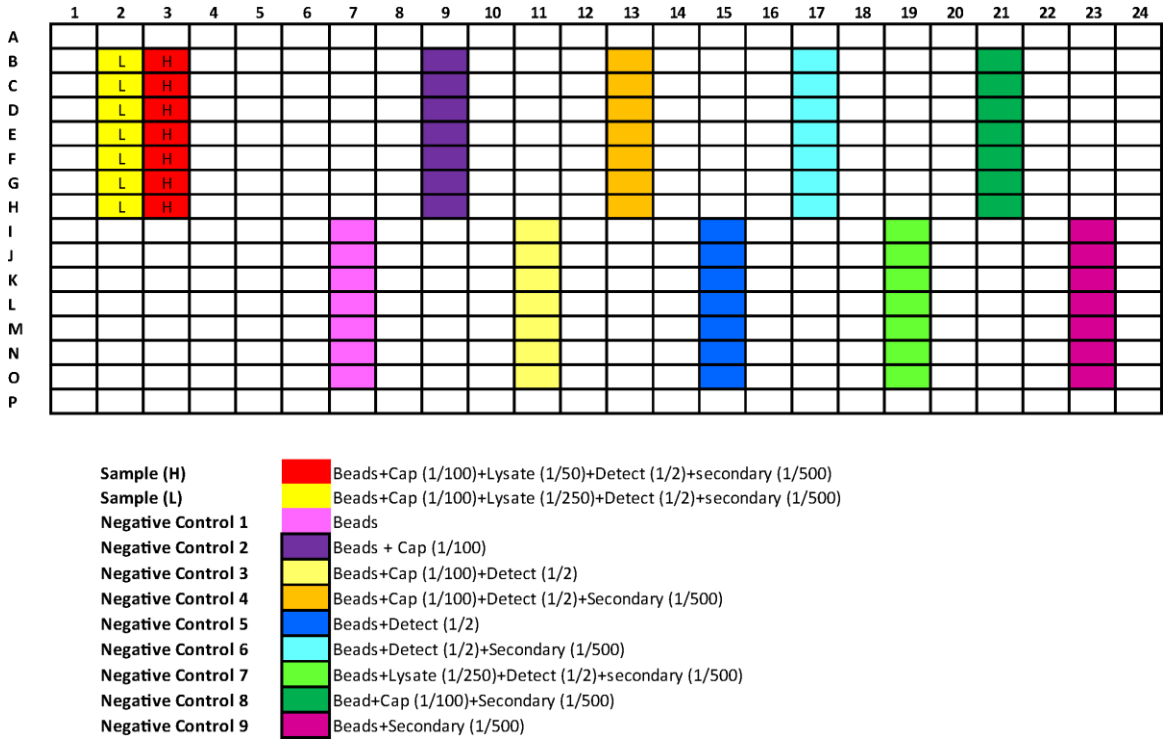

Figure 5.6. 384-well microplate experimental layout showing samples in red and yellow and controls in various colors.

A.

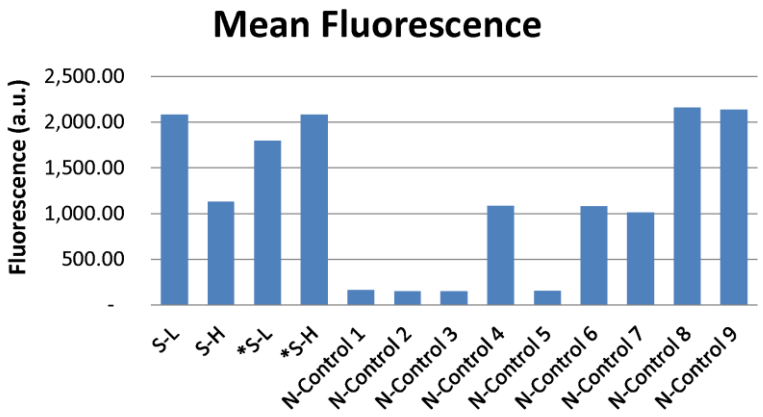

B.

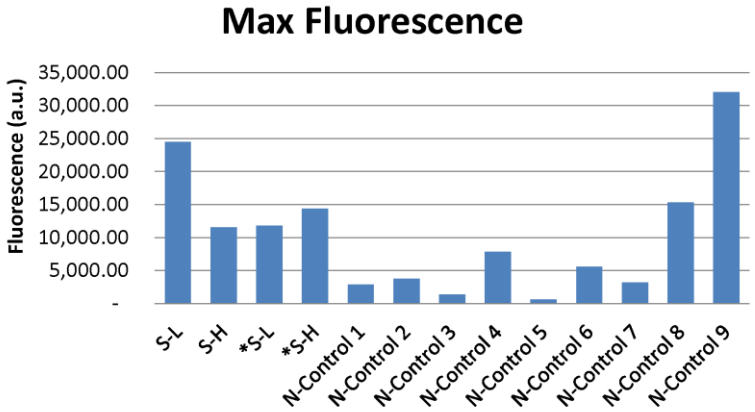

Figure 5.7. Flow cytometer fluorescence signals. (A) Mean fluorescence for high concentration and low concentration FMRP samples compared to controls. (B) Max fluorescence for high concentration and low concentration FMRP samples compared to controls.

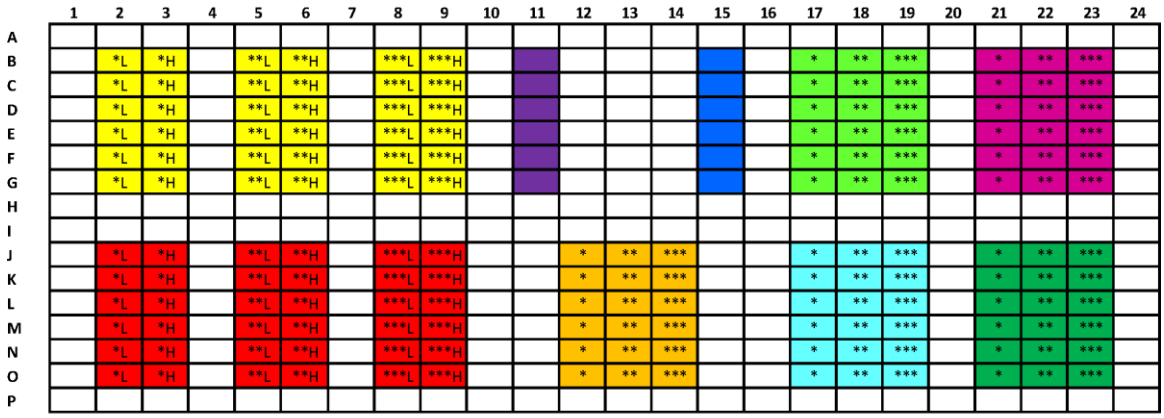

Sample 1	*L	Bead+Cap(1/100)+Lysate (1/250)+Detect(1/2)+Secondary (1/500)
Sample 2	*L	Bead+Cap(1/100)+Lysate (1/250)+Detect(1/20)+Secondary (1/500)
Sample 3	*H	Bead+Cap(1/100)+Lysate (1/50)+Detect(1/2)+Secondary (1/500)
Sample 4	*H	Bead+Cap(1/100)+Lysate (1/50)+Detect(1/20)+Secondary (1/500)
Sample 5	**L	Bead+Cap(1/100)+Lysate (1/250)+Detect(1/2)+Secondary (1/1000)
Sample 6	**L	Bead+Cap(1/100)+Lysate (1/250)+Detect(1/20)+Secondary (1/1000)
Sample 7	**H	Bead+Cap(1/100)+Lysate (1/50)+Detect(1/2)+Secondary (1/1000)
Sample 8	**H	Bead+Cap(1/100)+Lysate (1/50)+Detect(1/20)+Secondary (1/1000)
Sample 9	***L	Bead+Cap(1/100)+Lysate (1/250)+Detect(1/2)+Secondary (1/10,000)
Sample 10	***L	Bead+Cap(1/100)+Lysate (1/250)+Detect(1/20)+Secondary (1/10,000)
Sample 11	***H	Bead+Cap(1/100)+Lysate (1/50)+Detect(1/2)+Secondary (1/10,000)
Sample 12	***H	Bead+Cap(1/100)+Lysate (1/50)+Detect(1/20)+Secondary (1/10,000)
Negative Control 1		Beads+Cap (1/100)+Detect (1/2)
Negative Control 2	*	Beads+Cap (1/100)+Detect (1/2)+Secondary (1/500)
Negative Control 3	**	Beads+Cap (1/100)+Detect (1/2)+Secondary (1/1000)
Negative Control 4	***	Beads+Cap (1/100)+Detect (1/2)+Secondary (1/10,000)
Negative Control 5		Beads+Detect (1/2)
Negative Control 6	*	Beads+lysate+Detect (1/2)+secondary (1/500)
Negative Control 7	**	Beads+lysate+Detect (1/2)+secondary (1/1000)
Negative Control 8	***	Beads+lysate+Detect (1/2)+secondary (1/10,000)
Negative Control 9	*	Beads+Detect (1/2)+Secondary (1/500)
Negative Control 10	**	Beads+Detect (1/2)+Secondary (1/1000)
Negative Control 11	***	Beads+Detect (1/2)+Secondary (1/10,000)
Negative Control 12	*	Bead+Cap (1/100)+Secondary (1/500)
Negative Control 13	**	Bead+Cap (1/100)+Secondary (1/1000)
Negative Control 14	***	Bead+Cap (1/100)+Secondary (1/10000)
Negative Control 15	*	Beads+Secondary (1/500)
Negative Control 16	**	Beads+Secondary (1/1000)
Negative Control 17	***	Beads+Secondary (1/10,000)

Figure 5.8. 384-well microplate experimental layout showing samples in red and yellow and controls in various colors.

A.

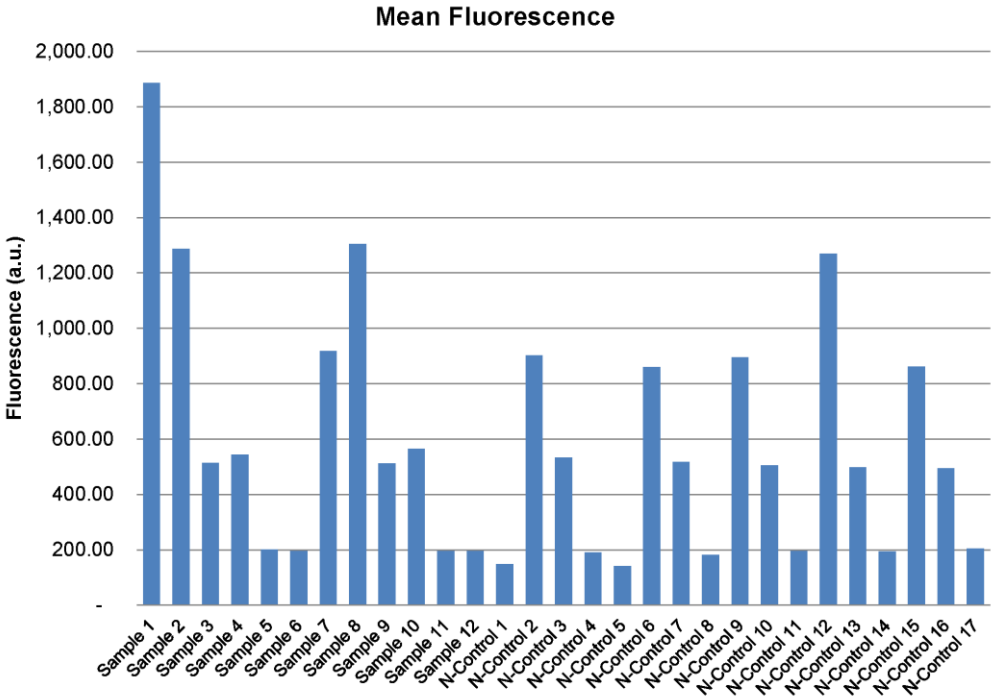

B.

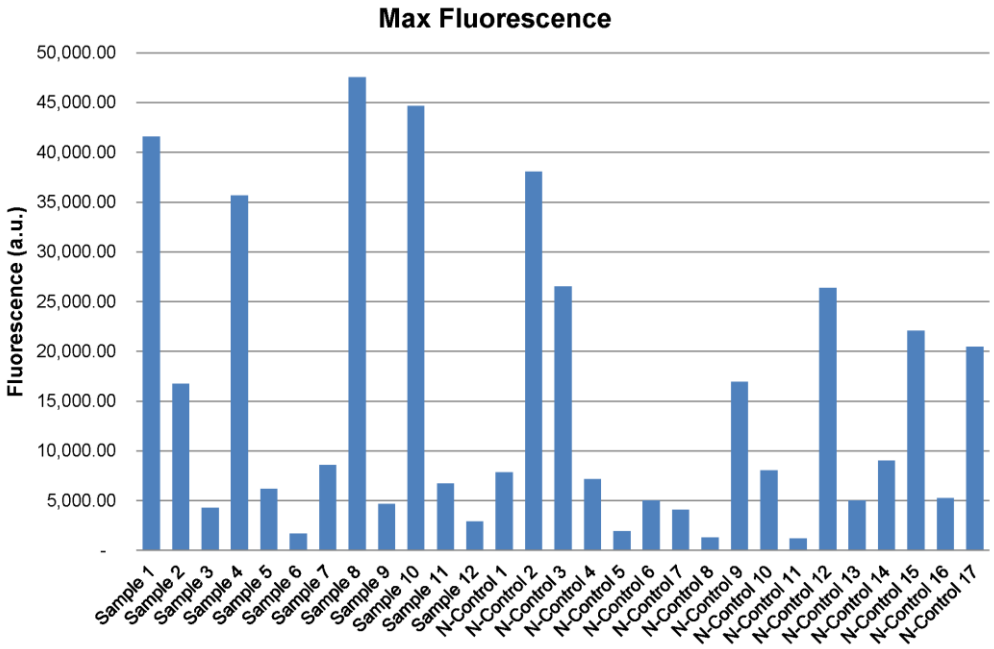

Figure 5.9. Flow cytometer fluorescence signals. (A) Mean fluorescence signal of samples and controls at various secondary antibody dilutions. (B) Max fluorescence signal of samples and controls at various secondary antibody dilutions. See Figure 5.8 for sample and control identifications.

A.

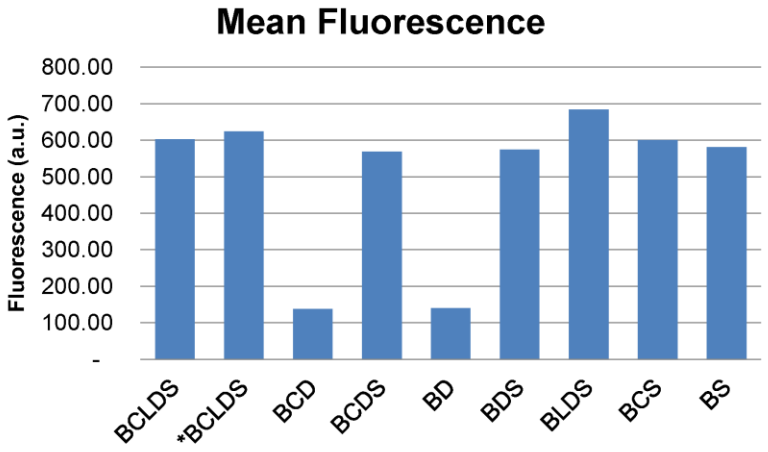

B.

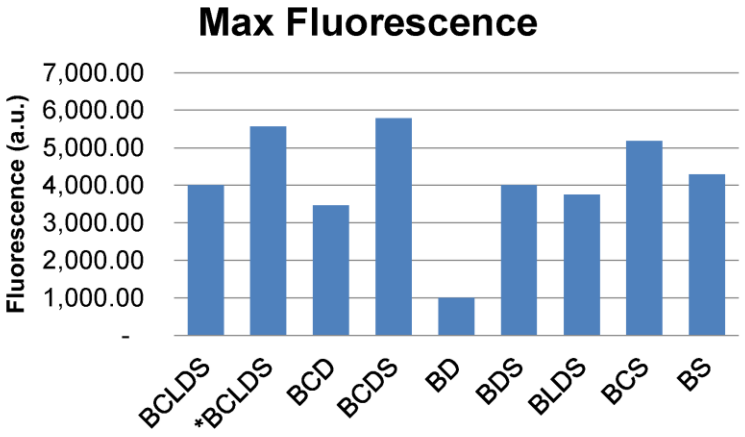

Figure 5.10. Flow cytometer fluorescence signals produced from the lysate of neurons grown on microrafts. (A) Mean fluorescence signal of samples and controls. (B) Max fluorescence signal of samples and controls. Letters represent component combinations. B = bead, C = capture antibody, L = lysate, D = detection antibody, S = secondary antibody, * indicates lysate from recombinant FMRP.

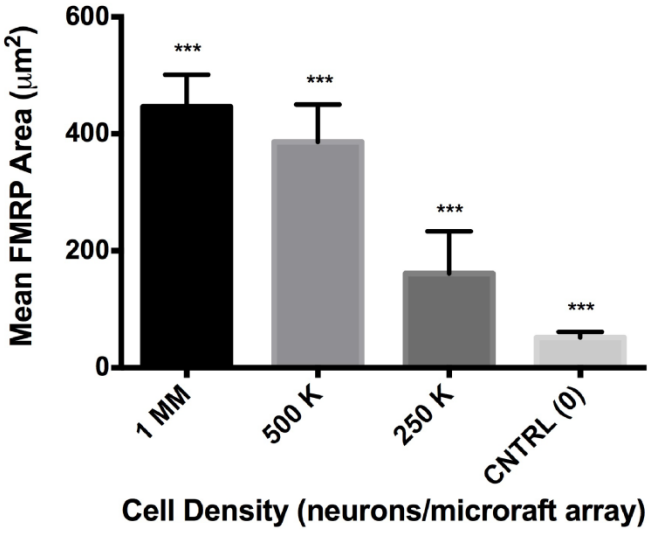

Figure 5.11. Immunofluorescence FMRP measurements versus cell density.

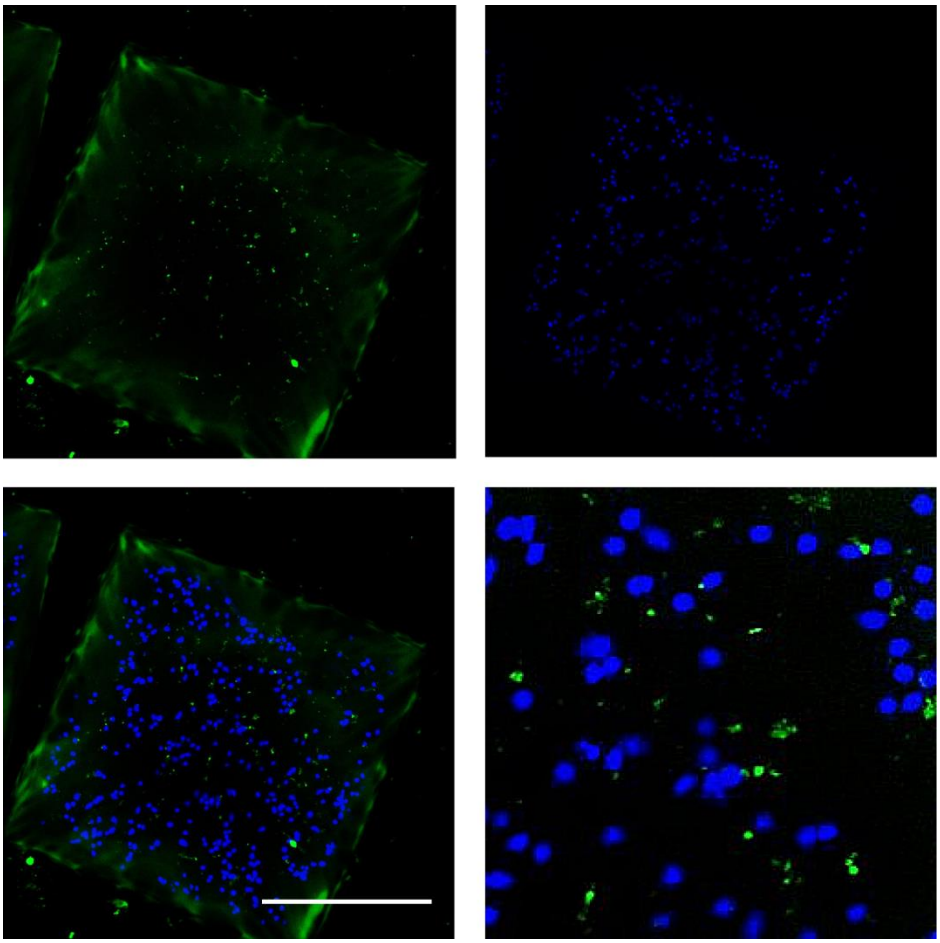

Figure 5.12. Representative 20X images of rate hippocampal neurons plated at 1MM cells/mL (A) FMRP specific marker. (B) DRAQ5 nuclear stain. (C) 2-channel composite image. (D) Magnified view of composite image. Scale bar = 250 µm.

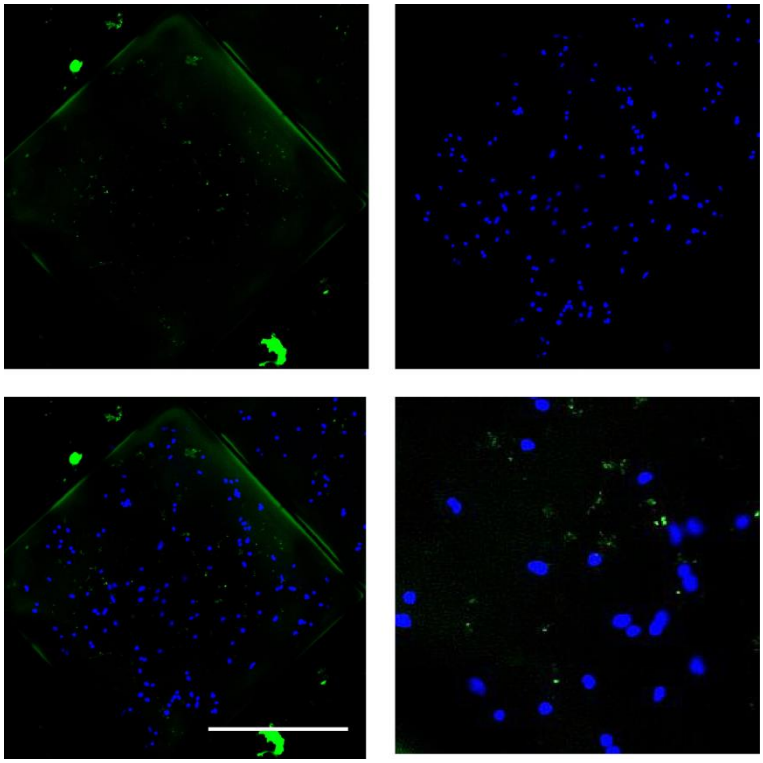

Figure 5.13. Representative 20X images of rate hippocampal neurons plated at 500K cells/mL (A) FMRP specific marker. (B) DRAQ5 nuclear stain. (C) 2-channel composite image. (D) Magnified view of composite image. Scale bar = 250 µm

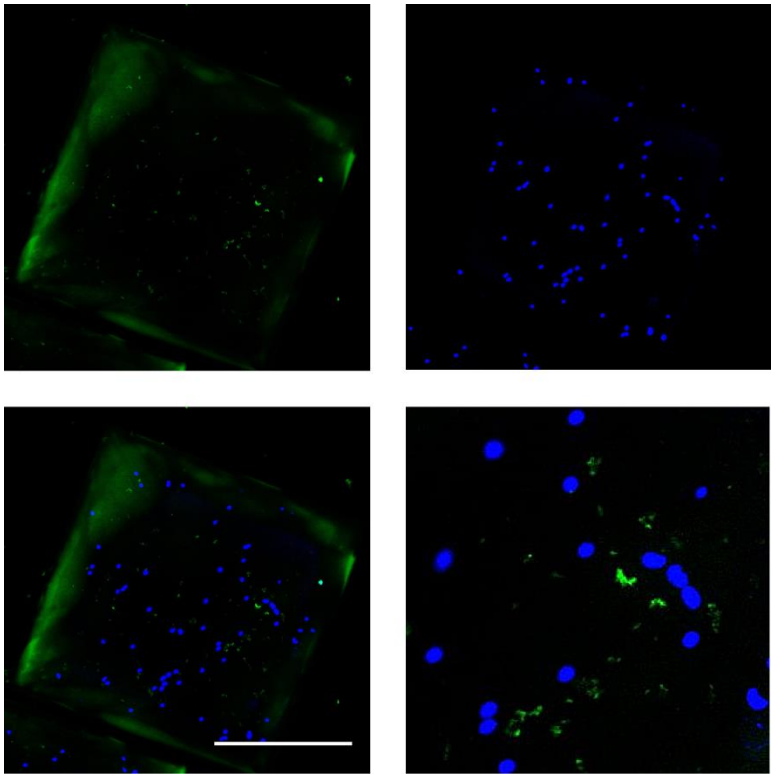

Figure 5.14. Representative 20X images of rate hippocampal neurons plated at 250K cells/mL (A) FMRP specific marker. (B) DRAQ5 nuclear stain. (C) 2-channel composite image. (D) Magnified view of composite image. Scale bar = 250 µm

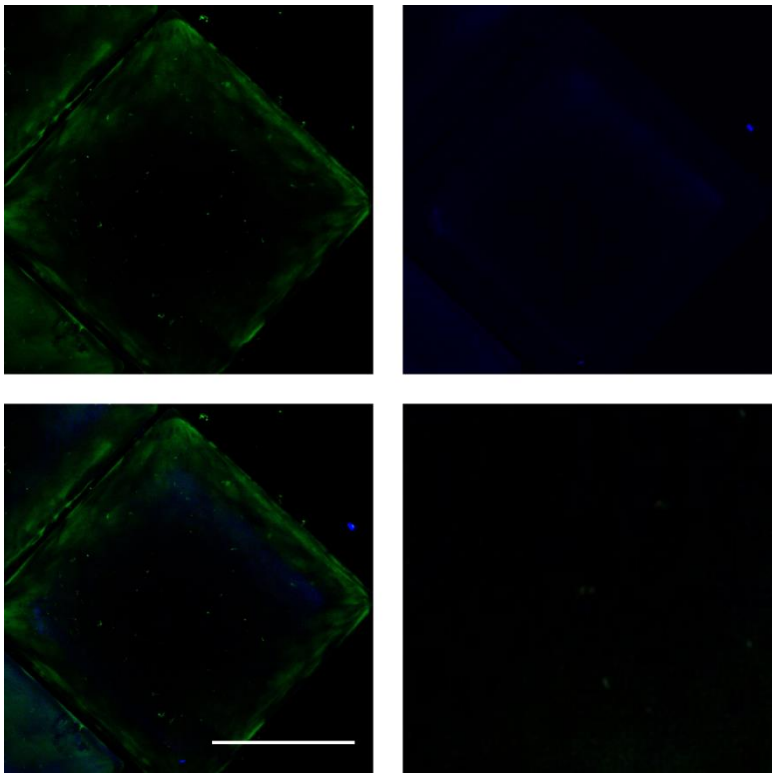

Figure 5.15. Representative 20X images of rate hippocampal neurons plated at 0K cells/mL (A) FMRP specific marker. (B) DRAQ5 nuclear stain. (C) 2-channel composite image. (D) Magnified view of composite image. Scale bar = 250 µm

5.6 BIBLIOGRAPHY

1. Iwahashi C, Tassone F, Hagerman RJ, Yasui D, Parrott G, Nguyen D, Mayeur G, Hagerman PJ. 2009. A quantitative elisa assay for the fragile x mental retardation 1 protein. Journal of Molecular Diagnostics. 11(4):281-289.

2. Schutzius G, Bleckmann D, Kapps-Fouthier S, di Giorgio F, Gerhartz B, Weiss A. 2013. A quantitative homogeneous assay for fragile x mental retardation 1 protein. Journal of Neurodevelopmental Disorders. 5.

3. Kumari D, Swaroop M, Southall N, Huang WW, Zheng W, Usdin K. 2015. High-throughput screening to identify compounds that increase fragile x mental retardation protein expression in neural stem cells differentiated from fragile x syndrome patient-derived induced pluripotent stem cells. Stem Cells Translational Medicine. 4(7):800-808.

4. Kaufmann M, Schuffenhauer A, Fruh I, Klein J, Thiemeyer A, Rigo P, Gomez-Mancilla B, Heidinger-Millot V, Bouwmeester T, Schopfer U et al. 2015. High-throughput screening using ipsc-derived neuronal progenitors to identify compounds counteracting epigenetic gene silencing in fragile x syndrome. Journal of Biomolecular Screening. 20(9):1101-1111.

5. Taylor AM, Wu J, Tai HC, Schuman EM. 2013. Axonal translation of beta-catenin regulates synaptic vesicle dynamics. J Neurosci. 33(13):5584-5589.

Chapter 6: Conclusions

This work set out to determine whether or not microraft arrays represent a viable tool for expanding cellular throughput in drug screening for neurological disorders. Previous work by Niedringhaus et al. using the microraft array for neuronal culturing and physiological measurement was very encouraging, but performed limited testing with traditional high-throughput screening tools such as high-density well plates and did not test the technology using a high-throughput formatted assay. For this research, the microraft array was used to culture human and rat neurons in 384-well high-density plates. New tools were created to transport, center, and secure the microrafts to facilitate screening, and scalable assays were devised in order to determine the feasibility of this technology in real screens for neurological disorders.

One of the biggest challenges in using the microrafts for cell-based screening is the manual handling of microrafts, as well as manually carrying out the processing steps of the described assays to extract useful data. An advantage of the microraft array in neurological screening is the possibility of using this technology without the need of expensive automated equipment. However, it was observed in this work that manual use of the microraft array for screening is difficult and impractical. Extracting the full potential of the microraft array requires seeding cells onto the device, releasing the individual microrafts, removing the microrafts and placing them one-by-one into individual wells of 384-well microtiter plates, supporting the

cellgrowth in a healthy manner, and then securing the microrafts with their attached neurons during assay processing steps such as washing, aspirating, and agitation etc. Such choreography proved to be very difficult under manual conditions. Neurons are arguably the most sensitive cell type in our body and disturbing them after plating and attachment can cause aggregation, detachment, or even cell death. Therefore, mass release of the microrafts by flexural deformation of their PDMS substructure can lead to these outcomes and individual release of each microrafts is more beneficial.

Additionally, transferring single rafts is also very difficult to perform with the naked eye and is quite time consuming. For these reasons, transferring microrafts individually with an automated approach is more beneficial. As a future strategy to enable high-throughput screening using microraft arrays, a system was conceived that would improve the release and transfer of microrafts for screening purposes (**see Appendix A.1-3**); the fabrication of this system was beyond the scope of this project. An automated system releasing and transferring the microrafts was developed by Attayek et al., however this system was designed specifically for 96-well plates and operates at about 30 seconds per well with a single magnetic wand and microneedle. The system sketched out in Appendix A would instead use 4x4 array of microneedles and miniaturized magnetic wands with a 4.5 mm spacing to match the well-to-well spacing of the 384-well plate. With this spacing, a customized microraft array (**Figure A.1 A**) would have to be produced such that the microrafts are released at the precise location of each magnetic wand tip. Compared to the original microraft array used throughout this work, this customized array would be

smaller containing about half the number of total microrafts, but each microraft would be slightly larger at 550 µm on each side. Using this customized system with the same 30 second cycle time of the previous 96-well automated system, a 384-well plate could be fully populated in approximately 12 minutes or less with 16 microraft transfers on each cycle.

Given the delicacy of neurons, assay procedures requiring washing and aspiration were very difficult to perform manually even with the security of the magnet array plate. These steps required very careful technique and vision so as to not disturb the cells. Such careful dexterity puts a lot of strain on the user, and thus fluid handling machines where fluid pressure and aspiration height can be specified are very much an advantage when using this technology. For future studies, the integration of automated fluid handling machines with the microraft arrays could improve assay performance and reliability.

Provided there is the ability to work with the microraft arrays in a highly controlled automated environment, there is much promise for their ability to help expand screening for neurological diseases using human or primary neurons. The future directions of this work include the design and implementation of a fully automated system that can successfully release and transfer single microrafts filling a 384-well plate in less than five minutes. Such a system (**Appendix A.1-3**) would have to be utilized in concert with a traditional fluid handling machine and stem cell facility such that the sterility chain would remain intact. Considering that assay development requires a very robust environment where many variables must be

tested in parallel and many plate layouts must be prepared, creating this automated system is critical in order to achieve desired results from appropriate sample sizes.

Once the release and transfer of the microrafts is fully automated for 384-well microtiter plates, the next major hurdle for the commercial adoption of the microrafts in neurological screens is demonstrating their use in a scalable high-throughput assay. In regards to this future assay development, a new more streamlined approach should be tested. The bead-based ELISA used in this work coupled with flow cytometry measurements was selected for its high sensitivity. However, this assay was very complicated to implement and requires extensive optimization and validation beyond the scope of this project. In an effort to avoid such complications and expedite the detection of FMRP in a high-throughput assay, a much more streamlined approach should be tested in the future.

In the previous study by Niedringhaus et al. the microrafts had been used to reproduce the results of an immunofluorescence screening assay originally used by Huang et al.[1] This assay was developed to screen compounds for potential treatment of Angelman syndrome and concluded with topotecan, a topoisomerase inhibitor as a possible therapy. In reproducing these results Niedringhaus et al. tested topotecan on embryonic neurons from a mouse model containing a Ube3a-YFP transgene within the normally silent paternal allele on the microrafts, resulting in increased YFP expression indicating that topotecan indeed activated the normally dormant paternal allele of Ube3a.[2] Although successfully reproducing the same results, this assay was based on high-content imaging which is typically not

considered “high-throughput” due to the extensive number of assay steps and the time required for image acquisition and analysis.

For testing the microraft arrays in a high-throughput scalable assay a good model to replicate would be that of Kumari et al. published in *Stem Cells Translational Medicine* in 2015.[3] In this study and assay was designed, optimized, and validated to measure increases in FMRP to identify potential drug candidates for treating fragile x syndrome. This assay utilized TR-FRET to detect the presence of FMRP in a 1536-well plate format. After first optimizing and validating the assay, a small screen was performed with the library of pharmacologically active compounds (LOPAC^{1280}) which contains 1280 compounds, and then with an FDA approved drug library containing ~4,000 compounds. As previously mentioned, none of these compounds produced FMRP at clinically relevant levels, however a proof of principle was established.

TR-FRET is an attractive assay type because of its simplicity. After seeding the cells and allowing them to attach and grow over night, compounds are introduced and incubated for 24 hours. Following the compound introduction, the cells were lysed with 4X lysis buffer at 4°C for 30 minutes. Then donor and acceptor antibodies were added and incubated simultaneously overnight at 4°C. The next day, the plate was read using an Envision Plate Reader (Perkin Elmer) with an excitation of 320 nm, a donor emission of 615 nm and an accepter emission of 665 nm. In theory, this same procedure could be performed on a plate containing microrafts and would have much less complexity compared to the bead based ELISA. This assay utilizes an anti-FMRP (clone 2D4)-K (Ab-7-K) donor antibody

with the Ab-K europium-cryptate donor fluorophore and anti-FMRP (D14F4)-d2 acceptor antibody with the Ab-d2 acceptor dye. Both of these antibodies are specific to the N-terminal of FMRP.

Using purified recombinant FMRP at various concentrations, the dynamic range was reported as linear between 4 - 270 fmol/µL which equals approximately 280 – 19,200 pg/µL. The incubation time for these antibodies, and the cell plating density were then optimized using FXS patient fibroblasts cultured in 384- and 1536-well plates. Once these results were acquired the assay was tested on iPSC-derived neural stem cells (NSCs) from FXS patients with the full mutation as well as healthy controls. The NSCs and their controls were plated at densities of 625, 1250, 2500, and 5000 cells per well in 1536-well solid bottom white plates and their FMRP levels were measured. FMRP levels were reported as the ratio of the sample fluorescence signal to the control fluorescence signal. Unfortunately the exact values of these measurements were not reported but judging by the graph published, it seems the following values represent an approximation of the raw data:

Cell Density (cells/well)	**FMRP Level (A.U.)**
625	38
1,250	25
2,500	20
5,000	10

After plotting these results (**Figure 6.1**), interestingly, it appears that the FMRP levels decrease in a logarithmic pattern as the cell density increases. However, compared to background levels this indicates that for small cell

populations the gap between the signal and background diminishes. With this assumption, fitting a logarithmic trend line results in a $R^2 = 0.974$. Using the equation of this line to estimate the FMRP levels for the average amount of cells on the microrafts (300-500 cells) results in a range of 46 – 39.5 which would still be less than half the signal produced from the healthy control which is represented by a value of 100.

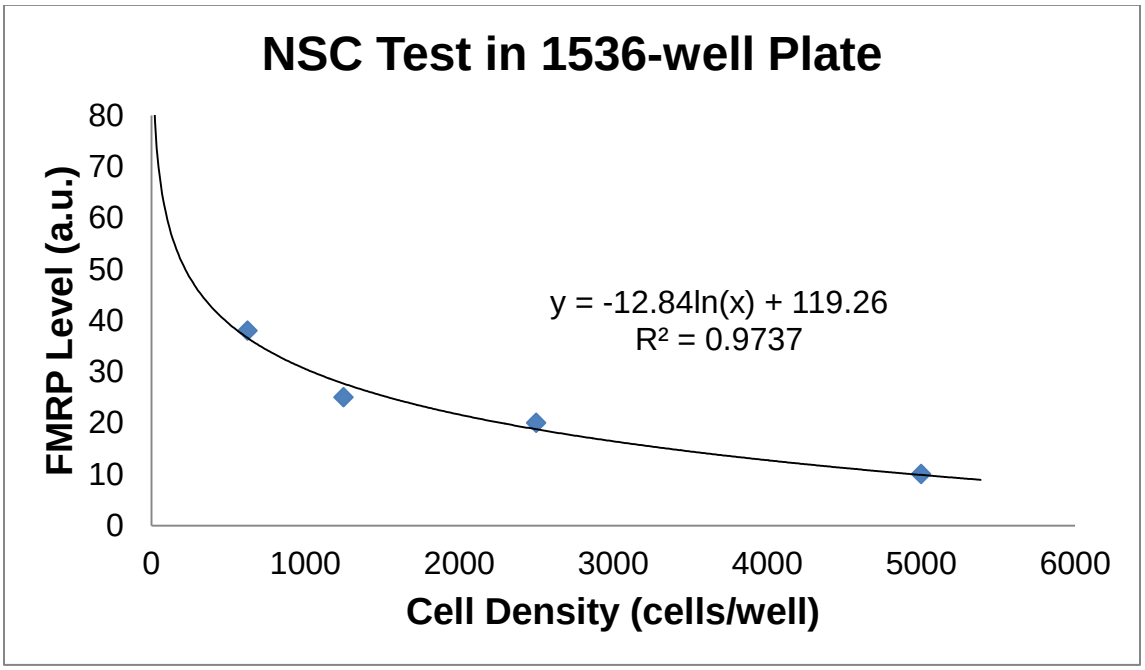

Figure 6.1. FMRP measurements in NSCs using TR-FRET assay by Kumari et al.

After testing the assay on NSCs, Kumari et al. also performed tests on iPSC-derived neurons plated in 1,536-well plates at a density of 2,500 cells/well. This experiment resulted in an FMRP level of 40, which was double the value of the NSC experiments at the same cell density. Therefore, assuming a similar logarithmic trend, the microraft might produce values of approximately 92 – 80 which is nearly indistinguishable from the control.

Finally, to validate the assay for HTS, signal to background (S/B) ratios were calculated along with the coefficient of variation (CV) and Z' scores. These metrics were calculated for FXS iPSC-derived NSCs and FXS iPSC-derived neurons each plated in 1536-well plates at a density of 2,500 cells/well along with controls from healthy donors. For the NSCs the S/B, Z', and CV were 5.2, 0.4, and 9.5% respectively. Assuming the same logarithmic relationship, for microrafts containing 300 - 500 neurons the S/B would be approximately 2.5 - 2.2. Since the distance between the signal and background is much narrower for 500 neurons, the Z'-factor will be reduced by the same proportions. Thus for 300 – 500 cells on the microrafts would produce Z'-factors approximately equal to 0.19 – 0.17. Although these numbers represent a very small separation band, performing a screen with the microrafts using this assay would still be possible. It's also possible that the CV values would remain the same.

In a study published prior to the Kumari paper, Schutzius et al. used a TR-FRET assay in a similar fashion to detect FMRP; however, this study only focused on assay development and did not perform any compound screening.[4] This study used an anti-FMRP 1C3 (Mab2160) donor antibody and an anti-FMRP (M03-d2) acceptor antibody – both specific to the N-terminal of FMRP like those used by Kumari et al. Due to the tendency of purified recombinant FMRP to aggregate, recombinant FMRP was fused with maltose binding protein (MBP-FMRP) for use in optimizing the assay. Using this MBP-FMRP, the antibody combination, and an Envision plate reader, a linear dynamic range was reported between 10 – 2000 pg/µL.

After optimization, to investigate if the assay was capable of quantifying endogenous human FMRP, batch lysates from FXS patient-derived fibroblasts and a healthy human control were tested. These cells were plated at various cell densities ranging from 500 – 8,000 cells/well in 384-well plates, and the Z'-factors were reported. At 8,000 cells per well Z' = 0.85 whereas for 500 cells per well Z' = 0.03. Since these tests were performed on fibroblasts, it's difficult to interpolate them to neurons, but based on these results and the estimates from the findings of Kumari et al., it's reasonable to assume that a screen performed with 500 neurons on microrafts would result in a Z'-factor less than 0.5 which is the standard benchmark above which an assay is considered excellent and simply "screenable" when this value falls between 0 and 0.5. Moreover, at the wells plated with 500 fibroblasts produced a change in fluorescence equal to

Finally, in order to test the feasibility of using microraft arrays with hiPSC-derived neurons, future experiments growing these cells on the microraft arrays should be conducted. These experiments should test neuron viability over time, neurite outgrowth, as well as electrophysiological cues and synaptic function compared to the same cells grown directly in 384-well plates. Moreover, various protocols should be tested in parallel to determine the various kinds of neurons that can be differentiate on the microrafts working with 384-well plates. Knowing the types of neurons which can be produced on the microrafts is important in further demonstrating their utility as a tool for neurological drug screening.

At present, the microraft array is very challenging to use. However, the benefits it promises, namely a >20 fold increase in throughput with 384-well plate

compatibility, suggest that implementing the above changes beyond the current scope of work will help unlock its true potential as a screening tool. Moreover, based on previous work there is evidence that this technology could be used with a TR-FRET based high-throughput screening assay further validating its potential.

6.1 BIBLIOGRAPHY

1. Huang HS, Allen JA, Mabb AM, King IF, Miriyala J, Taylor-Blake B, Sciaky N, Dutton JW, Lee HM, Chen X et al. 2012. Topoisomerase inhibitors unsilence the dormant allele of ube3a in neurons. Nature. 481(7380):185-+.

2. Niedringhaus M, Dumitru R, Mabb AM, Wang Y, Philpot BD, Allbritton NL, Taylor AM. 2015. Transferable neuronal mini-cultures to accelerate screening in primary and induced pluripotent stem cell-derived neurons. Sci rep. England. p. 8353.

3. Kumari D, Swaroop M, Southall N, Huang WW, Zheng W, Usdin K. 2015. High-throughput screening to identify compounds that increase fragile x mental retardation protein expression in neural stem cells differentiated from fragile x syndrome patient-derived induced pluripotent stem cells. Stem Cells Translational Medicine. 4(7):800-808.

4. Schutzius G, Bleckmann D, Kapps-Fouthier S, di Giorgio F, Gerhartz B, Weiss A. 2013. A quantitative homogeneous assay for fragile x mental retardation 1 protein. Journal of Neurodevelopmental Disorders. 5.

APPENDIX

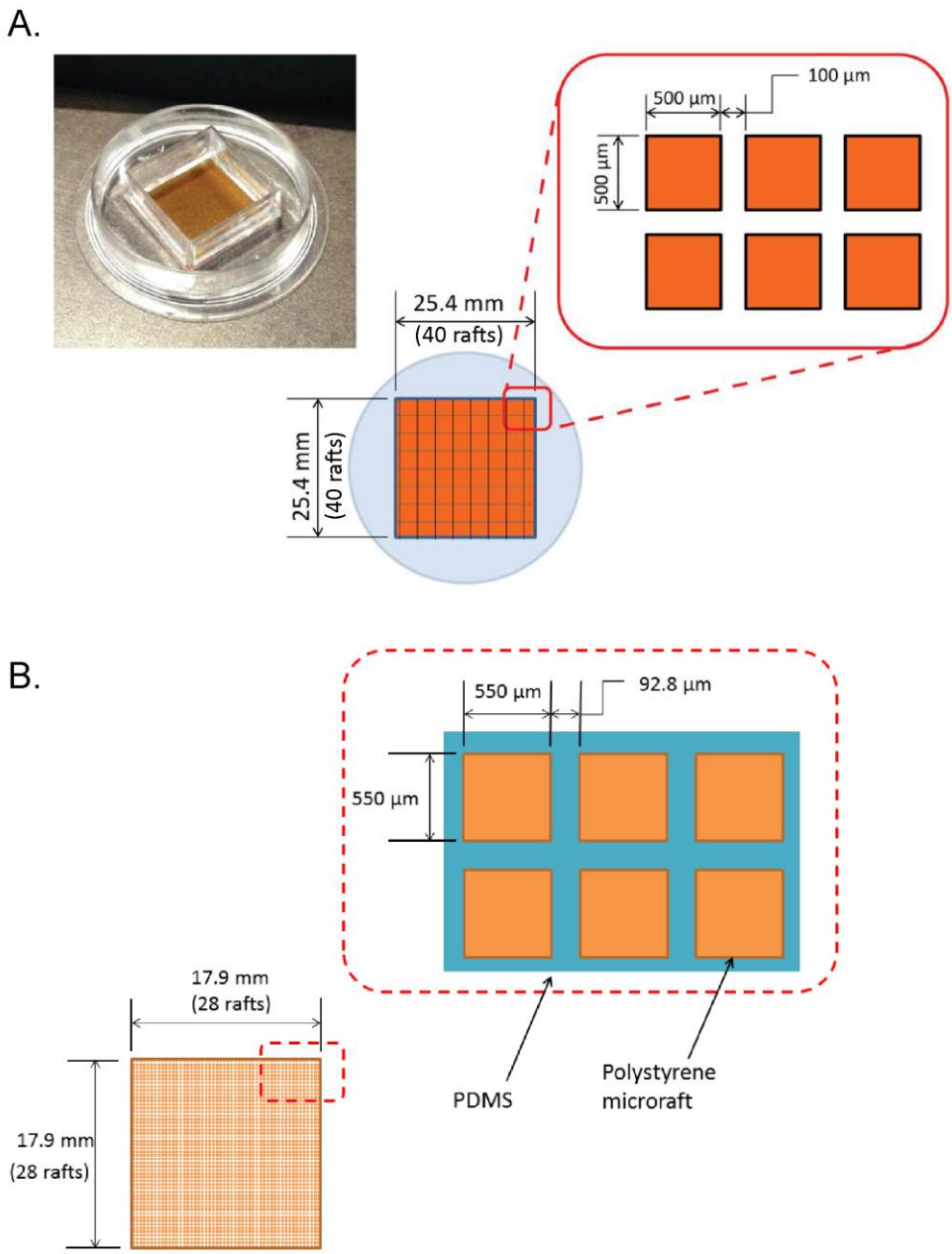

Figure A.1. Modified microraft array design for 384-well automation. (A) Original microraft design used in all experiments. (B) Redesigned microraft array for automated release and transfer to 384-well plates

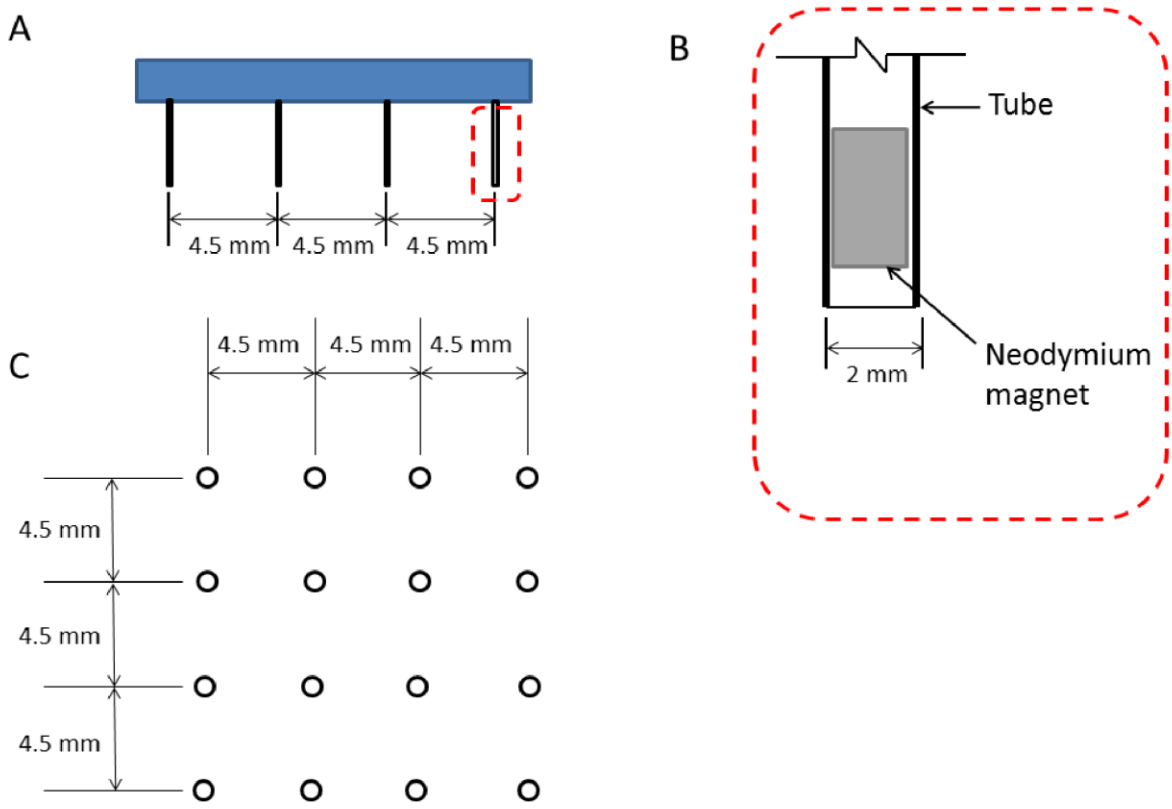

Figure A.2. Custom magnetic wand array design for 384-well automation. (A) Profile view showing magnetic wands attached to a single substrate. (B) Detailed view of individual magnetic wand design featuring a free moving magnet within a sealed tube for capture and release of microrafts. (C) Plan view of 4x4 magnet wand array with 4.5 mm spacing to match spacing of 384-well plate.

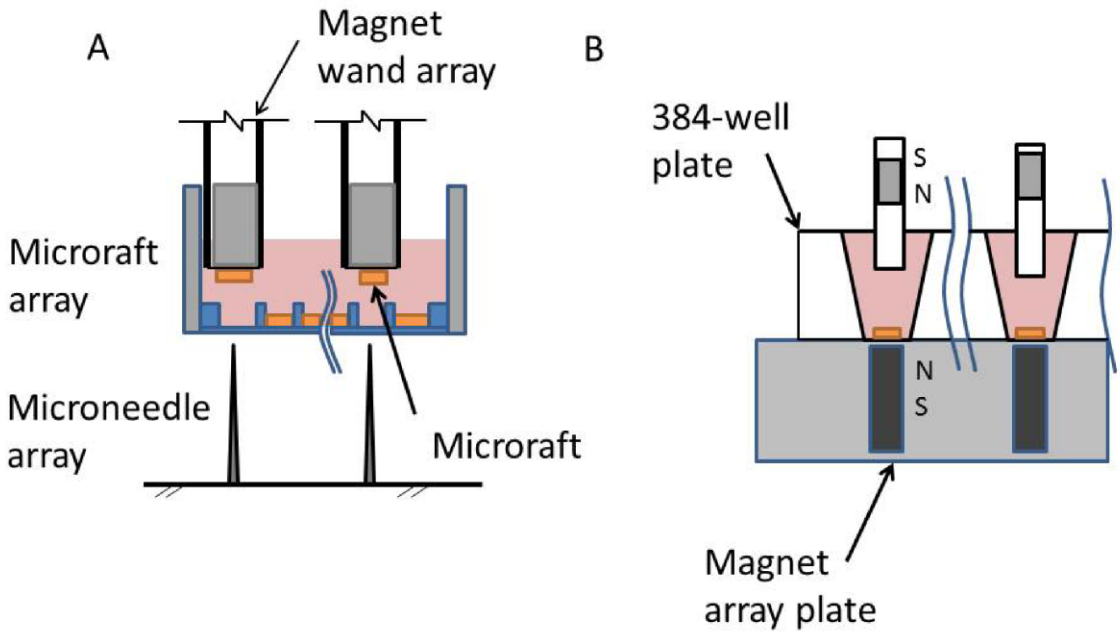

Figure A.3. Schematic of 384-well Cellraft release and transfer process. (A) Release of individual microrafts with a 4x4 microneedle array with simultaneous capture via magnet wand array. (B) Release of microrafts from magnet wand array via magnetic repulsion using the magnet array plate.